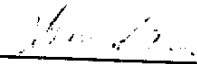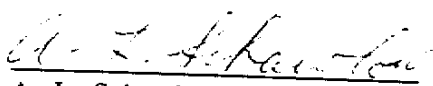ATOM INTERFEROMETRY IN AN ATOMIC FOUNTAIN

A DISSERTATION

SUBMITTED TO THE DEPARTMENT OF APPLIED PHYSICS

AND THE COMMITTEE ON GRADUATE STUDIES

OF STANFORD UNIVERSITY

IN PARTIAL FULFILLMENT OF THE REQUIREMENTS

FOR THE DEGREE OF

DOCTOR OF PHILOSOPHY

by

Mark A. Kasevich

June 1992

I certify that I have read this dissertation and that in my opinion it is fully adequate, in scope and quality, as a dissertation for the degree of Doctor of Philosophy.

_____
S. Chu   (Principal Advisor)

I certify that I have read this dissertation and that in my opinion it is fully adequate, in scope and quality, as a dissertation for the degree of Doctor of Philosophy.

_____
A. L. Schawlow   (Physics)

I certify that I have read this dissertation and that in my opinion it is fully adequate, in scope and quality, as a dissertation for the degree of Doctor of Philosophy.

_____
B. Cabrera   (Physics)

Approved for the University Committee
on Graduate Studies:

_____

ii

For my wife,

Mary

and my parents,

Ray and Elizabeth

ABSTRACT

An interferometer for atoms has been demonstrated using laser cooled sodium atoms and the mechanical effects of velocity sensitive stimulated Raman transitions. The interferometer has been used to measure the acceleration due to gravity, g, of an atom with a resolution of 3 parts in 10^8, and interference has been observed for atomic wavepackets separated by as much as 6 mm.

Momentum recoil associated with velocity sensitive stimulated Raman transitions was used to coherently divide, redirect and recombine the atomic wavepacket. These transitions have also been used to prepare ensembles of atoms with one-dimensional velocity spreads as narrow as 300 μm/sec, and to measure the temperature of polarization gradient cooled atoms.

Laser cooling and trapping techniques have been used to develop an "atomic fountain" source for the interferometer experiment: cold atoms were launched on vertical ballistic trajectories which turned due to gravity within the confines of the apparatus. This source has also been used in rf spectroscopy of the sodium groundstate hyperfine interval and for observation of the Casimir/van der Waals force between sodium atoms and a dielectric surface.

ACKNOWLEDGEMENTS

TABLE OF CONTENTS

LIST OF TABLES

LIST OF FIGURES

SECTION 1

INTRODUCTION

In 1975 Schawlow and Hänsch introduced the idea that light could be used to cool atoms.[1] A decade later, Chu and coworkers used light to cool a dilute vapor of sodium atoms to a temperature of $\sim 240~\mu$K.[2] Dubbed "optical molasses," this dilute, ultra-cold vapor had a density of $\sim 10^6$ atoms/cm^3 and atoms within the vapor an rms velocity of ~ 1 m/sec. Two years later, Dalibard suggested that atoms could be localized (trapped) as well as cooled by light by combining light forces with magnetic field gradients.[3] Subsequently, Chu, Pritchard, and collaborators demonstrated magneto-optic trapping of atoms.[4] The addition of forces which spatially localized the atoms increased the density to $\sim 10^{11}$ atom/cm^3, but kept the temperature of the vapor well below a mK.

Further experimental and theoretical investigations have refined/defined the mechanisms at work in optical molasses and magneto-optic traps. Both systems have proven to be richly complex. They are interesting objects of study in their own right and have led to important progress in understanding the interaction of light with atoms.

From a more pragmatic perspective, these advances have provided researchers, for the first time, with dense sources of cold atomic vapors. The work described in this thesis relates to a series of experiments which owe their existence to laser cooled and trapped sources. These experiments provide us with new methods in the fields of precision spectroscopy and cold atom-surface collisions. In addition, they have played a role in the burgeoning field of atom optics.

Most of the experiments in this thesis have required the development of new atom manipulation techniques, all centered on the idea of controlling the velocity of an ensemble of atoms with light. Developments include velocity control with "moving molasses,"[5] Doppler sensitive stimulated Raman transitions,[6] and recent demonstration of a scheme to cool atoms below the so-called photon recoil limit.[7]

The following paragraphs outline broad classes of experiments which have

benefitted from the use of cold atom sources. The scope is not exhaustive, but is significantly broader than that of the work presented in subsequent chapters. The intent is to view the atom manipulation techniques used in the central experiment of this thesis, demonstration of an interferometer for atoms, in the context of related experiments performed during the course of this research.

1.1 PRECISION SPECTROSCOPY

1.1.1 *Clocks*

For experiments where the energy-time uncertainty principle $\Delta\omega\Delta t \sim 1$ limits the linewidth of a resonance, increasing the measurement time Δt often enhances accuracy by narrowing the resonance linewidth $\Delta\omega$. Rf hyperfine clock (ie. the Cs $4S_{1/2}$, F=3 to $4S_{1/2}$, F=4) transitions are natural examples of this type of resonance. In an effort to maximize measurement time, Zacharias, in the early 50's, attempted to use gravity to confine atoms by launching them on vertical ballistic trajectories.[8] His scheme relied upon the Boltzman tail of a thermal atomic beam as a source of atoms slow enough to turn around in his apparatus. The experiment failed because fast atoms knocked slow atoms out of the interaction region. Despite the failure, the idea survived, with numerous researchers proposing the fountain geometry for precision measurements.[9,10] Zacharias' idea was good, it simply needed a better atomic source.

Using laser cooling and trapping techniques, it became feasible to construct a suitable source. Our novel idea was to first trap, then cool, and finally launch atoms on ballistic trajectories at speeds slow enough so that the majority of atoms turned due to gravity within the confines of our modest sized apparatus. Atoms were launched by resonant radiation pressure (first observed by Frisch over 50 years ago!): a short resonant pulse of light lofted atoms vertically. This "atomic fountain" geometry confined atoms in an intrinsically perturbation free environment for measurement times $\Delta t \sim 1$ sec for an apparatus ~ 1 m tall.[11] The subsequently improved version of this fountain, which uses a "moving molasses" to launch the atoms, is described in section 3.

We used the fountain to measure the sodium 1.7 GHz groundstate hyperfine resonance frequency. After trapping, cooling, launching and finally optically pumping
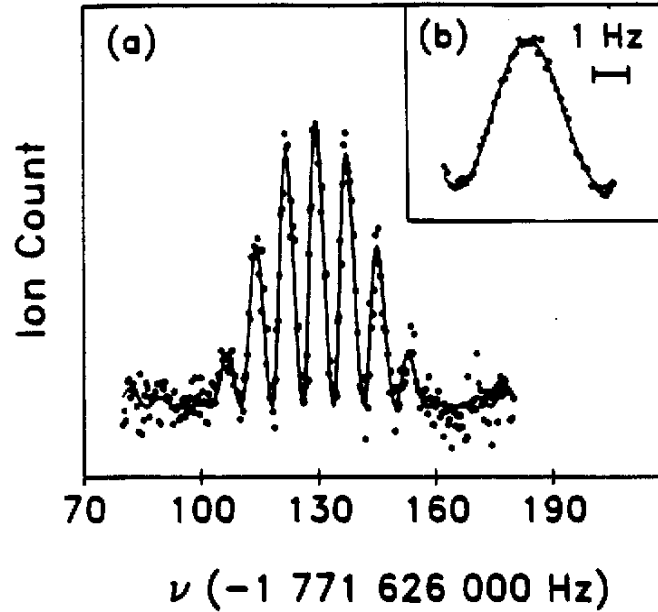
Figure 1.1: Rf spectroscopy in an atomic fountain — the sodium hyperfine interval. (a) The observed lineshape for two 32-msec $\pi/2$ pulses separated by 125 msec. (b) The center fringe for two 3.2 msec $\pi/2$ pulses separated by 255 msec. Pulses were applied near the top of the atom's ballistic trajectory to drive the sodium $3S_{1/2}$, $F=1 \rightarrow 3S_{1/2}$, $F=2$ "clock" transition.

atoms into one of the hyperfine levels, we probed the resonance with Ramsey's method of separated oscillatory fields:[12] near the apex of their ballistic trajectories, atoms were irradiated with two short radio-frequency pulses separated in time by 255 msec. The resulting resonance fringe width, measured by detecting the number of atoms in the other hyperfine state, was ~2 Hz, as shown in Fig. 1.1. After 1000 sec worth of data integration time, our counting statistics enabled us to determine the center of the fringe to ± 10 mHz.

This experiment demonstrated the feasibility of a fountain-based atomic clock. Several groups are actively pursuing this technology as a next generation time standard.[13] The atom of choice for these clocks is Cs, not Na. The large mass of cesium allows for laser cooled ensembles with velocity spreads substantially narrower than those of sodium. This, in turn, produces better counting statistics by allowing more

3

atoms to contribute to the resonance signal. Furthermore, the Cs hyperfine interval currently defines the second, and the Cs ground state resonance frequency of ~ 9.2 GHz is a factor of 5 greater than the Na interval of 1.7 GHz.

The ultimate clock may be a fountain-based standard using an metastable optical resonance.[14] With a Q of 10^{15} and count rates of 10^6/sec, short term stabilities of $10^{-18}/\tau^{1/2}$ (where τ is the measurement time in seconds) might be realized. Unfortunately, this lies in the future: there is no realistic candidate atom which can both be laser cooled with present laser technology and which possesses a long lived resonance suitable for clock work.[15]

1.1.2 Doppler Spectroscopy

The marriage of narrow atomic fountain linewidths and highly Doppler sensitive transitions has lead to a new class of precision experiments: those where the Doppler shift itself becomes the object of study. A precise measurement of a Doppler shift, which can be in principle limited by the transit-time through an atomic fountain, can yield detailed knowledge of the velocity of an atom through the usual Doppler relation $\delta\omega_{Dopp} \sim \mathbf{k} \cdot \mathbf{v}$, where $\mathbf{k}$ is the propagation vector for the light and $\mathbf{v}$ is the velocity of the atom. For example, by precisely measuring the rate of change of the Doppler shift of an atom accelerating due to gravity we have been able to make a precision measurement of g, the acceleration due to gravity, for atoms.[16,17] This experiment is described in detail in section 5. Other measurements of this type include measurement of the Doppler shift acquired as a result of scattering a photon,[18,19] which in turn allows for precise determination of the quantity $m/\hbar = k/v$ (m the atomic mass), and precise measurements of Doppler shifts induced by rotations.[20] As an example of possible level of sensitivity which can be achieved, consider a one-photon transition to a metastable optical level of frequency $\sim 10^{15}$ Hz. With a resonance linewidth of 1 Hz, a velocity resolution of $\Delta v = c(1 \text{ Hz}/10^{15} \text{ Hz}) \sim 0.3$ μm/sec is attainable!

There are a number of difficulties in achieving this level of sensitivity. First, the laser source used to drive the one-photon transition must be phase stable over the measurement time, ie. it must have an absolute frequency linewidth of < 1 Hz. To

date, ultra-stable lasers have absolute linewidths of ~ 80 Hz.[21] Second, vibration of mirrors/optical components which steer the light into the interaction region may Doppler shift the frequency of the light used to probe the atoms by much more than 1 Hz. Finally, the number of atoms which can contribute to a resonance seems exceedingly small. For example, an ensemble of laser cooled sodium atoms typically has an rms velocity width of ~ 30 cm/sec, so the fraction of atoms in a one dimensional velocity slice 0.3 μm/sec wide is 10^{-6}.

The first problem is solved by the use of two-photon velocity sensitive stimulated Raman transitions.[6] Consider a three-level atom consisting of two hyperfine groundstate levels $|1\rangle$ and $|2\rangle$ and an intermediate optical level $|i\rangle$. An atom with population in level $|1\rangle$ can be driven to level $|2\rangle$ when illuminated by two optical beams of frequencies ν_1 and ν_2 nearly resonant with the intermediate level $|i\rangle$ and with frequency difference ν_1-ν_2 of approximately the hyperfine interval. If the two beams are counter-propagating, the sensitivity to Doppler shifts is $\Delta\nu = (\Delta v/c)(\nu_1+\nu_2)$ or nearly twice that of a single optical photon. When the two frequencies used to drive the transition are derived from the same laser source (with the second frequency, for example, being generated by modulation of the first with a non-linear optical element), fluctuations in the absolute laser frequency are present in each beam, and since the atom responds to the difference frequency of the two beams, these fluctuations cancel.[22] Thus, two-photon Raman transitions provide a scheme where highly Doppler sensitive transitions are driven between internal levels stable against spontaneous decay, without ultra-stable lasers. In our 1991 experiment, we demonstrated for the first time the feasibility and Doppler sensitivity of Doppler sensitive stimulated Raman transitions in sodium. In this experiment, we prepared and observed samples of atoms with velocity spreads ~ 300 μm/sec (corresponding the effective 1-D temperatures of 2.4×10^{-11} K). This work is described in section 4.

The second problem, vibrations, is solved by referencing the phase of the light field to a platform known to be inertially stable. We used two approaches during the course of this research. In the first approach, we phase-locked the heterodyne beatnote between the two Raman beams to a stable rf-source. If the beatnote is measured directly outside the interaction region, only the optical elements used to overlap the laser beams

need be inertially stable.[6,16] Alternatively, if the counter-propagating beam is derived by retro-reflecting a beam containing both Raman frequency components, then only the retro-reflecting mirror must be stable.[17]

The third issue, that of count rates, can be circumvented for certain classes of interactions by techniques first introduced by Bordé[23] and Chebotayev[24] in what is broadly labelled optical Ramsey spectroscopy. In the specific case of measuring the acceleration of an atom due to gravity, we are not interested in the initial velocity of the atom, only the change in the velocity of the atom after a known time. The resonance condition for a $\pi/2$-τ-$\pi/2$ light-pulse sequence, analogous to an NMR spin-echo sequence, is well suited to this measurement: it is not sensitive to the initial velocity of the atom, but is sensitive to changes in velocity.[5] Because gravity changes the velocity of all atoms in the same way, in principle an entire ensemble of atoms can contribute to the signal. Clearly this technique applies to any experiment designed to measure a force which effects all atoms in the ensemble in the same manner. In our June 1991 experiment,[16] we were able to use this technique to measure the acceleration of an atom due to gravity to a relative precision of 3 parts in 10^6. With straightforward improvements we were subsequently able to demonstrate a sensitivity of 3 parts in 10^8.[17]

Our experimental resolution was limited by vibration of our inertial reference. However, we anticipate that by using state-of-the-art active vibration isolation systems,[25,26] we ought to be able to achieve short term accuracies of 10^{-9} $g/\tau^{1/2}$, where τ is the signal integration time in seconds, again limited by the performance of the vibration isolation. As in the clock experiment described above, use of laser cooled cesium atoms, rather than sodium, significantly enhances count rates: if vibration isolation were not a factor, short term stabilities could approach 10^{-10} $g/\tau^{1/2}$ in a cesium fountain.

1.2 ATOM OPTICS

When considering the atom as a quantum mechanical wavepacket, with a mean deBroglie wavelength $\lambda_{dB} = 2\pi\hbar/mv$, the control afforded over the velocity of the atom with laser manipulation techniques translates directly into control of the mean deBroglie

6

wavelength of the wavepacket. Laser cooled and manipulated sources offer the best means of obtaining incoherent, but highly monochromatic, sources of deBroglie waves. Viewed in this light, Doppler sensitive Raman transitions are a means of preparing uncertainty principle wavepackets of spatial width $\Delta x \sim \hbar/\Delta p$, where Δp is the momentum spread associated with the velocity spread of atoms contributing to Raman resonance. For the experiment described in section 4, the width Δx was ~ 50 μm.[6]

1.2.1 *Atom Interferometry*

The $\pi/2$-π-$\pi/2$ experiment described in section 1.1.2, when considered in terms of the center of mass motion of atomic wavepackets, constitutes a matter-wave interferometer: conservation of momentum between the light and the atom leads to a one-to-one correlation between a wavepacket's mean momentum and its internal state.[27] The geometry is analogous to a Mach-Zehnder interferometer for light. The first $\pi/2$ pulse acts as a "beamsplitter" which produces two spatially coherent wavepackets of differing velocity. For example, when an atom initially prepared in hyperfine state $|1\rangle$ is driven into a coherent superposition of hyperfine states $|1\rangle$ and $|2\rangle$ with a velocity sensitive stimulated Raman transition, the $|2\rangle$ state drifts away from the $|1\rangle$ state with mean velocity $2\hbar k/m$. The subsequent π pulse a time T later switches the internal state of each wavepacket by driving the transitions $|1\rangle \rightarrow |2\rangle$ and $|2\rangle \rightarrow |1\rangle$. Momentum exchange with the light field "reflects" each wavepacket so that the two wavepackets drift together. A time T later, the wavepackets overlap spatially, but do not yet interfere as each wavepacket is correlated with a different internal atomic state. A final $\pi/2$ pulse mixes the internal states to allow interference by driving the $|1\rangle$ state into a coherent superposition of $|1\rangle$ and $|2\rangle$ and the $|2\rangle$ state into a similar superposition state. It plays the role of a final "beamsplitter" in a Mach-Zehnder type interferometer. A more precisely analogous optical system is a Mach-Zehnder interferometer made with acousto-optic deflecting elements, in which, for example, the unshifted frequencies correspond to a wavepacket in state $|1\rangle$ and the shifted frequencies to a wavepacket in state $|2\rangle$.

We demonstrated the interferometer for two geometries: the Mach-Zehnder geometry where the mean velocity of the atom is perpendicular to the momentum recoil

kick, and the gravimeter configuration, where the mean velocity lies parallel to the Raman beam propagation axis. In the Mach-Zehnder geometry, we observed maximum wavepacket separations of 84 μm, and were limited by the size of the beam used to drive the Raman pulses. Had the pulses been applied at the apex of the fountain, a 3 cm diameter beam would have allowed a 4.7 mm wavepacket separation. In the gravimeter configuration, interference was observed for wavepacket separations as large as 6 mm, where 100 msec separated the $\pi/2$ pulses from the π pulse.

In 1991 three other groups demonstrated matter-wave interference with atoms. Two groups used micro-fabricated gratings: one built an analogue to Young's double slit experiment[28] and the other used a three grating configuration again analogous to a Mach-Zehnder interferometer.[29] The remaining group used light pulses in a sequence of four $\pi/2$ pulses.[20] The long drift time T between pulses in our atomic fountain based interferometer afforded significantly larger wavepacket separations (6 mm vs. 30 μm).

Viewing the $\pi/2$-π-$\pi/2$ pulse sequence as an interferometer places the experiment in the broader context of past matter-wave interference experiments with neutrons and electrons, as well as earlier proposed experiments for atoms. In 1954 Marton first demonstrated interference with electrons by diffracting electrons from three successive gratings formed from epitaxially grown Cu films.[30] In 1974 Rauch, Treimer and Bronse demonstrated interference with neutrons by diffracting neutrons from three gratings carved out of a piece of perfect crystal Si.[31] The perfect crystal Si neutron interferometer has since become a tool to perform tests of quantum mechanics. Of note are past demonstrations of the interferometer's sensitivity to gravity[32] and to the Earth's rotation[33] as well recent experimental observation of the Aharonov-Casher effect[34,35] (a geometrical phase shift resulting from the motion of a magnetic moment in an electric field which is analogous to the Aharonov-Bohm effect for electrons in magnetic fields). Similar experiments are accessible to atom interferometers. New tests of quantum mechanics seem feasible as a result of the fact that an atom possesses internal as well as external degrees of freedom. Finally, effects like the Aharonov-Casher effect can be probed with much higher resolution in atom interferometers.

1.2.2 *Atom resonators*

Atoms have yet to be made to resonate in a way analogous to light in a Fabry-Perot cavity. Nevertheless, progress has been made in this direction. A good mirror for *slow* atoms is a nearly resonant evanescent wave of light at a dielectric interface. An incident atom is polarized by a light field whose intensity is increasing exponentially with scale length $\ell \sim \lambda/[2\pi(n^2\sin^2\theta -1)^{1/2}]$ as the atom approaches the vacuum-dielectric interface.[36] Here λ is the wavelength of the evanescent light field, n is the index of refraction for the dielectric, and θ the angle of incidence for the light beam. The strong spatial gradient of the polarizing field leads to a repulsive force if the light is tuned to the blue of the atomic resonance. In 1990 we demonstrated for the first time a normal incidence mirror for slow atoms by dropping a sample of laser cooled atoms onto a horizontally oriented evanescent mirror. We observed the atoms to bounce twice before the detection background noise became larger than the signal.[37] In this work we noted that by replacing the flat surface with a curved surface, it should be possible to transversely confine as well as reflect the atoms. We have done a quantum mechanical analysis of this configuration and shown that with present laser cooling technology, a minimum of 10^4 modes are excited when atoms are initially loaded into such a resonator. An improved cooling mechanism may enable occupation numbers > 1 for a given mode if the atoms obey Bose statistics!

1.3 ULTRA COLD ATOM-SURFACE SCATTERING

The dynamics of atom-atom and atom-surface interactions are expected to exhibit new, non-classical features which result from the large deBroglie wavelengths of ultra-cold atoms.[38] For example, a slow atom incident on an abrupt, attractive potential will *reflect* from the discontinuity. This effect is in a sense dual to quantum tunnelling: whereas classical particles either reflect from or pass over a repulsive barrier, a quantum mechanical particle may tunnel through the barrier if its energy is less than the barrier height, but it may also reflect from the barrier if its energy is greater than the barrier height. A crude analogy is to that of a photon propagating in a medium of changing index of refraction.[39] For a step discontinuity, the mismatch in dielectric constants

9

leads to Fresnel reflection from the boundary, whether the dielectric constant increases or decreases.

A slow atom incident on a surface may quantum reflect from the attractive van der Waals/Casimir[40] potential. This system has been studied by many researchers in varying degrees of complexity.[41] The most simple-minded approach is to treat the atom-surface potential as rigid and one dimensional. Estimates of reflection coefficients are obtainable by direct integration of a one dimensional Schrödinger's equation. In this system there are actually two possibilities for reflection: (1) the atom quantum reflects from the attractive part of the potential or (2) the atom does not quantum reflect, but reflects rather from the repulsive barrier at the surface boundary. (For many systems (2) is strongly suppressed since the atom may dissipate energy to the surface when it hits the repulsive wall). Specular reflection due to mechanism (2) has been observed for H-He film scattering.[42] We have performed calculations for Na incident on a dielectric surface (LiF, for example) with the result that incident temperatures of ~ 10 nK - 100 nK (depending on the substrate) are needed to see quantum reflection coefficients of 10% due to mechanism (1).

One way of achieving such cold effective temperatures is to velocity select atoms from an ensemble of laser cooled atoms. We originally used traditional time-of-flight velocity selection techniques in the atomic fountain geometry: atoms were launched through two narrow slits separated by ~ 15 cm to define a narrow transverse velocity spread.[43] The scattering surface was oriented vertically to decouple gravity from the interaction. With this scheme we were able to select velocity ensembles as cold as 100 nK. We also could control the mean velocity of the selected ensemble by adjusting the relative positions of the slits. Unfortunately, we did not observe quantum reflection from the Na-BK7 glass system at 100 nK.

We were, however, able to observe a similar effect by modifying the attractive retarded van der Waals/Casimir potential with a repulsive, exponentially decaying potential. The exponential potential was produced by a totally internally reflected wave at the dielectric-vacuum interface which polarized the atom as the atom approached the surface. We could adjust the strength of the potential by varying the intensity of the

10
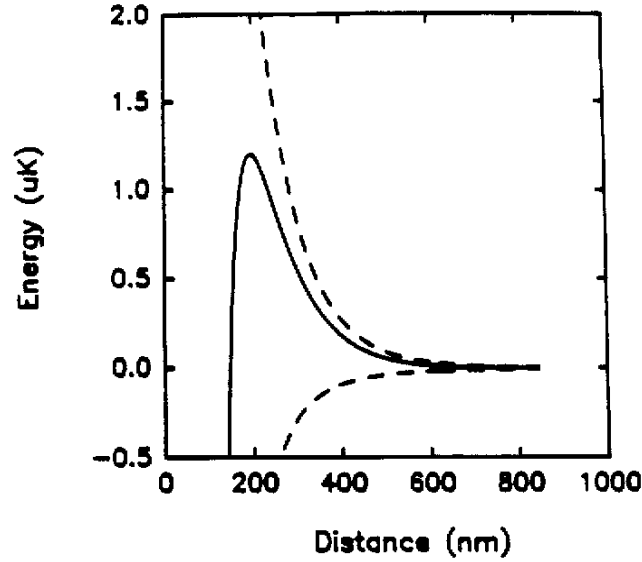
Fig. 1.2: Hybrid retarded van der Waals (Casimir)/evanescent wave surface potential. The lower dashed line is the retarded van der Waals contribution for sodium on BK7 glass. The upper dashed line is evanescent wave contribution for typical operating parameters. The solid line is the combined potential.

driving light or the detuning of the light from the atom's internal resonance. For strong repulsive evanescent potentials the surface behaved as a mirror and reflected nearly all incident atoms. At lower intensities, the potential seen by the ultra-cold atoms was a hybrid of the retarded van der Waals/Casimir and evanescent wave potential as shown in Fig. 1.2.

Fig. 1.3 shows the experimentally measured number of atoms reflected from the hybrid potential as a function of the strength of the evanescent wave potential, which varies inversely with the detuning of the evanescent wave. The incident velocity of the atoms was fixed at ~3 cm/sec and the velocity spread was ~0.5 cm/sec. The dashed line shows the classically expected result based on a retarded van der Waals/Casimir potential strength of $V_{Casimir} = -C_4/R^4$, with $C_4 = 3000$ eV-$Å^4$. The theoretical model accounts for a Gaussian intensity distribution for the evanescent patch on the prism
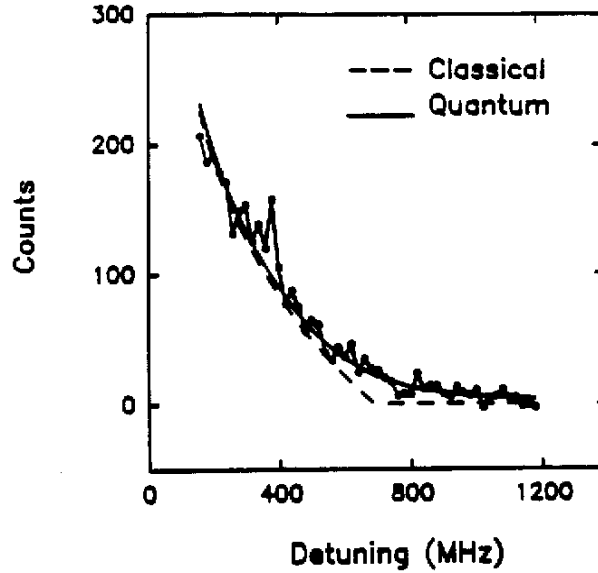
Fig. 1.3: Preliminary measurement of the reflection of ultra-cold atoms from the combined potential as a function of the frequency of the laser used to make the repulsive potential barrier (hence height of the combined potential). The dashed curve is a fit based on a model where the atom is treated as a classical particle. The solid line is a solution to the one-dimensional Schrödinger wave equation for a mono-energetic wave incident on a rigid potential barrier. Experimentally, no reflection was observed if the light responsible for the repulsive potential was turned off.

surface. The solid line is the corresponding quantum mechanical model, based on a solution of the one dimensional Schrödinger equation for a mono-energetic wave incident on a rigid potential barrier. The probability of sticking was inserted into the calculation by assuming that the potential never becomes repulsive close to the surface. No reflection counts were observed when the evanescent light was turned off (the BK7 prism was cooled to ~77 K).

This study also constituted a preliminary first measurement of the atom-surface retarded van der Waals/Casimir interaction. The quantum mechanical model did not fit

the data well when the value for C_4 was changed by 30%. The measured value agrees with the value calculated using the Lifshitz theory[44] of retarded van der Waals forces to within 20%.

We hope to improve these measurements dramatically by using velocity selective stimulated Raman transitions (discussed in section 4), rather than mechanical slits, to prepare the incident atomic ensemble. By varying the incident atomic velocity, evanescent wave scale length, and evanescent potential strength, we believe that we can map out the strength of the retarded van der Waals potential as a function of the atom's distance from the surface. We also hope to observe quantum reflection from the purely attractive van der Waals/Casimir potential.

This experiment is not discussed in detail in the sections which follow. It is included here to point to the wide range of applicability of the atomic fountain/laser manipulation techniques developed during the course of this research.

SECTION 2

LASER COOLING AND TRAPPING

The kinetic effects of light on atoms follow from conservation of momentum during the atom-light field interaction.[45] When an atom absorbs a photon of momentum $\hbar k$, the velocity of the atom must change by $m\Delta v = \hbar k$, where m is the mass of the atom and Δv is the change in velocity of the atom. Momentum exchange may also be viewed classically, where the atom is seen as a polarizable oscillator in a time varying electro-magnetic field. Quantum mechanics needs to be summoned to calculate the polarizability, but once calculated, the light forces follow from classical considerations. For the purposes of this chapter, and understanding of future chapters, we will shamelessly mix views. Rigorous treatments exist in the literature. The aim here is to present nearly valid models which convey intuitively appealing explanations of the processes involved. In this section we briefly review the laser cooling and trapping background necessary for understanding the experiments presented in subsequent sections.

2.1 LIGHT FORCES FOR TWO-LEVEL ATOMS

For a two-level atom in a nearly resonant *travelling-wave* light field, the atom-field momentum exchange arises through the scattering force.[46] During the resonance fluorescence scattering cycle, which takes an atom from its ground state via a stimulated absorption and returns the atom to its ground state through a spontaneous emission,[47] the momentum of the atom changes by an average amount $\langle \Delta p_{atom} \rangle = \hbar k$, where k is the propagation vector for the travelling wave. On average, there is no net momentum transfer arising from spontaneous emission: the atom is equally likely to emit into the $\hbar k'$ field mode as the $-\hbar k'$ mode. In the classical limit this follows from the symmetry inherent in the dipole radiation pattern of a driven oscillator.

The rate of momentum transfer, hence force, is given by the rate of absorption

from the light field and the size of the momentum kick. In the limit where the atom is exposed to the radiation for a time much longer than its natural lifetime τ_n, the probability for spontaneously scattering a photon in the time τ_n is equal to the probability σ_e of finding the atom in the excited state. Thus, the mean time between scattering events, τ_{scat}, is

$$\tau_{scat} = \frac{\tau_n}{\sigma_e} \quad .$$ (2.1)

For a saturated atom, $\sigma_e = 1/2$, so the mean time between photon scattering events is $\tau_{scat} = 2\tau_n$. Thus $f_{scat}^{max} = \hbar k/(2\tau_n)$ is the maximum force that a travelling wave can exert on the two-level atom. For sodium, this translates into a maximum acceleration of $a_{scat}^{max} = f_{scat}^{max}/m = 9.5 \times 10^5 \text{ m/s}^2$ ($m_{Na} = 23 \times 1.67 \times 10^{-27}$ kg, $\tau_n = 16$ nsec, and $\lambda = 2\pi/k = 589$ nm).

Often it is neither practical nor desirable to saturate the atom. In this case, the full expression for the steady state population is needed. This is obtained, for example, by solution of the optical Bloch equations[48,49] with the result that

$$\sigma_e = \frac{1}{2} \frac{\frac{I}{I_{sat}}}{1 + \frac{I}{I_{sat}} + 4\left(\frac{\Delta}{\Gamma}\right)^2} \quad ,$$ (2.2)

where

$$\frac{I}{I_{sat}} = 8\frac{|\Omega_r|^2}{\Gamma^2} \quad ,$$ (2.3)

$$\Omega_r = \frac{\mu \cdot E}{\hbar} \quad ,$$ (2.4)

and where Ω_r is the Rabi frequency, $\Gamma = 1/\tau_n$ is the natural linewidth, $\mu = \langle 1|r|2\rangle$ is the dipole matrix element, $E\cos(\omega t + \phi)$ is the electric field, and $\Delta = \omega - \omega_0$ is the

detuning from resonance (ω is the frequency of the light field in the rest frame of the atom, and ω_0 the atom's resonance frequency). The resulting expression for the scattering force is

$$f_{scat} = \hbar k \Gamma \left[\frac{1}{2} \frac{\dfrac{I}{I_{sat}}}{1 + \dfrac{I}{I_{sat}} + 4\left(\dfrac{\Delta}{\Gamma}\right)^2} \right] \quad . \tag{2.5}$$

Next consider an atom in a time varying electric field of frequency nearly resonant with the atom's internal resonance which also possesses a spatial variation in its intensity. Examples of such fields are those of standing wave light fields or those arising from total internal reflection at a dielectric interface. In this case, the shift $\hbar \Omega_{AC}$ in the atom's internal energy arising from the interaction of the induced dipole moment of the atom with the driving electric field (the AC Stark shift) varies with the intensity of the field, giving rise to the so-called dipole force:

$$f_{dipole} = -\nabla (\hbar \Omega_{AC}) \quad , \tag{2.6}$$

and

$$\Omega_{AC} \approx \frac{\Omega_r^2}{\Delta} \quad . \tag{2.7}$$

Eqs. (2.6) and (2.7) are valid in the limit where the detuning $\Delta \gg \Gamma$.

The dipole force may also be interpreted in terms of cycles of stimulated absorption and emission, ie. intrabeam coherent scattering.[46] Momentum exchange in a standing wave configuration, for example, can be thought of in terms of absorption from a travelling wave component incident from one direction followed by a stimulated emission into the other travelling wave. In an evanescent light field or tightly focussed laser beam the electric field may be decomposed into a continuum of spatial Fourier components. The dipole force is then a manifestation of photon redirection between these existing modes via stimulated processes.

16

Yet another powerful model for understanding dipole forces comes from the dressed state picture of the atom-field interaction.[50] In this picture, the atom and the field are treated on equal footing in the Hamiltonian for the entire atom+field system. The undressed basis states are atom in ground state, n photons in the field, and atom in excited state, n-1 photons in field. The so-called dressed states which diagonalize the Hamiltonian give the spatial dependence of the internal energy of the atom as well as the new eigenstates. The AC Stark shift in Eq. (2.7) is the dressed state energy shift in the limit $\Omega_r \ll \Delta$.

Dipole forces are conservative. Scattering forces are dissipative. Dipole forces alone can not cool an atomic ensemble. On the other hand, the scattering force dissipates energy by irreversibly coupling to vacuum field modes. In a classical model of the atom, the two forces can be unified by taking the polarizability of the atom to be a complex quantity.[51]

When we speak of forces we are usually invoking a semi-classical approximation in the sense that we are referring to the atom's center of mass coordinates as continuous classical variables. This is a good approximation when the atom is well localized on a scale length comparable to the wavelength of light. In this limit, general expressions are obtainable for the forces for arbitrary field configurations and intensities by solving density matrix equations for the internal state of the atom at a particular point in an electromagnetic field. Usually the fields are also treated classically, that is as coherent states, with the usual approximation which decouples the density matrix operators for the atom's internal degrees of freedom from the electro-magnetic field operators. More general treatments (i) quantize atomic motion[52] and/or (ii) treat electro-magnetic field states which are other than coherent states.[53] As laser cooling techniques continue to evolve a third approach (iii) consisting of a quantum many body treatment of atomic center of mass variables may be needed. Approach (i) has become necessary with the advent of ultra-cold atoms whose temperatures are such that the Heisenberg uncertainty in position $\Delta x \sim \Delta p/\hbar \rightarrow \lambda$. Approach (ii) is used in speculative studies, for example, of diffraction of atomic wavepackets from number field states. Approach (iii) will be necessary when the density of atomic states becomes large enough that the Bose or Fermi

17

statistics of the atoms needs to be considered. Most of the experimental work described below can be considered in the context of the simple considerations of the previous paragraphs.

2.2 DOPPLER COOLING

The motion of a two-level atom can be damped when the atom is irradiated by counter-propagating laser beams tuned to the red of the transition. This arises because the scattering force has a *velocity dependence* arising from the Doppler effect:[1,54] the detuning $\Delta = \omega - \mathbf{k} \cdot \mathbf{v} - \omega_{atom}$ in the rest frame of the atom. When the laser beams are tuned to the red of the resonance, the atom will Doppler shift the beam toward which it moves into resonance, while the beam from which it moves gets Doppler shifted out of resonance. This leads to a preferential absorption from the blue shifted beam (due to the net red detuning of the laser) for Doppler shifts smaller than the laser's detuning from resonance, and thus to a velocity dependent damping force which always opposes the atom's motion. The idea generalizes to three dimensions by using three pairs of mutually orthogonal beams.

From a thermodynamic perspective the vacuum electromagnetic field is playing the role of a heat bath, and the reduction in the atom's kinetic motion can be seen as a consequence of its thermalization with the bath. The question then arises, What is the ultimate temperature of the atom? The answer, based on a rigorous solution of a Fokker-Planck equation governing the evolution of an ensemble of atoms in this type of light field,[55] is that the ultimate temperature is limited by the natural linewidth of the transition: $k_b T_{Dopp} \sim \hbar \Gamma$.

There is a simple physical picture for this result.[54,56] As the atom scatters photons, its velocity diffuses as a result of the atom-field momentum exchange during the spontaneous relaxation. This part of the cycle can be modelled as a random walk in the momentum space of the atom. In a simple 1-D model, treating momentum diffusion as a random walk with step size $\pm \hbar k$, the rate of kinetic energy increase is

$$\left.\frac{dE}{dt}\right|_{heat} = \frac{1}{m}\left.\frac{dp^2}{dt}\right|_{heat} = 2\left(\frac{Photons\ scattered}{unit\ time}\right)\frac{(\hbar k)^2}{m} \quad . \qquad (2.8)$$

A factor of 2 enters above because an atom nearly at rest is as equally likely to absorb a photon from one direction as the other, so each absorption-emission cycle corresponds to two random walk steps. In equilibrium the rate of energy increase is balance by the rate of energy decrease due to the cooling force. The cooling rate is

$$\left.\frac{dE}{dt}\right|_{cool} = \left(f^1_{scat} + f^2_{scat}\right)\cdot v \quad , \qquad (2.9)$$

in the low intensity limit (so that the scattering forces for the two beams, indexed by superscripts in the previous equation, are additive). Equating Eqs. (2.8) and (2.9), and substituting expressions for the scattering force from Eq. (2.5) (after expanding the expression to first order in velocity), leads to an expression for the equilibrium kinetic energy of the atom in terms of the detuning of the laser from resonance and the natural linewidth of the resonance. The kinetic energy is minimized for $\Delta = -\Gamma/2$, and can expressed as a temperature

$$k_B T_{Dopp} = \frac{\hbar\Gamma}{2} \quad . \qquad (2.10)$$

The Doppler limit for sodium is 240 μK. Parenthetically, the Doppler shift due to an atom moving with a velocity at the Doppler limit is $k\cdot v_{Dopp} = [(\hbar k^2/m)\Gamma]^{1/2} \ll \Gamma$. On the other hand, the scattering force is no longer effective when the atom's velocity leads to a Doppler shift which is on the order of the natural linewidth of the resonance.

The above considerations can be recast in the language of Brownian motion.[2] The momentum diffusion rate $d\langle p^2\rangle/dt = 2D_p$, where D_p is the momentum diffusion constant. The damping force can be written in the form $f = -\alpha v$. The Einstein relation for Brownian motion gives the temperature $k_b T = D_p/\alpha$. In addition to being cooled by the light fields, the atoms are also viscously confined spatially. The rms displacement after a time Δt for a particle undergoing Brownian motion is $\langle x^2\rangle = (2k_b T/\alpha)\Delta t$. This has the

important consequence that the diffusion time is long enough to allow atoms to come into equilibrium with the light.

During the cooling process the kinetic energy of the atom goes into the light field. For each emission/absorption event

$$<\Delta E_{atom}> = \frac{\langle(p+\hbar k)^2\rangle}{2m} = \frac{p^2}{2m} + \frac{(\hbar k)^2}{2m} + \frac{\hbar<p \cdot k>}{m} \quad . \tag{2.11}$$

The brackets indicate an averaging over all possible emission angles for an outgoing spontaneously emitted photon. The change in the atom's kinetic energy in an absorption-emission cycle is $\hbar p \cdot k/m + (\hbar k)^2/2m$. When p opposes k, the atom absorbs a photon of frequency of ω but emits, on average, a blue shifted photon. Note, however, that on average, the energy of an atom initially at rest *increases* as a result of the cycle by an amount

$$E_{Rec} = \frac{(\hbar k)^2}{m} \quad , \tag{2.12}$$

known as the photon recoil limit. This limit, however, is not fundamental -- it is an artifact of considering energy balance in the average. Recent experiments by Aspect, *et. al.*[57], and Kasevich and Chu[7] have demonstrated cooling below the recoil limit.

2.3 LASER COOLING MULTI-LEVEL ATOMS

In 1989 the NIST group discovered that sodium atoms could be cooled to temperatures an order of magnitude colder than the Doppler limit.[58] Subsequently, Dalibard and Cohen-Tannoudji[59] and independently Chu and coworkers[60] developed new theories of laser cooling which explained these startling results. Explanations aside: the NIST discovery had important consequences for the work in this thesis. Higher velocity phase space densities meant higher count rates for the atomic fountain based experiments.

The essential point of departure for the new "polarization gradient" theories is that rich new complexities present themselves when the atom is treated as a multi-level

system. The new theories integrate the effects of optical pumping with the dipole and scattering forces considered above. In particular, the mechanism of optical pumping introduces new paths for energy transfer from the atom to the light field.

Consider the groundstate populations of a multi-level atom such as sodium. If the population is initially prepared in the $F=2$, $m_f=-2$ Zeeman sub-level and if the atom is irradiated with *low intensity* light polarized σ^+, the transition oscillator strengths are such that the population will "optically pump" to the $m_f=+2$ Zeeman sub-level -- the sub-level with the strongest coupling to the excited state.[61] Analogously, if linearly polarized light is applied, the atom will pump predominantly into the $m_f = 0$ state. Mathematically this follows directly from a rate equation analysis (the intensities are low).[62] The steady state population is of course independent of the initial population. The time scale for the approach to equilibrium τ_p (the optical pumping time) is proportional to the excitation rate of the atom.

The AC Stark shifts of the Zeeman sub-levels are also proportional to the coupling strength to the excited state (see Eq. 2.7). With the detuning of the laser to the red of the optical transition, the optically pumped level is also the lowest energy sub-level (ie. the AC Stark shift lowers the energy of the ground state levels for red detuning and the magnitude of the AC Stark shifts scales linearly with the oscillator strength of the transition in the low intensity limit).

Next consider the behavior of an atom in a light field comprised of counter-propagating beams with crossed linear polarizations. The local polarization of the combined field changes from σ^- to linear to σ^+ to linear in $\lambda/4$ steps along the propagation axis of the light. Thus an atom moving parallel to the laser beams will see changes in the polarization. Here is the important point: when the atom moves from one region of polarization to another in a time shorter than or comparable to the optical pumping time, τ_p, it costs the atom energy in AC Stark shifts. Suppose an atom is initially in steady state equilibrium with σ^+ polarization, for example, and is therefore optically pumped into its lowest energy sub-level. Moving the atom to a region of different polarization necessarily increases the internal energy of the atom: the internal polarization of the atom is no longer optimally phased with the driving field. This

energy is taken from the center of mass motion of the atom. However, at this new location the atom tends to optically pump into equilibrium with the new field polarization. This tends to transfer the atom's internal energy to the light field as it pumps into the low energy Zeeman sub-level. Crucially, the optical pumping *irreversibly dissipates* the extra internal energy accrued in moving to the new location.

The force resulting from the above process, known in the literature as the "Sisyphus" force, is velocity dependent since the amount of energy transferred from the external degrees of freedom to the internal energy levels of the atom depends on the distance the atom can travel in the light field before the optical pumping dissipates the energy. An order of magnitude estimate is given by

$$f_{sys} \approx -\left\langle \frac{dU_{AC}}{dx} \right\rangle_{v\tau_p} = -\langle f_{dipole} \rangle_{v\tau_p} \quad . \tag{2.13}$$

The brackets indicate an average over the distance travelled by the atom in an optical pumping time. Approximating the spatial dependence of $U_{AC}(x)$ by

$$U_{AC}(x) \approx -\hbar \Omega_{AC} \left[1 - \left(\frac{x}{\lambda/4} \right)^2 \right] \quad , \tag{2.14}$$

where the expression for Ω_{AC} is given in Eq. (2.7). Performing the average gives

$$f_{sys} \approx \hbar k^2 \left(\frac{\Delta}{\Gamma} \right) v \quad , \tag{2.15}$$

where we have taken the large detuning limit, approximated the optical pumping time $\tau_p \sim 1/(\Gamma \sigma_e)$, and considered small $v\tau_p$ only. For velocities larger than $v_c \sim \lambda/\tau_p$ this force averages to zero. The Doppler friction force, however, is still present.

To estimate the ultimate temperature in this configuration we need an estimate of the momentum diffusion constant D_p. The dominant contribution no longer arises from the random scattering model used to estimate the Doppler cooling temperatures.[59] Again we need to consider the motion of an atom at rest at a given position in the light field. Suppose the atom is at rest in a position of linear polarization. The steady state

22

population distribution is peaked for the $m_f = 0$ state, but there is a finite probability the atom finds itself in another sub-level. When the atom resides in a $m_f \neq 0$ sub-level, it feels a dipole force $\sim dU_{AC}/dx$ which acts for a time on the order of τ_p, transferring momentum in steps of size $\Delta p \sim \tau_p(dU_{AC}/dx)$. This force reverses sign when the Zeeman sub-level reverses sign, thus leading to a random walk type of behavior as the internal state of the atom fluctuates. The diffusion coefficient is $D_p \sim (\Delta p)^2/\tau_p \sim \tau_p(\hbar\Omega_{AC}/\lambda)^2$. Thus the temperature, given by D_p/α, scales as

$$k_B T_{sys} \propto \frac{\hbar\Omega_R^2}{\Delta} \quad . \tag{2.16}$$

This is an important heuristic result for experimental work: to achieve lowest temperatures, reduce the intensity of the laser light and/or increase the detuning of the light field if the light fields have "polarization gradients."

Eq. (2.16) ought not to be interpreted to mean that the temperature can be reduced to arbitrarily low values. For example, at low enough temperatures the atoms can become confined in AC Stark shift potential wells. At this level, a complete understanding requires a quantum mechanical treatment of the atom's position coordinates.[63] Experimentally, equilibrium momentum spreads as low as $\Delta p_{min} \sim 3\text{-}4$ $\hbar k$ are routinely achievable for a number of atomic species (eg. Cs, Na, Rb).

To complete the picture of laser cooling of multi-level atoms, one final mechanism deserves mention. The scattering force, in certain circumstances, is enhanced by the optical pumping process. Consider an atom in a light field comprised of counter-propagating laser beams polarized $\sigma^+\sigma^-$. In this case, the local electric field is always linear in polarization, but the direction of the polarization axis rotates by one full cycle per wavelength of light. The enhancement arises because motion of the atom induces population asymmetries in the ground state Zeeman sub-levels for velocities less than v_c (defined above) which tends to further favor scattering from the blue shifted beam. A Sisyphus type force exists for this light field but it turns out to be much weaker than the force arising from motionally induced population imbalance.

The diffusion of momentum is also altered in the low velocity limit:[64,65] the momentum step size in the random walk is leveraged up for a reason similar to that leading to the enhancement in the cooling force. Once the atom has absorbed a photon from one direction, it is more likely to absorb again from that direction than from the counter-propagating direction. In spite of the differences between this cooling mechanism and the Sisyphus mechanism, the temperature scaling D_p/α is the same in the large detuning limit. The critical velocity is similar to that estimated for the Sisyphus mechanism. For velocities much greater than λ/τ_p, the internal populations can not respond to the changing polarization orientations.

In summary, the theory of laser cooling of multi-level atoms has introduced two qualitatively new forces. These forces allow atoms to be cooled to temperatures well below the classical Doppler limit. These two new forces can be introduced into a quasi-classical framework by considering the polarizability of the atom to be a *tensor* quantity. Subsequent evaluation of the resulting force produces four terms: (i) the two-level scattering force (ii) the dipole force (iii) the motionally-induced population imbalance scattering force and (iv) the Sisyphus force.[51]

A final word of caution. The theory of cooling for multi-level atoms is still an area of active research. The simple explanations given above were for one dimensional field configurations, although similar principles should apply to three dimensional configurations. The recent development of powerful numerical techniques[66] have enabled numerical studies of two and three dimensional geometries.[67]

2.4 MAGNETO-OPTIC TRAPPING

Laser cooling viscously confines atoms. It does not provide a force which tends to localize to a single point in space. A magnetic field gradient, however, can induce long range ($\ell \gg \lambda$) spatially dependent forces which lead to localization. The mechanism is through spatially dependent Zeeman shifts of the atom's internal states which, in appropriately polarized and detuned light fields, generate spatially induced anisotropies in the light scattering forces.

Fig. 2.1 shows a one dimensional "magneto-optic trap." The magnetic field has
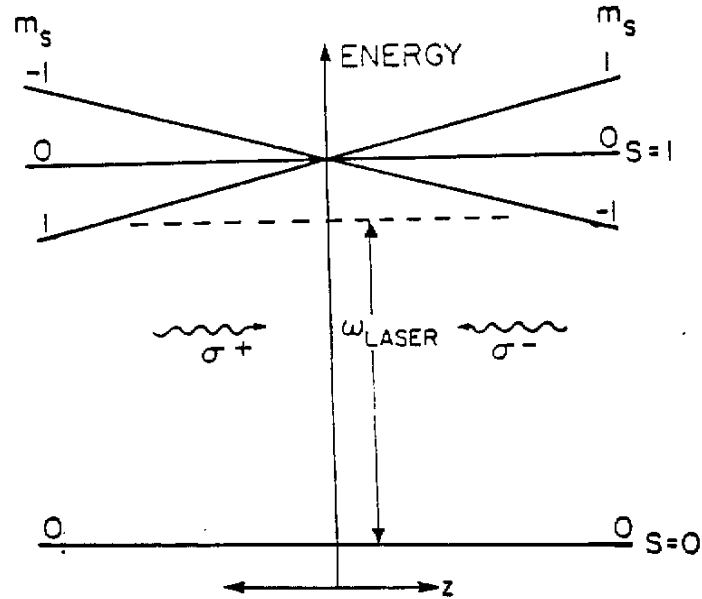
Fig. 2.1: Magneto-optic trapping in 1-dimension.

a zero at x=0, and the direction of the field is collinear with the gradient. The counter-propagating light beams are tuned to the red of the atomic resonance and polarized $\sigma^+\sigma^-$. For simplicity, the atom is taken to have an S=0 ground state and an S=1 excited state. The light's polarization ensures that the σ^+ beam couples only to the $m_f = +1$ level in the excited state while the σ^- beam couples only to the $m_f = -1$ level. Thus an atom to the left of the origin will feel a scattering force predominantly from the σ^- beam tending to push the atom toward the origin, since the Zeeman field shifts the $m_f = -1$ transition into resonance while shifting the $m_f = +1$ transition out of resonance. Similarly, an atom to the right of the origin feels a restoring force from the σ^+ beam. Near the origin of the trap, the effects of the magnetic field on the scattering forces are minimal. There remains, however, a damping force which arises from the velocity dependence of the scattering force. The magneto-optic trap not only localizes atoms, it also cools them.

These principles presumably underlie the operation of the three-dimensional version of the trap for atoms with $S > 1$. A spherical quadrupole magnetic field (formed by two oppositely sensed current loops separated by approximately a loop radius) generates the required field gradients in three-dimensions. $\nabla \cdot \mathbf{B} = 0$ implies $|\partial B_z / \partial z| = 1/2 |\partial B_y / \partial y| = 1/2 |\partial B_x / \partial x|$, and symmetry considerations require $B_\alpha \parallel \partial B\alpha / \partial \alpha$ ($\alpha = x,y,z$) in the x-y plane and along the z-axis (the z axis is taken parallel to the symmetry axis of the coils). The light field is configured with three mutually orthogonal beam pairs polarized $\sigma^+ \sigma^-$ along each of the three gradient axes. With this configuration Chu, Pritchard and collaborators demonstrated trapping of sodium in 1987.[4]

Subsequent research has shown that the dynamics of the trap are significantly more subtle than one would expect from the simple arguments presented above. A few general considerations, however, can aid in optimization of the trap performance.

(1) The trap loading time can be modelled by a rate equation expressing competition between the trap loading rate and the trap loss rate. Neither the loading nor the loss mechanisms are fully understood. The loading rate, however, is proportional to the flux of pre-cooled atoms into the trapping volume. The loss rate is limited in part by collisions with background gas elements (proportional to the background pressure of the vacuum system). For more trapped atoms, increase the flux of pre-cooled atoms and lower the pressure.

(2) The dynamics are affected by radiation trapping and laser beam attenuation when the density of trapped atoms becomes high enough that the vapor becomes optically thick.[68] The radiation trapping leads to a repulsive force, with inverse square law scaling, between pairs of trapped atoms. This force is believed to limit the final density of atoms. Beam attenuation introduces strong restoring forces in addition to the magnetic field induced force. An atom at one edge of the trap, for example, feels a stronger scattering force from the beam which does not have to travel through the trap's center to reach the atom.

(3) Polarization gradient light forces are present.[69] The 3-D $\sigma^+ \sigma^-$ beam geometry produces a light field with spatially varying polarization. Near the magnetic field zero, the AC Stark shifts from the light field can be much larger than the Zeeman

26

shifts of the atomic levels (typical trapping gradients are 1 G/mm, and trap sizes are ~ 1 mm). Thus we expect polarization gradient cooling mechanisms to play an important role in this region.

Although not entirely understood, the magneto-optic trap reliably produces ensembles of cold atoms. At present, it is the best method of obtaining high densities and numbers of trapped,[70] cold atoms.

2.5 LASER COOLING OF SODIUM

The purpose of this section is to summarize the parameters relevant to laser cooling of sodium as well as indicate qualitatively where the basic theory presented in the previous sections diverges from what is needed for a full description of laser cooling of sodium.

Fig. 2.2 shows the relative oscillator strengths and energy separations for the hyperfine transitions of the $3S_{1/2} \rightarrow 3P_{3/2}$ manifold. The natural lifetime of the excited state is $\tau_n = 16$ nsec which corresponds to a natural linewidth of $\Gamma = 10$ MHz. The saturation intensity I_{sat} (see section 2.1) is 6.3 mW/cm^2 for the "stretched" $F = 2$, $m_f = \pm 2 \rightarrow F = 3$, $m_f = \pm 3$ transitions. The relative matrix elements and their signs are tabulated in Appendix A. Typically the cooling and trapping lasers are tuned just red of the $F = 2 \rightarrow F = 3$ transitions.

External magnetic fields remove the degeneracy of the hyperfine levels via Zeeman shifts. The Bohr magneton, $\mu_B = 1.4$ MHz/Gauss, sets the scale for the size of these shifts is the weak field limit. In particular, the shift of the $\Delta m_f = 0$ groundstate hyperfine transition frequency is $m_f \mu_b B$ for $m_f \neq 0$. The $m_f = 0 \rightarrow m_f = 0$ shift is second order in B, with $\Delta E = \hbar \alpha B^2$, and $\alpha = 2.21$ mHz/mGauss^2. In general, the polarization gradient molasses cooling mechanisms produce the coldest temperatures when the residual magnetic field is less than 100 mGauss. In some cases a properly directed bias field may lead to a polarization gradient-type cooling when the atoms are illuminated with properly polarized light (so-called magnetic orientational cooling).[64] The presence of the bias field may also be used to shift the mean velocity of the laser cooled ensemble.[71] To date these mechanisms have only been studied for one-dimensional

27
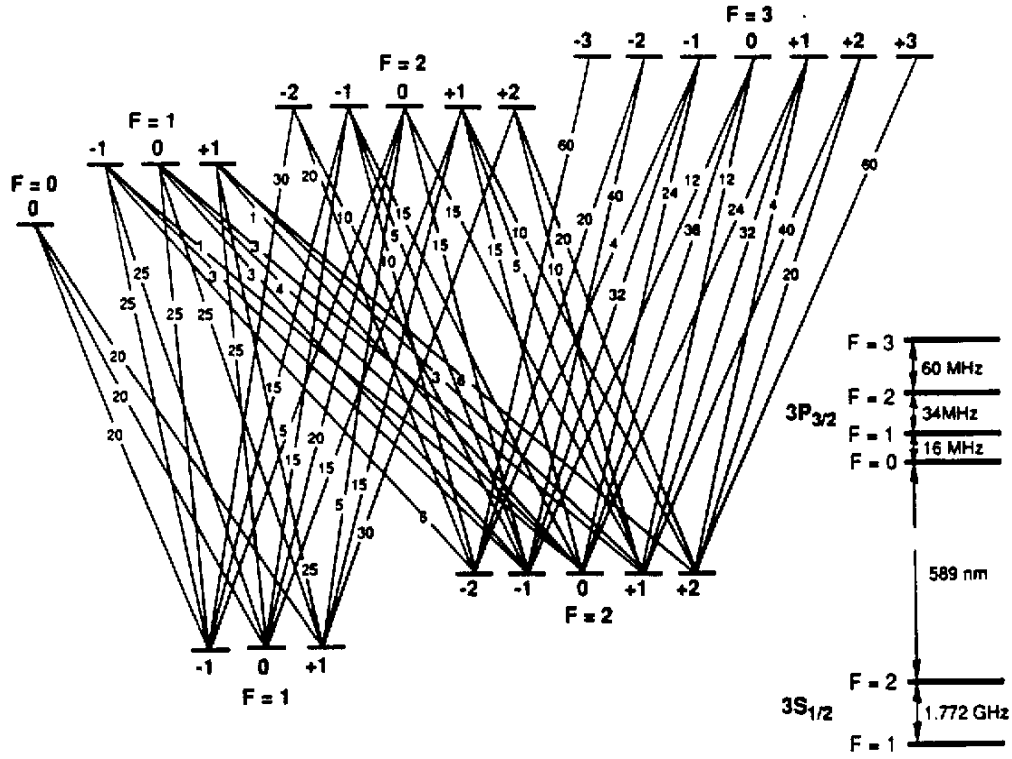
Fig. 2.2: Oscillator strengths and energy separations for the sodium $3S_{1/2} \to 3P_{3/2}$ hyperfine transitions.

configurations.

Off-resonant excitation of the F=2 → F=2 transitions in optical molasses tends to optically pump atoms into the F=1 groundstate if the driving laser field has only one spectral component. When the atom optically pumps into the F=1 state it is no longer coupled to the light field and the laser cooling mechanisms described above turn off. For sodium this happens on a time scale which is much faster than the time required for the atoms to fully cool. To keep the atoms from pumping into the F=1 state, some "repumping" light, tuned typically from the F=1 → F=2 transition, is used to re-excite atoms from the F=1 state. In our experiments we generated the repumping light with an electro-optic modulator driven at the 1.7 GHz hyperfine interval. For sodium, the lowest temperatures are achieved when the repumping beam has ~20% of the power of the main cooling beam and is tuned to be resonant with the F=1 → F=2 transition.[64]

Other alkalies, such as cesium, require much lower repumping intensities, due to a much weaker off-resonant excitation rate. The presence of the extra spectral component significantly complicates the theory, and some researchers have speculated that Raman process between hyperfine levels may play an important role in the cooling process.[72,73]

SECTION 3

ATOMIC FOUNTAIN

By combining the laser cooling and trapping techniques described in section 2, ensembles of atoms localized to a few mm spatially of temperature $\sim 30 \, \mu K$ (for Na) are routinely achievable. At $30 \, \mu K$, the corresponding velocity spread is $\sim 30 \, cm/sec$. For time scales on the order of 1 sec, the change in velocity of the ensemble due to gravity is much larger than the initial spread in velocity: ie. gravity is a dominant perturbation on the velocity of the atoms. In this limit, one can think of creating a fountain of atoms by launching the laser cooled ensemble vertically at speeds low enough that gravity turns them around within the confines of the apparatus.

This geometry has a number of benefits for experiments with cold atoms. (1) From the perspective of precision spectroscopy, the fountain geometry doubles the maximum interaction time for an apparatus of fixed height. (2) The fountain geometry provides perhaps the best means of extracting a sample of cold atoms from the not-so-benign environment of a magneto-optic trap and transporting them to another spatial region where they can again be nearly at rest for long periods of time (at the apex of their ballistic trajectory). For precision spectroscopy this reduces, for example, systematic shifts from residual trapping magnetic fields. For low count rate experiments, it greatly reduces background counts arising from untrapped atoms. When the atoms are initially trapped in a vapor cell,[74] it allows cold atoms to be separated from untrapped atoms by launching them into a differentially pumped high vacuum cell. (3) Finally, when an atom is launched vertically on a ballistic trajectory it passes through a given spatial region twice: once on the way up, and again after it has turned an is falling back to earth. In high resolution spectroscopy, techniques such as Ramsey's method of separated oscillatory fields[12] require an atom to interact with the probing radiation twice. For non-fountain geometries (ie. conventional atomic clocks) two nearly identical interaction regions need to be constructed. In the fountain geometry, one region serves

double purpose. This reduces systematic errors which otherwise arise from slight asymmetries between two independent regions.

The aim of this chapter is to convey the operating principles of the fountain source which has formed the core of a series of experiments with laser cooled atoms. Section 3.1 outlines the basic operating principles of the fountain source, including the techniques used to launch atoms. Section 3.2 provides a detailed description of the apparatus. Section 3.3 presents results demonstrating the successful operation of the fountain.

3.1 BASIC OPERATING PRINCIPLES

The atomic fountain operated in a pulsed mode. Each pulse of atoms was generated from a three step sequence which consisted of loading a magneto-optic atom trap, then cooling the trapped atoms in an a polarization gradient optical molasses, and finally launching the cooled atoms vertically.

Atoms in a thermal atomic beam were initially slowed by the scattering force from a resonant, counter-propagating laser beam, as shown in Fig. 3.1. The frequency of this beam was chirped by an electro-optic modulator to stay in resonance with the atom as it decelerated to near zero velocity. A magneto-optic trap, consisting of a spherical quadrupole magnetic field and six laser beams, collected the slowed atoms. The laser beams were configured in three mutually orthogonal pairs of counter-propagating, circularly polarized laser beams tuned to the $F=2$, $3S_{1/2} \rightarrow F=3$, $3P_{3/2}$ sodium transition. Two ~ 10 cm diameter coils were used to generate the spherical quadrupole field. A second electro-optic modulator was used to impose 1.712 GHz sidebands on the trapping/slowing beams. The high-frequency sideband re-excited atoms which were optically pumped into the $F=1$, $3S_{1/2}$ level. The trapping magnetic field was turned off after a substantial number of atoms had collected in the trap. This left the atoms in a polarization gradient molasses light field which had the effect of further cooling the sodium atoms to temperatures of ~ 30 μK. Following this post-cooling period, the atoms were launched vertically on ballistic trajectories.

In the course of this research the launching technique evolved from the relatively crude method of pushing atom from below with a short pulse of resonant radiation to the
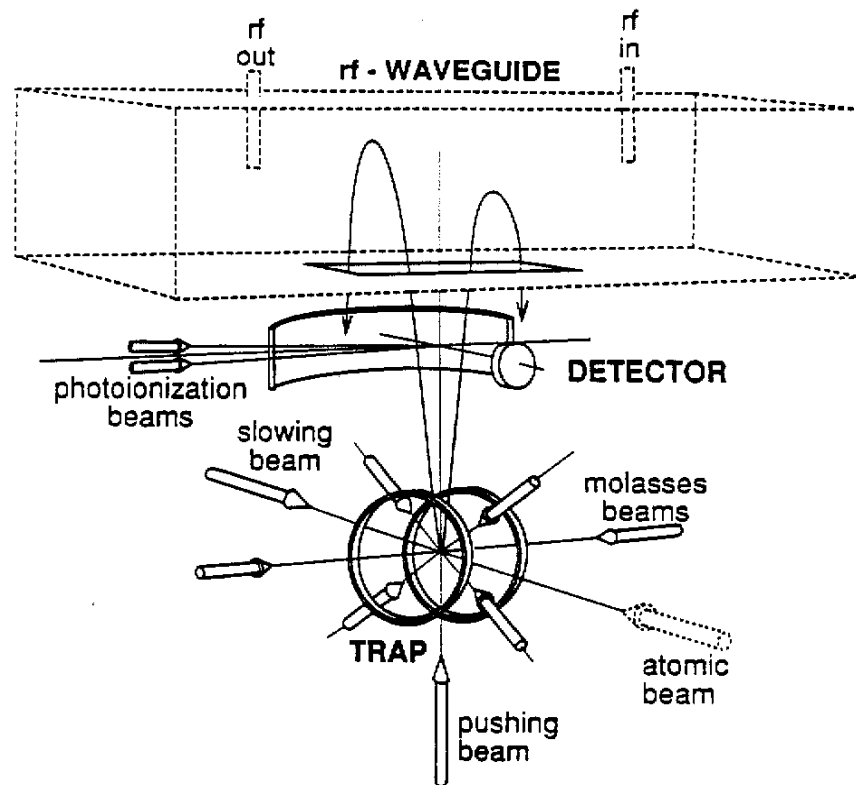
Fig. 3.1: Schematic of the first demonstration of an atomic fountain. Atoms were launched with a resonant light pulse. Near the apex of their trajectories, they entered a rf-waveguide, which was used to drive the groundstate hyperfine transition (see. Fig. 1.1).

preferred method of creating a molasses with polarization gradients which moved vertically with respect to the lab frame. The problem with the pushing launch method is that the velocity spread of the atoms increases from the initial polarization gradient temperature to a value more characteristic of Doppler cooled atoms. The extra heating from this method comes from the diffusion of momentum associated with the scattering force as discussed in section 2.2 On the other hand, atoms can be launched without

additional heating with a "moving molasses" technique. The moving molasses light field is created by red shifting the frequency of the upper molasses beams and blue shifting the frequency of the lower molasses beams. The equilibrium velocity of the atoms is the velocity that Doppler shifts all beams to the same frequency. The velocity spread in the moving molasses is again the ~ 30 cm/sec characteristic of polarization gradient molasses. Experimentally this method is more difficult to implement, but leads to a factor of ~ 30 increase in velocity phase space density. After the atoms reached their equilibrium temperature in the moving molasses, the molasses beams were extinguished by blocking them with a mechanical shutter. For many experiments it is desirable to prepare the sample in one hyperfine state. Just prior to closing the shutter, atoms could be optically pumped into the $F = 1$ groundstate by turning off the repumping sideband for the optical molasses.

Atoms were detected by resonant photo-ionization. Atoms were ionized if they were in the detection region when the ionizing laser beams were pulsed on. Ion counts were subsequently registered by a micro-channel plate. In the photo-ionization process, atoms were resonantly excited into the $3P_{3/2}$ state by a ~ 500 nsec pulse of light from the trapping laser before being ionized by a co-propagating 15 nsec pulse of 355 nm laser light. The detection process was made state sensitive by adjusting the frequency of the light from the trapping laser.

3.2 APPARATUS

The basic system can be roughly divided into three categories: vacuum hardware, optics, and electronics.

(1) Vacuum hardware. The atomic source is located off of one arm of the main vacuum can, as shown in Fig. 3.2. The effusive atomic beam is slowed by a counter-propagating beam which entered through a window on the opposite side of the chamber. Atoms entered the main chamber through an ~ 6 mm aperture. In the middle of the chamber, the slowed beam intersected the magneto-optic trap. After being trapped, cooled, and finally launched atoms were detected approximately 25 cm above the trapping point. Typical operating pressures in the main vacuum chamber were 10^{-9}-10^{-10}

Viewport

Molasses
Beam

Mirror

Molasses
Beams

Atomic Beam

Slowing
Beam

Trapping
Coils

Cylindrical
Vacuum
Chamber

3'

Molasses
Beam

Support Legs

Partial view:
Only viewports for
molasses/slowing beams
indicated
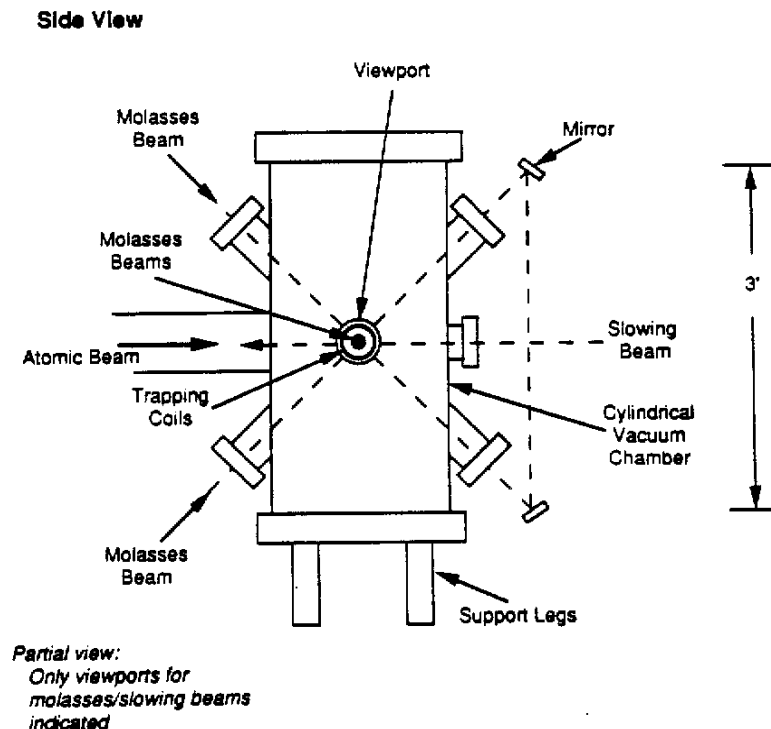
Fig. 3.2: Schematic of the vacuum system for the atomic fountain
apparatus.

torr.

(2) Optics. Fig. 3.3 shows a schematic diagram of the laser/optics system. A
single frequency, actively stabilized commercial dye laser generated the laser cooling
beams. Requisite frequency shifts were produced with a mixture of commercial and
home-made non-linear modulators. The frequency of the laser was further stabilized to
an external reference vapor cell. A frequency tripled Q-switched Nd:Yag laser provided
the pulsed radiation for photo-ionization. The molasses laser beams converged on the
atoms in an X-configuration, as shown in Fig. 3.2. This freed up the vertical axis for

34
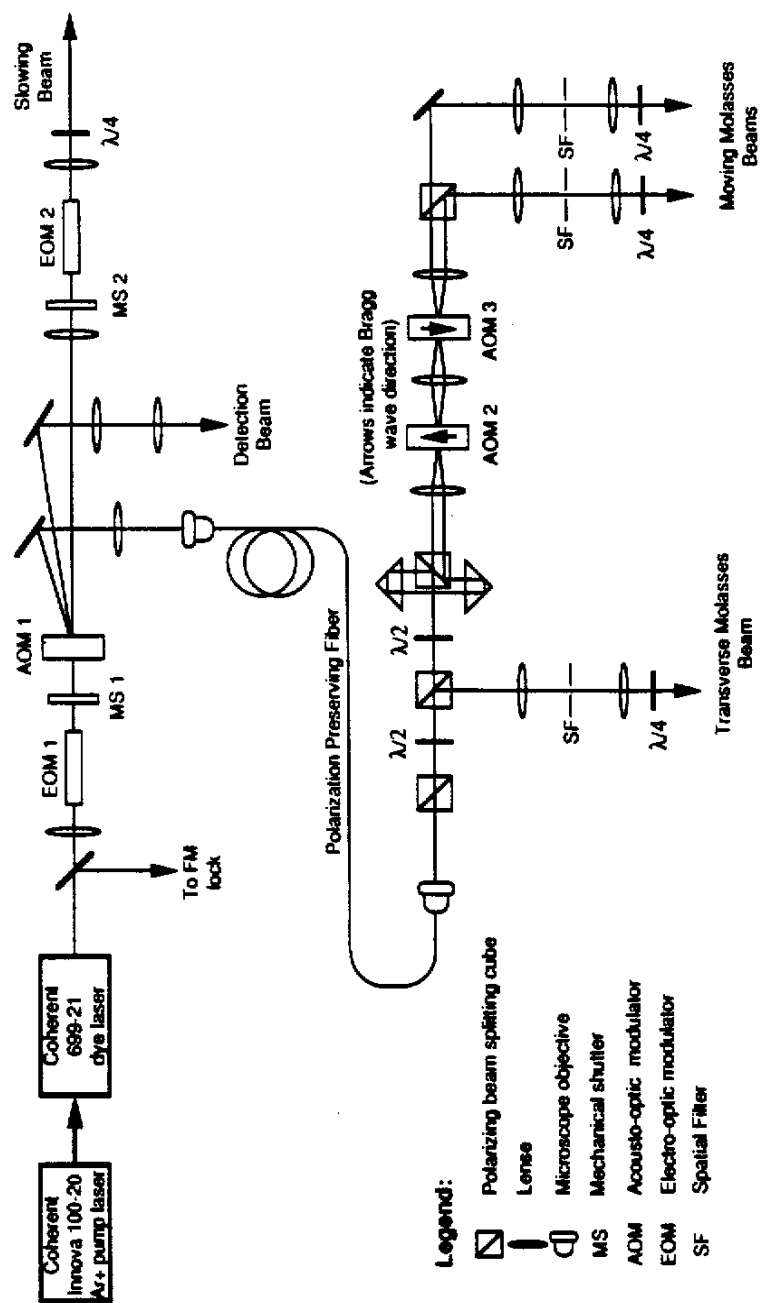
Fig. 3.3: Schematic diagram of the laser/optics system

35

the experiment at hand. The photo-ionization beams defined a detection volume a few cm in front of the micro-channel plate. The orientation of the Nd:Yag beam was fixed horizontally, but the propagation axis of the beam derived from the dye laser could be varied to constrain the detection volume as desired.

(3) Electronics. An armada of pulse generators controlled the timing. Rf synthesizers, VCO's and amplifiers drove the non-linear optical elements. For time/frequency critical components, a Stanford Research Systems FS 700 LORAN-C stabilized oscillator provided a 10 MHz reference timing signal (some of the pulse generators could be slaved to an external reference).

The entire laser/optics system fit on one 4'x12' Newport table (unfloated) and a couple of smaller breadboards firmly bolted onto the main table. The large vacuum chamber was placed off to one side of the table, and rested on the floor. It was not attached to the optical table. Accompanying electronic equipment was stuffed below and above the table. A major problem proved to be supplying enough cold air to the room to adequately cool the electronics. Without air conditioning it was impossible to run (room temperatures exceeded 90°F). Too much air flow caused turbulence which lead to laser beam pointing instabilities (air flow was regulated by variable speed overhead fans). At the compromise air flow rate, the room temperature rose by ~5°F over approximately two hours after all electronic components were turned on. Temperature sensitive alignments were done after thermal quasi-equilibrium had been reached.

3.2.1 *Vacuum system*

The atoms were trapped and launched in an ultra-high vacuum environment. The main vacuum chamber (~ 100 ℓ volume) held a pressure of 10^{-9} torr with a trouble free CTI-8 cryo-pump. The chamber was welded from 304 stainless steel, and Conflat type copper seal flanges were used throughout. Pressure in the main chamber was measured with a nude ion gauge. At 10^{-9} torr the mean free path of background atoms is much larger than the dimensions of the apparatus. A home-built liquid nitrogen cooled copper cryo-shield was mounted just inside the chamber walls. At LN_2 flow rates of $> 10\ell/hr$ the background pressure dropped to 10^{-10} torr. After breaking vacuum the chamber

would pump down to 2×10^8 torr in 8 hours. The number of trapped atoms in the magneto-optic trap improved by roughly an order of magnitude when the background pressure was reduced from 10^8 to 10^{-9} torr. The incremental increase in the number trapped from 10^{-9} to 10^{-10} torr was not nearly as dramatic (less than a factor of 2). The cryo-shield was useful in obtaining low background pressures following a vacuum break. Approximately 2 kW worth of bake-out heaters were glued onto the chamber with RTV. These were used once for their intended purpose during the course of this research. They proved useful, however, for preventing fogging of the optical windows on humid days when the cryo-shield was operative: radiative cooling from the inner shield lowered the temperature of the surrounding chamber which in turn condensed water on the windows. Turning on the heaters (~ 400 Watts) warmed up the can enough suppress this problem. (Warning: driving the heaters with a Variac produces a ~ 5 mG 60 Hz AC magnetic field near the center of the chamber).

The cryo-pump was vibrationally isolated from the main chamber with a home-built suspension system consisting of three small inner-tubes sandwiched between two large aluminum plates and a flexible bellows. One plate was attached to the chamber, the other to the pump, and the bellows connected the pump to the can.

The windows for the viewports which admitted the cw laser beams into the vacuum can were Huntington standard 7056 glass (Kovar seal) viewports. Flatness was remarkably good in the center 3" diameter of the windows (measured interferometrically to be planar to $\lambda/2$ over 1"). The windows were coated by Continental Optics with a hard dielectric double-V at 589 nm (Na) and 671 nm (Li). Uncoated 7056 glass windows were used for the 355 nm light.

The oven for the thermal atomic beam was located in a separate, differentially pumped, chamber. The atomic beam entered the main chamber through an ~ 6 mm square aperture. The aperture could blocked by an electro-mechanical shutter (Uniblitz LS6) mounted inside the vacuum can. A 170 ℓ/sec Balzers turbo pump maintained a base pressure of 5×10^{-9} torr when the oven was off, and a pressure of $\sim 5 \times 10^8$ torr when the oven was on.

3.2.2 Oven

Fig. 3.4 shows a schematic view of the atomic beam oven. A two chamber design was employed. A large reservoir chamber, which could hold an ~ 7 cm^3 charge of sodium, was attached to a smaller nozzle chamber. The temperature of the nozzle chamber and the reservoir chamber could be independently controlled by separate heaters which were brazed onto the 304 stainless chamber bodies. The entire assembly was encased by a three layer radiation shield. The inner two layers were constructed from thin sheets of unpolished stainless steel. The outer shield was water cooled copper. The effusive nozzle consisted of a 1 mm diameter hole approximately 4 mm long. The beam divergence was estimated to be $\sim \pm 15°$, inferred from the shadow of oxidized sodium left on the aperture between chambers. The entire oven structure was connected to an 8" Conflat flange which in turn was mounted on a bellows assembly. This permitted the beam to be steered while the oven was operational.

Standard operating temperatures were 13.0 mV for the nozzle and 12.5 mV for the chamber (measured with Type K thermocouples). Little effort went into optimizing these temperatures: they were chosen to give acceptably high numbers of trapped atoms while at the same time conserving the charge. A charge typically lasted 600-900 hrs of running time.

3.2.3 Magneto-optic trapping coils

The spherical quadrupole magnetic field was generated from two 10 cm diameter current loops separated by ~ 5 cm. Each loop was formed from 9 turns of 1/4" square, fiberglass insulated, tubing. Water flowed through a 1/8" diameter channel in the core of the current carrying copper to dissipate heat generated when the coils were on. At 50 A drive current the field gradient was measured to be ~ 1 G/mm with a Hall effect probe along the symmetry axis of the coils.

The coils were supported by clamps which were weakly thermally linked to the cryo-shield. This proved to be a *serious design flaw*: if there was no cooling water flow and the magnet was off, stagnant water in the coils would freeze when the cryo-shield was cooled. An experiment showed that expansion during the ice block was enough to

Conflat 8" flange

Flexiible bellows

Support
rods
(3 places)

Tilt adjust
(3 places)

Nozzle

Atomic beam

Heater
coils

S.S. radiation
shields

Reservoir

Water cooled
copper shield

Not to scale
Not shown:
Feedthrough for water
thermocouples, and
heater power.

Oven support screw
(6 places)
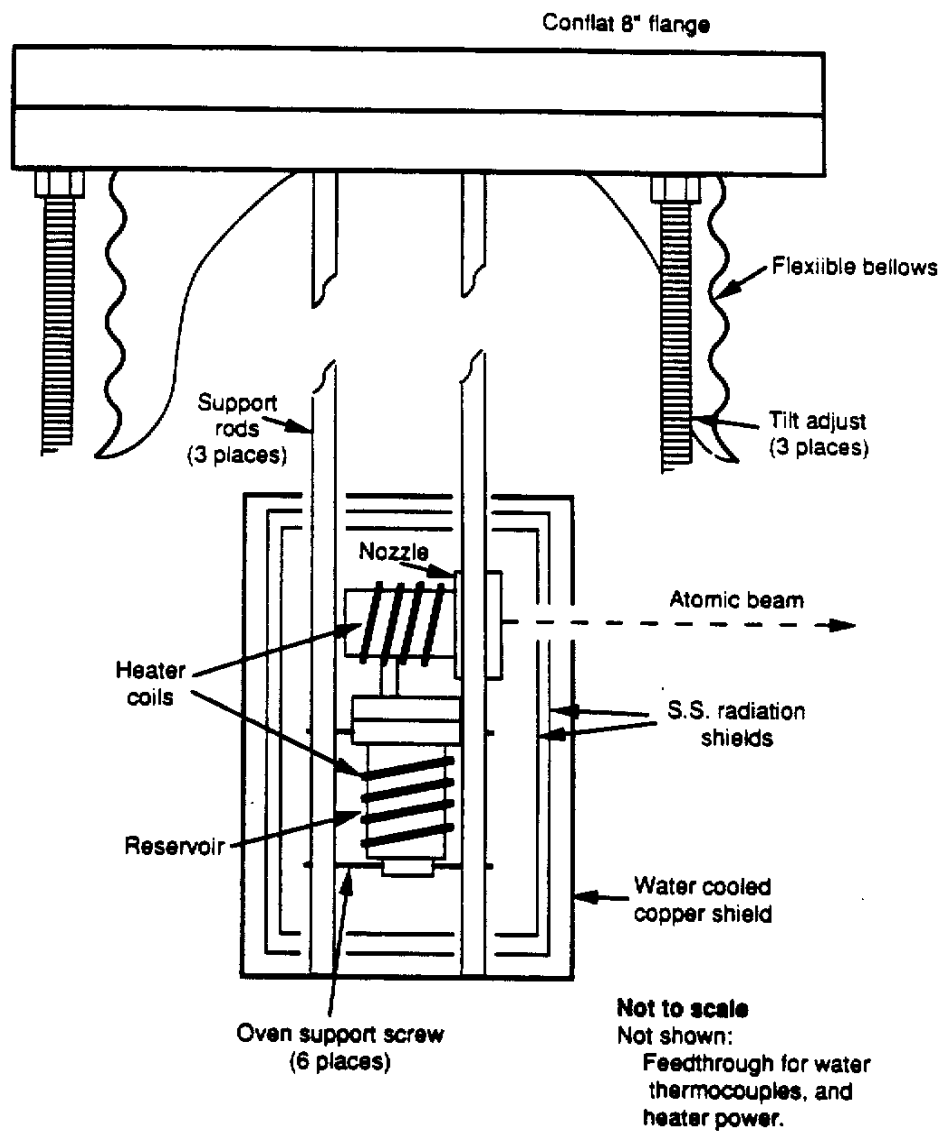
Fig. 3.4: Atomic beam oven

39

rupture the coils. An interlock was installed that prevented the LN$_2$ from being turned on if there was no water flow.

Operation of the atomic fountain required the trapping magnet to be switched off on the time scale of ~ 1 msec with a current extinction of better than 10^3 (residual fields of ~ 10 mGauss are desired). A 100 Amp/ 6 Volt (Kepco ATE 106) remotely programmable power supply was used to drive the magnet. The supply was switched off in voltage control mode. The current switching mode was slower and produced unwanted reverse current flows in its ~ 800 μsec switching time. Reverse currents create an anti-trapping condition for the atoms in the magneto-optic trap in which atoms are pushed away from the field minimum. To insure good switching performance two measures were taken: (1) a water cooled resistor (2 ft. of 1/4" SS tubing) was placed in series with the inductive current loops. This improved the L/R current decay time by a factor of 5 to approximately 150 μsec. (2) Two power MOSFET's in parallel with one another were placed in series with the with the supply. The FET's were pinched off in ~ 100 μsec following the command to short the power supply. This ensured a zero current condition.

Eddy currents induced in the copper cryo-shield ultimately limited switching performance. These currents damped out with a 1/e time of 4 msec when the shield was at room temperature and 9 msec when it was at LN$_2$ temperature (measured with an Applied Physics Systems 520A fluxgate magnetometer). These values agree well with the crude estimate $\tau \sim \mu\sigma L^2$, where σ is the conductivity of the metal, τ is the damping time, and L is the characteristic scale length for the induced field gradients.[75]

3.2.4 Laser/Optics system

A block diagram of the optics system is illustrated in Fig. 3.3. A Coherent 699-21 dye laser supplied 589 nm single mode radiation for four purposes: (1) to frequency lock the laser to a reference vapor cell; (2) to slow atoms in the atomic beam to speeds where they will load into the magneto-optic trap; (3) to trap and cool the atoms; and (4) to detect the atoms.

The Coherent 699-21 was operated with R-6G dye and 6.5 W of pump power

40

from a Coherent Innova 100-20 Ar^+ pump laser. The Ar^+ laser was run multi-line visible with no aperture. A dye concentration of ~ 1 gm R-6G (Exciton chloride) per liter of ethylene glycol was circulated by the Coherent factory supplied module at a pressure of ~ 60 psi and temperature of $\sim 10°C$. The dye was cooled with a Neslab heat exchanger located between the output of the module and the dye laser nozzle. The laser supplied ~ 1.1 Watts of single line light with fresh dye and 6.5 watts pump power. Laser optics were kept clean for long periods of time (the mean time between cavity optics cleaning was ~ 1 month) by mounting a Clean Rooms International filter hood (HEPA-PLEAT II) above the laser. The linewidth of the laser was ~ 2 MHz.

Approximately 5% of the beam was split off for the FM lock just following its output from the laser cavity. The FM lock (see below) servoed the laser frequency to a lock frequency 30-110 MHz (depending on lock parameters) above the $3S_{1/2}$, $F=2 \rightarrow 3P_{3/2}$, $F=3$ transition frequency.

The remaining light was focussed through a home-made 1.71 GHz resonant electro-optic modulator (EOM1 in Fig. 3.3), a Uniblitz mechanical shutter (MS1) and an Isomet 110 MHz acousto-optic modulator (AOM1). The resonant electro-optic modulator (EOM1) imposed the 1.712 GHz "repumping" sideband on the light to keep the atoms from becoming optically pumped into the $F=1$ hyperfine level. The sideband power was 20% of the carrier power with 30 dBm of rf power driving the crystal. The rf signal for the modulator was generated by amplifying the frequency doubled output of a Wavetek 2500A synthesizer. Two fast rf switches were placed in series between the synthesizer and doubler. The combination allowed the modulator to be switched off in ~ 1 μsec with an extinction of 10^{-5}.

The Uniblitz LS2 shutter (MS1) was used to finally extinguish the light following the launch of the atoms. Placement of the shutter in a beam waist meant that in the far field the atoms saw the light turn off uniformly. The shut-off time was ~ 50 μsec with a timing jitter of $\sim \pm 50$ μsec and a trigger delay of ~ 1 msec.

The Isomet acousto-optic modulator (AOM1) was used to divide/multiplex the beam for the slowing, trapping and detection functions. The undiffracted beam became the slowing beam. At 90 MHz drive frequency the first diffracted order was switched

41

into the detection beam line. At 110 MHz drive frequency the light was switched into the molasses beam line.

After AOM1, the slowing beam was then refocussed through a broad-band travelling wave electro-optic modulator[76] (EOM2) and another Uniblitz mechanical shutter (MS2). This modulator produced the frequency chirp necessary to keep the light in resonance with the atom as the atom decelerated. Typically the frequency was chirped from 1 GHz to 100 MHz in 2 msec. A custom made Brimrose VCO drove a 10 W, 1 GHz Amplifier Research broadband amplifier which fed EOM2. The overall modulation efficiency was flat to within ±20% over the range of the sweep. At maximum rf power output, the carrier and first order fm sidebands had approximately equal power. The Uniblitz shutter was used to turn off the slowing beam when the magneto-optic trapping field was turned off. A final lens focussed the ~8 mm $1/e^2$ diameter quasi-Gaussian beam (measured at entrance window of vacuum can) to a point just behind the oven nozzle. The light was circularly polarized with a $\lambda/4$ plate just before it entered the vacuum can to take advantage of the good oscillator strength of the $F=2$, $m_f=2 \rightarrow F=3$, $m_f=3$ transition.

The detection beam (90 MHz first order out of AOM1) was collimated and sent into the vacuum can. For some experiments (eg. surface scattering and demonstration of stimulated Raman transitions) the beam was focussed to an elliptical profile of ~500 μm by ~8 mm in the detection region to give good (1D) spatial resolution. The detection beam was overlapped with the pulsed 355 nm beam using a dichroic plate (actually a 355 nm 0° mirror). The combined beam pair was then steered into the can with aluminum mirrors which were mounted on a motorized translation stage so that the position of the detection region could be scanned systematically. The frequency of the cw detection light was adjusted to be nearly resonant with the $F=2 \rightarrow F=3$ transition by applying the appropriate control signal to the FM lock (see below). The total power available to this beam was ~150 mW.

The molasses beam (110 MHz first order out of the AOM1) was steered into a microscope objective (NA 0.4) which focussed the beam into a ~2 m length of polarization preserving optical fiber (Newport F-SPV). The primary purpose of the fiber

was to isolate the rest of the molasses beam optics from day to day pointing drifts of the dye laser beam. The output of the fiber was collimated and steered through a polarizing beam splitting cube to fix the polarization axis of the light. Care was taken to insure that the fast/slow axis of the fiber was parallel to the incoming polarization of the molasses light in order to minimize thermal/stress induced drifts in the output beam polarization. Fluctuation in the beam intensity after the polarizer due to polarization walking in the fiber was at the 1% level. After the polarizer, the beam was further split into three paths: one path for each frequency needed in the "moving molasses" launch. First, the transverse molasses beam was split off from the beam with another polarizing beam splitting cube. A $\lambda/2$ plate just before this polarizer allowed the intensity of the split off beam to be easily adjusted. The remaining beam was divided into two parallel, slightly displaced beams. Rotation of a second $\lambda/2$ plate again allowed daily tweaks of the relative powers of the final two molasses beams. The combination of the polarizing beam splitting cube and two 180° prisms provided a means of obtaining parallel beams which was insensitive to rotation of each of the three elements in the plane nominally parallel to the optical table. By mounting one of the prisms on a translation stage the distance between the two beams could be precisely controlled. The two beams were next simultaneously focussed into another acousto-optic modulator (AOM2) so that one beam diffracted from one side of the Bragg wave (upshifting its frequency by 110 MHz) and so that the other beam diffracted from the other side of the Bragg wave (downshifting its frequency by 110 MHz). After leaving this first acousto-optic modulator the beams were immediately focussed into a second acousto-optic modulator (AOM3), whose driving frequency was nearly 110 MHz. The direction of propagation of the second Bragg wave, however, was reversed from that of the first wave, so that the frequency shifts in the second modulator opposed those of the first modulator. When the frequency of the second modulator differed from that of the first modulator, the frequency of one beam was on net upshifted by the difference frequency between the two modulators, while the other was downshifted by the difference frequency. Finally, the beams were made parallel and then separated from one another (and undesired diffraction modes from the pair of modulators) with another polarizing beam splitting cube. Slight angular

43

misalignments produced by switching the difference frequency of the AOM pair from zero to the moving molasses frequency were converted to parallel displacements by the collimating lens immediately following AOM3.

Although cumbersome, this method of deriving the moving molasses frequencies had its advantages. First, the beam frequencies were automatically upshifted and downshifted by the same amount. Second, the intensity of all three beams could be controlled by adjusting the diffraction efficiency of AOM1 before the optical fiber. Finally, it was relatively straightforward to shift between the trapping/cooling frequency configuration (all beams of the same frequency) and the launching configuration by simply changing the control voltage of the VCO which drove AOM3.

All three molasses beams were independently telescoped and spatially filtered with pinholes before being sent into the vacuum can. The two vertically oriented beams were aligned to be counter-propagating in the racetrack configuration shown in Fig. 3.2. The beams were also focussed slightly to compensate for power loss between successive passes through the trapping region. The aim was to keep the beam intensities balanced in the trapping region. The $1/e^2$ diameter of each beam was ~ 1.5 cm -- large enough to accommodate ~ 2 msec of cooling time for a moving molasses which drags the atoms through the beams at a rate of ~ 2 m/sec.

3.2.5 *FM Saturated Absorption Lock*

The frequency of the dye laser was stabilized against frequency drifts by locking the laser to the $F=2 \rightarrow F=3$ Na resonance line with a frequency modulation lock scheme.[77] A frequency modulated probe beam (modulation index $\ll 1$) is made to counter-propagate with a saturating pump beam in a vapor cell. The probe beam intensity is measured with a fast photodiode after it transits the cell. When the laser frequency is far from an atomic resonance the beatnote between the first order sidebands of the frequency modulated probe beam and the carrier interfere destructively on the photodiode so that there is only a DC response (the beatnote between the upper sideband and carrier is 180° out of phase with the beatnote between the lower sideband and carrier). As the laser carrier frequency approaches the atomic resonance, the

polarizability of the vapor is no longer effectively independent of frequency, and the phase and/or amplitude balance between beatnotes is destroyed. This leads to a response on the photodiode at the modulation frequency. Finally, when the frequency of the laser is such that the pump and probe beams resonate with the same velocity class of atoms, the probe registers the dramatic change in the polarization of the atoms induced by the pump, and the photodiode has a strong response at the modulation frequency. The frequency width of the pump-probe response can be on the order of the natural linewidth of the resonance. By mixing the photodiode output with power from the reference oscillator used to drive the frequency modulator, well formed dispersive lineshapes are obtainable. By chopping the pump, and detecting the mixer output synchronously with the chop frequency, the broad Doppler broadened probe response can be separated from the sharp pump/probe features.

Light was split off from the main laser beam with a slightly wedged plate as shown in Fig 3.5. One reflected beam became the pump and was focussed through a 16.15 MHz phase modulator. The other beam was double passed through an Isomet 110 MHz AOM. A $\lambda/4$ plate rotated the polarization of the probe beam from vertical to horizontal between the first and second pass through the AOM so that the return beam passed through the polarizing beam splitting cube and into the cell. Both the pump and probe beams were expanded from ~ 1 mm to ~ 8 mm $1/e^2$ diameters before entering the cell to prevent power broadening of the FM lineshapes while maintaining good overall power levels in the beams. The cell temperature was ~ 8.5 mV (type K thermocouple) with the finger 0.5 mV colder. The probe beatnote was detected with a FND-100 photodiode, amplified in a Mini-Circuits 500LN amplifier, and then mixed down to DC. A phase shift between the modulation frequency and mixer reference frequency was introduced with a delay box (1 nsec increments) placed between the mixer and reference oscillator. The pump was chopped at 100 kHz and a fast lock-in (PAR 5101) was used to demodulate the signal. The time constant on the lock-in was 100 μsec.

The phase of the lock-in and of the reference frequency to the mixer were adjusted until a large dispersive feature was found in the demodulated FM signal. The

45

To servo control

FND-100
Photodiode

Na Vapor Cell

110 MHz
Acousto-optic
modulator

16.15 MHz
Electro-optic
modulator

Aperature

$\lambda/4$

Main Beam

Uncoated wedge

Legend:

Polarizing beam splitting cube

Mirror

Lense
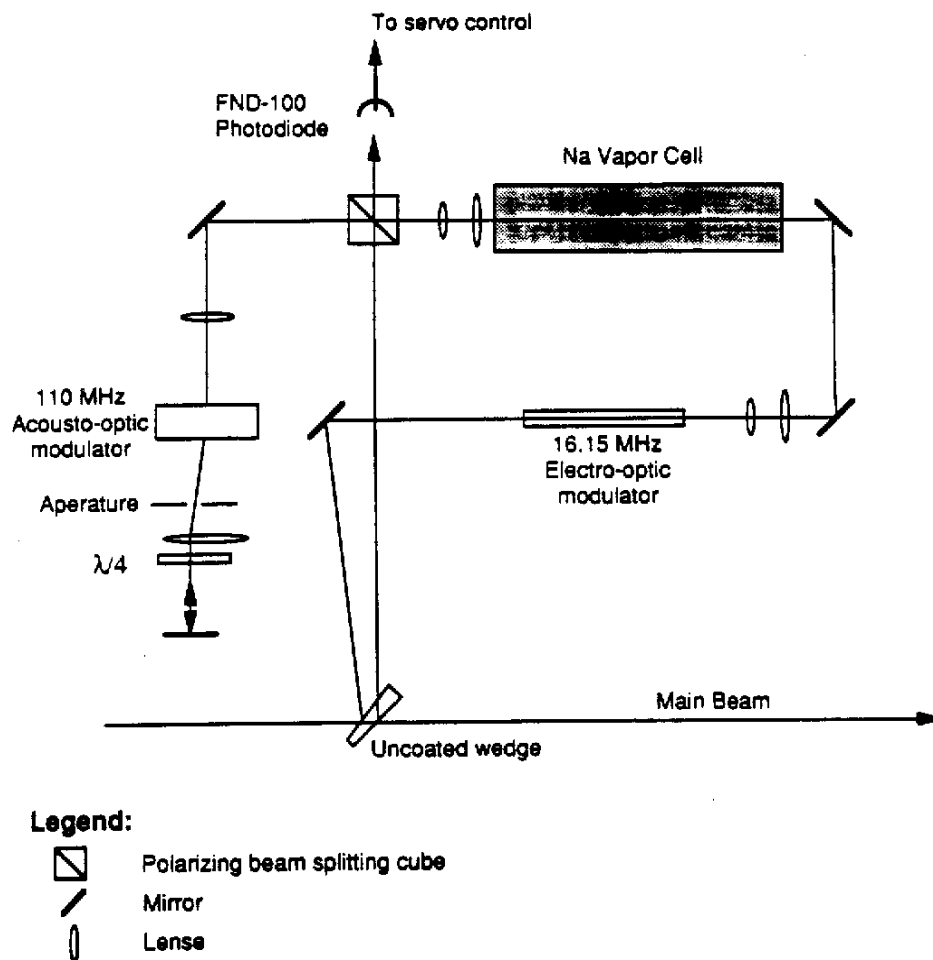
Fig. 3.5: Optics for the FM lock

zero crossing of this feature occurred ~ 29 MHz below the F=2 → F=3 resonance. The 699-21 frequency was then servoed to the zero-crossing of this feature by amplifying the lock-in output with proportional and integral gain (each gain could be optimized) and summing the resulting error signal with the error signal generated by the 699's own reference cavity. The feedback loop was closed by the Coherent laser stabilization drive circuitry, which could directly change the size of the laser cavity at high bandwidth

(through the tweeter) and large dynamic range (with the vertex mounted galvo). The sum point was the non-inverting input for the op-amp which Coherent uses to amplify the reference cavity photo-diode output. This hybrid scheme had a servo bandwidth significantly greater than that of the reference cavity galvo (the traditional sum point for lock error signals). It also retained the good high frequency response of the reference cavity. The double pass through the AOM provided the capability of tuning the frequency of the laser by changing the frequency of the AOM (in this case, the pump/probe response is for a non-zero velocity class). By stepping the control voltage to the VCO which drove the AOM, the frequency of the laser could be switched with a servo-limited slew rate of $\sim$ 10 MHz/200 μsec.

3.2.6 Fluorescence detection

The fluorescence from trapped atoms was imaged onto a 1P21 photomultiplier tube with a lens located inside the vacuum can. This enabled the number of trapped atoms to be monitored, for example, as a function of chirping parameters for the slowing beam. Ballistic measurements of the temperature of the cooled atoms were made by turning off the molasses light and allowing the atoms to drop through a weak probe beam located $\sim$ 2 cm below the trapping point. By imaging the fluorescence from the probe region, the temperature of the atoms could be deduced from the time-of-flight of the atoms to the probe region.[64] This was a useful diagnostic for independently ensuring that the cooling/trapping was functioning properly.

3.2.7 Photo-ionization detection

Resonant photo-ionization was the primary means for detecting atoms launched on fountain trajectories. This scheme offered excellent sensitivity at low count rates ($\sim$ 10% net efficiency, single atom resolution), excellent background suppression (the background count rate was better than 0.1 counts/shot at 1 shot/sec), and a wide spatial aperture (the MCP used had a 25 mm diameter). An energy level diagram illustrating the states and laser frequencies relevant to the photo-ionization process is shown in Fig. 3.6. The detection could be made hyperfine state selective with the appropriate choice

47

IP

355 nm

$3P_{3/2}$

589 nm

F=2

F=1

$3S_{1/2}$
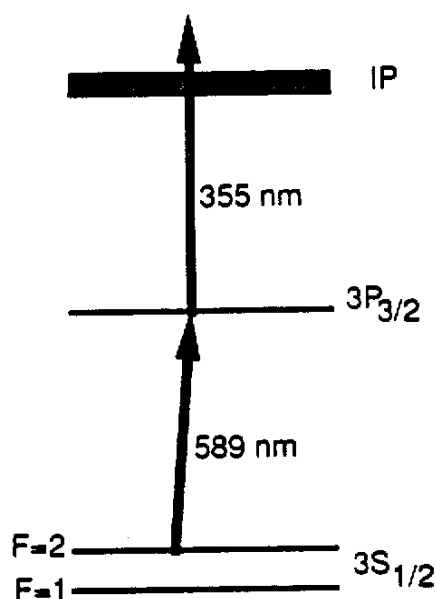
Fig. 3.6: Energy levels relevant to photo-ionization detection.

of cw laser frequency. At high count rates, pulse to pulse intensity fluctuations in the photo-ionization laser intensity lead to a 10% random fluctuation in the detection efficiency. Thus this detection method is well suited to the experiments with low count rates, and in particular those where the atom-shot noise is larger than the fluctuation in detection efficiency (eg. experiments with less than 100 counts/shot).

Fig. 3.7 schematically illustrates the detector assembly. A Galileo *curved* microchannel plate was mounted inside a copper cylinder which shielded the detection region from stray atoms. (Caution: prolonged exposure of these micro-channel plates to air will cause them to crack due to water absorption). The copper cylinder, in turn, was mounted on a base plate with a movable aperture that served to "image" the trapping volume (the aperture could be removed when not needed). A fine 1" diameter wire mesh grid (20 lines per inch) was located ~ 2 mm in front of the collection surface of the MCP and a collector plate ~ 2 mm behind the MCP. A 1" x 1" focussing plate, parallel to

Side View

Copper cylinder
superstructure

Galileo
curved MCP

Gate

Grid

View A

Ground shield

Ceramic
support
posts

UHV Coax

Aquadag

Collector
plate

To
Amplifier

Base plate

View A

Fine mesh

Ceramic
support posts
(4 places)

Ground
shield
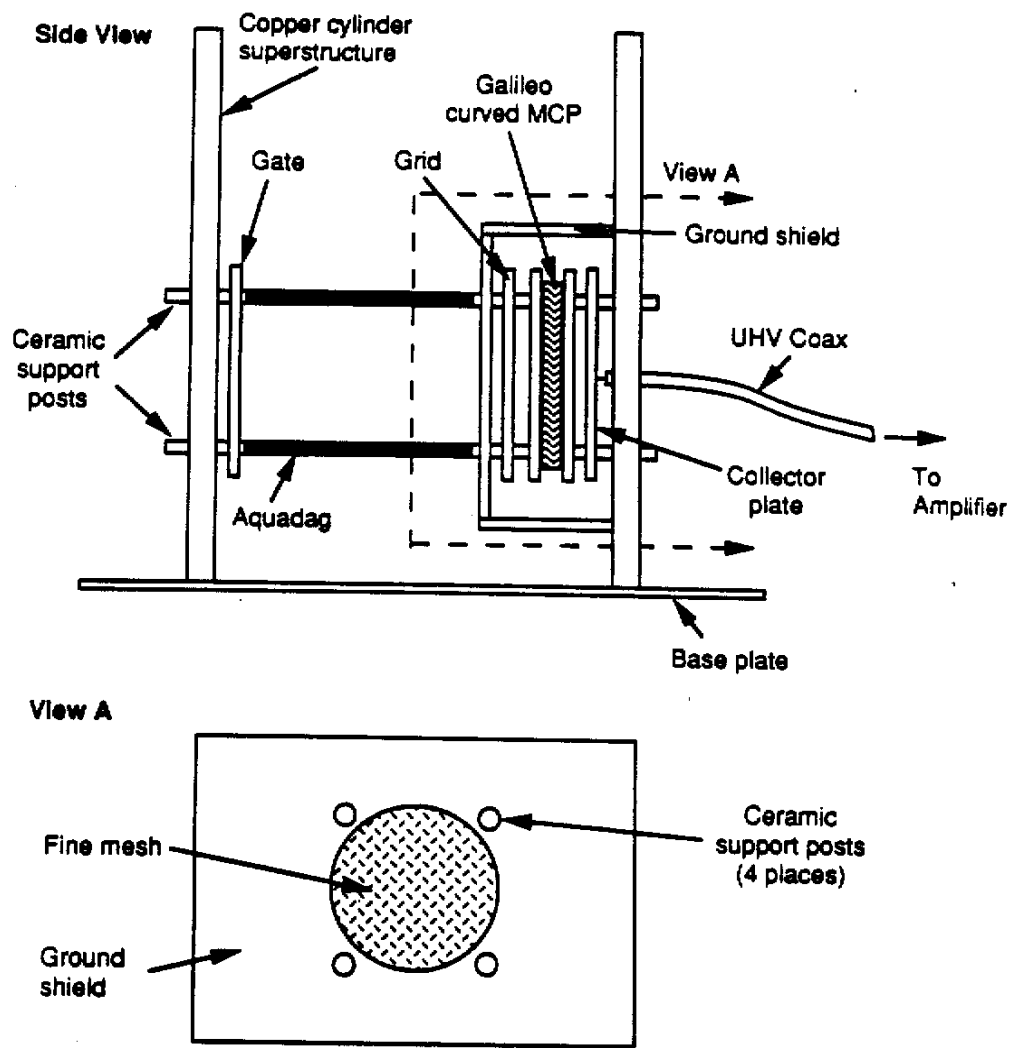
Not to Scale
Not shown:
    Biasing wires

Fig. 3.7: MCP detector assembly

49

the surface of the MCP, was located ~5 cm in front of the grid. The detection volume was located between the grid and focussing plate.

Care was taken to shield atoms from the biasing fields for the MCP when the atoms were in free flight, before being detected. Stray bias fields can deviate atomic trajectories: a field gradient of 1 (kV/cm)/cm produces a force which accelerates a sodium atom at ~0.01 g (the groundstate level shift is ~41 kHz/(kV/cm)^2).[78] This was done by encasing the MCP in a grounded shield, and grounding both the grid and the focussing plate during free flight periods. Approximately 5 msec before the detection photo-ionization light pulses the grid voltage was biased negative and the focussing voltage biased positive to turn on the MCP. The positively biased focussing plate was also meant to collect stray electrons created by the photo-ionization which might otherwise charge up nearby dielectric surfaces. Ceramic mounting rods which supported the MCP, grid, collector, and focussing plate were coated with a thin conducting layer of colloidal graphite (Aquadag) to minimize exposure of non-conducting surfaces.

The front of the MCP was typically biased from -1.0 to -1.3 kV with respect to the back of the MCP. The back of the MCP was held at -200 V with respect to ground. The collector plate was nominally grounded. The grid voltage was typically pulsed to -400 V and the focussing voltage to +400 V (lower voltages could be used to increase the time of flight to the grid and thus provide crude spatial discrimination via the ion's time of flight). Large filter capacitors were placed at the outputs of the high voltage MCP bias supplies which successfully suppressed line frequency voltage ripple that lead to a 60 Hz baseline drift.

The back of the collector plate was attached to a UHV 50Ω transmission line (Ceramaseal) which carried the signal to a 50Ω UHV vacuum feedthrough. An ORTEC H242A fast (20 nsec rise time) charge coupled pre-amplifier, located at the UHV feedthrough, integrated and amplified the current pulse. The pre-amplified output was gated, amplified (with an SRS Gated Integrator) and finally digitized and logged into an IBM PC.

The ionizing laser radiation was supplied by a Q-switched Nd:Yag Quantel model YG 481a laser.[79] The 15 nsec, 1.06 μm fundamental pulse was doubled to 532 nm.

The doubled pulse was summed with the fundamental to produce ∼ 30 mj of uv light (measured with a Scientec 361 power meter). Power levels are given for a flashlamp voltage of 1.5 kV. Flashlamp firing was triggered externally at a 10 Hz repetition rate. The Q-switch was triggered externally at the repetition rate of the experiment (1 Hz or 5 Hz) and appropriately synchronized with a flashlamp pulse. With new flashlamps and a well aligned cavity, timing jitter from the Q-switch firing to the output pulse was measured to be ±3 nsec.

The rf noise generated by the firing of the Q-switch was suppressed by enclosing the cavity Pockels cell in a copper shield (holes were supplied for the light!). This was a particularly troublesome noise source because it occurred in the same time window as the output pulse from the MCP. Further rf pickup on the MCP detector was reduced by properly grounding and shielding the signal cables and amplifiers.

3.2.8 *Timing*

The loading/cooling/launching/detection sequence was controlled by an array of pulse generators. Two SRS GPIB programmable DG535 delay generators controlled all time critical delays. A brief description of the timing sequence follows. A schematic of the timing control system is shown in Fig. 3.8.

At t = 0 the magneto-optic trapping field was turned off. Simultaneously mechanical shutter MS2 (see Fig. 3.3) blocked the slowing beam, the carrier frequency of the laser was detuned an addition 10 MHz from the trapping frequency and the intensity of the molasses light was reduced. After typically 1 msec the molasses beam frequencies were ramped to the moving molasses values by sending the appropriate ramp voltage to the second moving molasses VCO (see section 3.2.4). The ramp time was an adjustable parameter, but was typically set to 500 μsec. Following the frequency ramp, the molasses light was left on for an additional period of time (typically 500 μsec) to allow atoms to equilibrate with the moving field. At this point, atoms could be optically pumped by switching off the repumping sideband, which had the effect of piling all but 0.3% of the atoms into the F = 1 hyperfine level. Finally, the molasses mechanical shutter was closed, leaving the cold atoms in darkness. A few msec later the molasses AOM

51
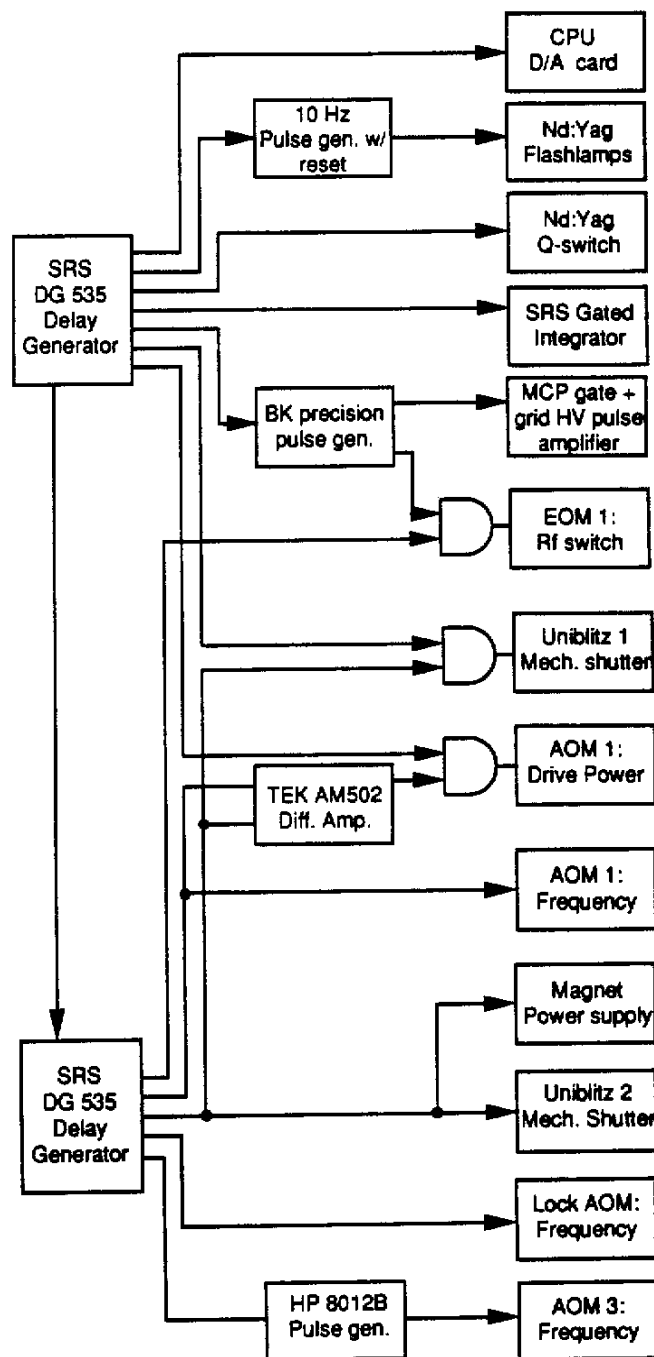
Fig. 3.8: Schematic diagram of timing/control system

(AOM1) driving frequency was switched to the detection frequency and its drive power was turned off. The repumping sideband was turned on to prevent thermal oscillations in the EO crystal (EOM1) due to the applied rf power. Following a preset free-flight time the ionizing lasers were pulsed on. 5 msec before the Q-switch fired the gate on the MCP was opened and, if desired, the rf repumping sideband was switched off. 200 μsec before the Q-switch fired the molasses mechanical shutter opened. Synchronously with the firing of the Q-switch, the molasses (now detection) AOM was switched on for 500 nsec. The uv pulse typically came 300 nsec after the cw detection beam was flashed on. 4 msec after the detection pulse the grid was turned off and the rf sideband turned back on. 1 msec after the detection pulse the frequency of the molasses AOM was switched to 110 MHz and the molasses light was turned on. Simultaneously the slowing beam Uniblitz shutter was reopened and the trapping field was turned on. This point also triggered the data acquisition/ GPIB control software to digitize the output of the SRS gated integrator and change any relevant delay times (eg. the time delay between launch and detection). The trap was allowed to load until the next launch cycle was initiated. The typical repetition rates were 1 Hz or 5 Hz.

3.3 RESULTS

Fig. 3.9 shows a plot of number of atoms detected vs. time delay from launch. For this scan the atoms were launched with a velocity of 2.6 m/sec without being optically pumped into the F=1 state. The gain on the micro-channel plate was increased by a factor of thirty for delay times greater than 200 msec. The detection region was located approximately 25 cm above the trapping region. At this height, the atoms passed through the detection region twice -- once on their way up (peak at 120 msec) and again after they turned around and were falling back down towards the trapping region (peak at 400 msec).

Typical trapping parameters were as follows. The trapping beams were tuned $\sim 1.5\Gamma$ below the $F=2 \rightarrow F=3$ resonance. The rf repumping sideband had 20% of the power in the carrier. The trapping field gradient was ~ 8 G/cm along the symmetry axis of the field coils. The molasses beams had an intensity of 6 mW/cm^2. The laser
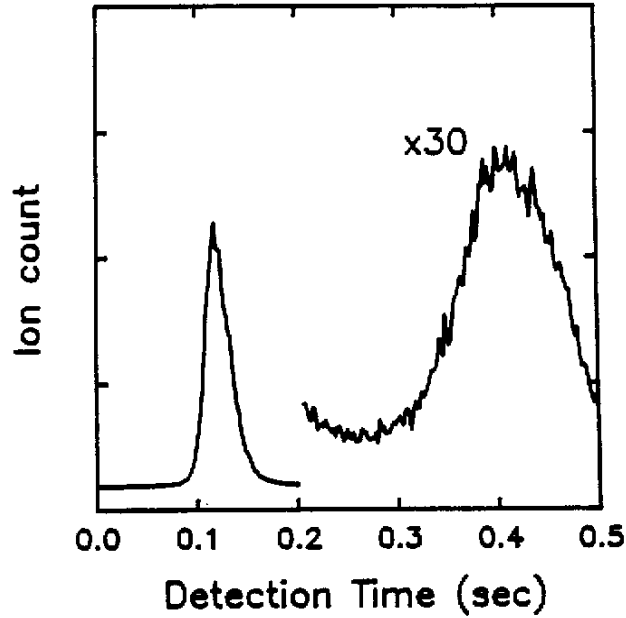
Fig. 3.9: Number of atoms vs. detection time for a moving molasses launch

detuning was increased to -2.5Γ when the trapping coils were switched off (t = 0 msec). At t = 1 msec the moving molasses frequency difference (see above) was ramped from 0 to 2.9 MHz in t_{ramp} ≈ 500 μsec. At t ≈ 2 msec the molasses Uniblitz (MS1) closed.

3.3.1 *General observations*

For the ~1 msec that the light fields are in the moving molasses configuration the ball of trapped atoms travels ~2.6 mm, so that they still sample the center region of the ~1.5 cm diameter molasses beams. The operation of the launch was largely insensitive to the ramp rate for the moving molasses beams (from 1 μsec < t_{ramp} < 2 msec), even when a long (~10 msec) delay until the ramp was used to allow residual magnetic fields to damp away (these fields might impair performance of the polarization gradient molasses). This is indirect evidence that the Doppler scattering force is capable

54

of accelerating the atoms to the moving frame. Even at the low saturation values used here, the Doppler equilibrium time is ~50 μsec (ie. the amount of time required to scatter the number of photons needed to accelerate the atom to 2.6 m/sec). This is significantly less than the time available to cool the atoms. Since the molasses beams move slightly when switched between the lab frame and moving frame frequencies, final alignments (for example spatial filter optimization and beam intensity balance) were done at the moving molasses frequency.

Treating the ensemble of launched atoms as a ballistically expanding ball one expects the number of atoms in the detection volume to scale as t^3 in the limit where the radius of the ball at the time of detection is much larger than the initial source size. The data of Fig. 3.9 is in good agreement with this scaling.

3.3.2 *Comparison with scattering force launch*

Fig. 3.10 shows a time of flight scan with the original launch method (the optics configuration for this method differed from that described in section 3.2). Note that two peaks are not resolvable in the time of flight scan. This is a direct result of the heating during the resonant pushing pulse. We were able to verify that the atoms were following ballistic trajectories by blasting a notch out of the distribution on the atoms' first pass through the detection region and subsequently observing the change in the number of atoms detected on the atoms' second pass through the detection region. Changing to the moving molasses launch scheme afforded a factor of ~30 in count rate.

3.3.3 *Moving molasses failures*

In our first attempt to implement the moving molasses launch we hoped to economize on acousto-optic modulators by just shifting the upper two beams down in frequency, but leaving the lower beam pair and horizontal beam at the same frequency. This might have worked if only Doppler cooling processes were operative. With polarization gradients, however, the atom is sensitive to the absolute frequency of all three beam pairs. In this configuration, there was no frame where all frequencies could be balanced. What we observed was a two peaked velocity distribution. One peak,
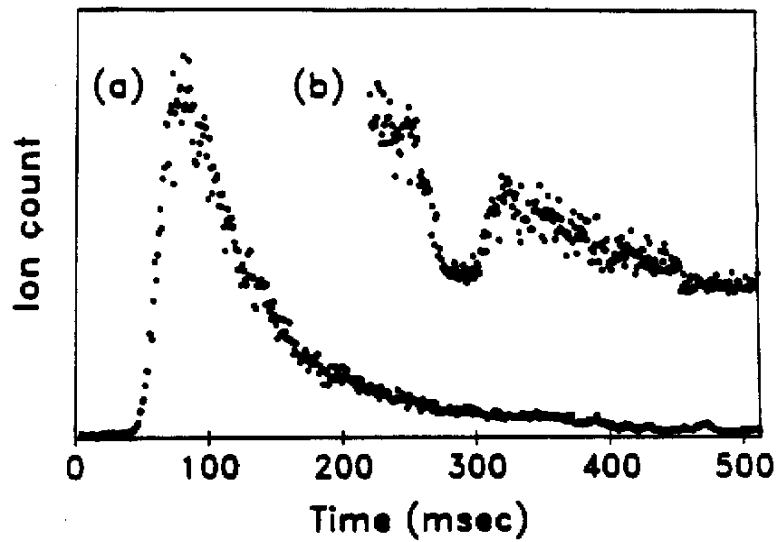
Fig. 3.10: Number of atoms vs. detection time for a resonant light pulse launch.

which was attributed to Doppler scattering forces, had a temperature characteristic of Doppler cooled atoms and displayed the correct dependence of the mean launch velocity on the molasses beam frequency shift. The other peak was narrower, and thus attributed to polarization gradient mechanisms, and had a launch velocity-frequency shift dependence which was half of what was expected. Suffice to say that these problems went away when the lower beams were blue-shifted and the upper beams red-shifted as explained above.

SECTION 4

VELOCITY SENSITIVE STIMULATED RAMAN TRANSITIONS

For many cold-atom experiments, the velocity spreads attainable with polarization gradient cooled atoms are not narrow enough. For example, in studies such as atom-surface collisions, ensembles of atoms with velocity spreads of less than 1 cm/sec are needed to observe quantum reflection from attractive potentials. The approach used in our 1989 surface scattering experiments[43] was to velocity select atoms launched on fountain trajectories with transverse collimation slits. With this technique, we prepared ensembles that had 1-D velocity spreads of less than 1 cm/sec.

Velocity selection with Doppler shifts is a superior velocity preparation technique. The basic idea is to use an atom's internal state as a label for its velocity. Consider, for simplicity, an ensemble of two-level atoms in a travelling wave driving field. If the atoms are prepared initially in one of the two levels and subsequently subjected to a Doppler sensitive excitation to the other level, only those atoms having the appropriate Doppler shift, hence velocity, will be resonantly excited. The excited atoms may then be separated from the initial ensemble, if necessary, by some state dependent interaction. Unlike velocity selection with slits, this type of velocity selection does *not* depend on the initial spatial location and spread of the atoms and is free from wavepacket diffraction effects[80] which might be present with narrow slits. Furthermore, it is intrinsically accurate: distance and time are automatically referenced to the wavelength of the driving field and its frequency. Finally, it is extremely flexible: the center velocity of the distribution is changed by changing the frequency of the driving radiation. For transit-time limited resonances, the velocity spread selected can be controlled by changing the interaction time of the atom with the radiation.

Stimulated Raman transitions between hyperfine groundstate levels are ideally suited to implementation of this type of scheme. A three-level atom, as illustrated in Fig. 4.1, is initially prepared in hyperfine state $|1\rangle$, for example. Two counter-
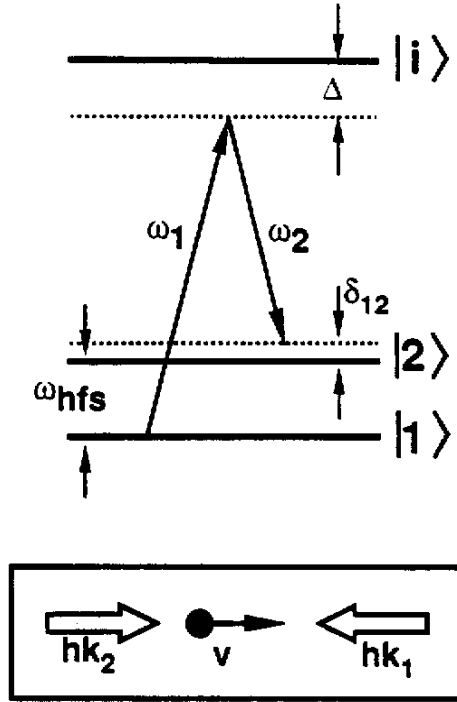
Fig. 4.1: Energy level diagram for stimulated Raman transitions. Inset shows geometry for velocity sensitive transitions.

propagating beams of frequency ν_1 and ν_2 induce stimulated Raman transitions to level $|2\rangle$ if $\nu_1 - \nu_2 + \Delta\nu_{Dopp} \sim \nu_{hfs}$. When the beams counter-propagate, $\Delta\nu_{Dopp} = (v/c)(\nu_1 + \nu_2)$, and the transition has a Doppler sensitivity which is twice that of an optical transition. For sodium, the two-photon Raman transition has a Doppler sensitivity of 33 kHz/(cm/sec) when the Raman beams are nearly resonant with the 589 nm $3P_{3/2}$ transition. The velocity spread, on the other hand, is determined by the time the atom is irradiated by the light. With laser cooled atoms in an atomic fountain this can be in principle on the order of a second. With a more practical measurement time of 10 msec the selected velocity spread is 30 μm/sec for sodium. Ultra-stable lasers are not needed to successfully implement narrow velocity selections: it is only necessary that the difference frequency $\nu_1 - \nu_2$ be phase coherent with the rf transition. Thus, if the frequency ν_2 is generated from ν_1 by an electro-optic modulator or by a phase-lock

technique, the frequency jitter of the laser is canceled out.

The high Doppler sensitivity of stimulated Raman transitions is coupled to a large velocity recoil kick. This is simply a consequence of momentum conservation. An atom initially in state $|1\rangle$ and with momentum p *absorbs* of photon of momentum $\hbar k_1$ and subsequently *emits* a photon of momentum $\hbar k_2$ in the opposite direction, leaving the atom in state $|2\rangle$ with momentum $p+\hbar k_1-\hbar k_2$. For sodium, the stimulated Raman transition recoil momentum translates into a velocity kick of ~ 6 cm/sec. In section 5, we describe an experiment where the large recoil kicks have been used to create an atomic interferometer.

The aim of this section is to lay the groundwork for the interferometer experiment as well as to discuss other applications of velocity sensitive stimulated Raman transitions. Section 4.1 presents the general theory of stimulated Raman transitions. There are three essential results of this section: (1) in certain regimes the three-level system can be viewed as a two-level system coupled with an effective Rabi frequency given by the two-photon transition rate; (2) the internal state of the atom is correlated with its momentum; and (3) the two-photon Raman excitation can be modelled by a travelling wave excitation of frequency $\nu_1-\nu_2 \sim \nu_{rf}$ and propagation vector $k_1-k_2 \sim 2k$. Section 4.2 offers a general overview of the experiment to demonstrate velocity sensitive stimulated Raman transitions. Section 4.3 contains a detailed discussion of the apparatus and experimental method. Finally, experimental results are presented and discussed in section 4.4.

4.1 THEORY OF STIMULATED RAMAN TRANSITIONS[81]

The key assumption in the treatment which follows is that the detuning of the frequencies ν_1 and ν_2 from the optical resonance is large enough that spontaneous emission from the intermediate level $|i\rangle$ can be neglected. This greatly simplifies the theory in that a density matrix approach need not be introduced. When the detuning from the intermediate level is large, the intermediate level can be adiabatically eliminated from the interaction picture Schrödinger equations. The first part of this section discusses the simplest case of a three-level atom in a Raman field of counter-propagating waves. The later parts of this section deal with field configurations realized in our

experiment as well as generalization of the theory to multi-level atoms.

The Hamiltonian for the three-level system is

$$\hat{H} = \frac{\hat{p}^2}{2m} + \hbar\omega_1^A |1\rangle\langle 1| + \hbar\omega_2^A |2\rangle\langle 2| + \hbar\omega_i^A |i\rangle\langle i| + \hat{V},$$ (4.1)

where $\hat{V}$ describes the atom-field interaction, and $\hbar\omega_\alpha^A$ is the internal energy of state $|\alpha\rangle$. In the electric dipole approximation, the coupling of the atom to the Raman light field is

$$\hat{V} = -e\mathbf{r}\cdot\mathbf{E} ,$$

$$\mathbf{E} = E_1\cos(k_1x - \omega_1 t + \Phi_1) + E_2\cos(k_2x - \omega_2 t + \Phi_2).$$ (4.2)

The frequencies $\omega_1, \omega_2 \sim \omega_i^A$ while the difference $\omega_1 - \omega_2 \sim \omega_1^A - \omega_2^A \equiv \omega_{hfs}$ (see Fig. 4.1). For counter-propagating beams $k_1 \approx -k_2$. We have explicitly neglected spontaneous emission from the off-resonant excitation of the optical transition.

Using free-space momentum eigenstates to characterize the center-of-mass motion of the atom, we look for solutions to the Schrödinger equation of the form

$$|\psi\rangle = \int dp \sum_\alpha a_{\alpha,p}(t) e^{-i(\omega_\alpha^A + \frac{p^2}{2m})t} |\alpha,p\rangle .$$ (4.3)

were $|\alpha,p\rangle$ corresponds to an atom in internal state $|\alpha\rangle$ and in momentum eigenstate $\psi_p(x) \sim e^{ipx/\hbar}$. For a given momentum, the Schrödinger equation reduces to

$$\dot{a}_{1,p} = \frac{i}{2}e^{i\Delta_1 t}\Omega_{1i}^* a_{i,p+\hbar k_1} ,$$

$$\dot{a}_{i,p+\hbar k_1} = \frac{i}{2}\left[\Omega_{1i}e^{-i\Delta_1 t}a_{1,p} + \Omega_{i2}e^{-i\Delta_1 t}a_{2,p+\hbar k_1 - \hbar k_2}\right] ,$$ (4.4)

$$\dot{a}_{2,p+\hbar k_1 - \hbar k_2} = \frac{i}{2}e^{i\Delta_1 t}\Omega_{1i}^* a_{i,p+\hbar k_1} ,$$

where

$$\Omega_{ji} = \frac{e}{\hbar} \langle i | r \cdot E_j | j \rangle e^{i\phi_j} ,$$

$$\Delta_j = (\omega_j^A + \omega_j - \omega_i^A) + \frac{p_j^2}{2m} - \frac{p_i^2}{2m} . \tag{4.5}$$

In the above equations, the index $j = 1,2$ while the index i refers to the intermediate state. The momentum associated with state $|1\rangle$ is $p_1 = p$, with state $|2\rangle$ is $p_2 = p + \hbar k_1 - \hbar k_2$, and with state $|i\rangle$ is $p_i = p + \hbar k_1$. For simplicity we have assumed that the electric fields E_j couple only to the $|j\rangle \rightarrow |i\rangle$ transitions. This is a good approximation when ω_{hfs} is larger than the detuning Δ from the optical resonance. The rotating wave approximation has been used to obtain the above coupled equations.

Adiabatic elimination of level $|i\rangle$ results in the familiar equations for a two-level atom in an external driving field:

$$\dot{a}_{1,p} \approx -\frac{i}{2} \Omega_1^{AC} a_{1,p} - \frac{i}{2} e^{i\delta_{12} t} \Omega_{eff} a_{2,p + \hbar k_1 - \hbar k_2} ,$$

$$\dot{a}_{2,p + \hbar k_1 - \hbar k_2} \approx -\frac{i}{2} \Omega_2^{AC} a_{2,p + \hbar k_1 - \hbar k_2} - \frac{i}{2} e^{-i\delta_{12} t} \Omega_{eff}^* a_{1,p} , \tag{4.6}$$

where

$$\Omega_{eff} = \frac{\Omega_{1i}^* \Omega_{i2}}{2\Delta} ,$$

$$\Omega_j^{AC} = \frac{|\Omega_{ji}|^2}{2\Delta} , \tag{4.7}$$

$$\delta_{12} = (\omega_1 - \omega_2) - \left[\omega_{hfs} + v_x (k_1 - k_2) + \hbar \frac{(k_1 - k_2)^2}{2m} \right] .$$

Here v_x is the projection of the atom's velocity along the laser beams.

Momentum recoil explicitly shows up in the coefficients of Eqs. (4.6), where there is a one-to-one correlation between the atom's internal state and its momentum. The first terms on the right of Eqs. (4.6) lead to AC Stark shifts of levels $|1\rangle$ and $|2\rangle$. The second terms lead to Rabi flopping between the two levels. Note that the effective Rabi frequency Ω_{eff} depends on the initial phase of the light fields. This dependence

eventually leads to the atom's sensitivity to inertial forces during a $\pi/2$-π-$\pi/2$ interferometer pulse sequence.

The effective detuning δ_{12} from the Raman resonance contains three terms: AC Stark shifts, Doppler shifts, and the recoil shift. The AC Stark shifts arise from the weak coupling of levels $|1\rangle$ and $|2\rangle$ to level $|i\rangle$. They are typically on the order of the effective Rabi frequency Ω_{eff}. The Doppler shifts arise from the atom's motion along the laser beams. In the atom's frame of reference, the frequency of each light beam is Doppler shifted by an amount $k_i v_x$. The Raman resonance, therefore, shifts by $(k_1-k_2)v_x$ $\sim 2kv_x$ when the beams are counter-propagating and of nearly the same frequency. For sodium, where the lasers are resonant with the $3P_{3/2}$ transition, this amounts to 33 kHz for an atom with a velocity of 1 cm/sec along the beams. Although the levels $|1\rangle$ and $|2\rangle$ have been described as groundstate hyperfine levels, the above considerations apply equally well to transitions between magnetic sub-levels within a given hyperfine level (eg. $F,m_f=-1 \rightarrow F,m_f=+1$).

4.1.1 *Raman transitions in multi-level atoms*

The hyperfine structure of the intermediate level, although not explicitly considered above, needs to be incorporated into the theory in order to calculate effective Rabi frequencies for real atoms. The hyperfine structure of level $|i\rangle$ is included by replacing the single state $|i\rangle$ with a multiplet of levels. Again, by adiabatically eliminating these levels, equations of the form of Eqs. (4.4) reduce to the form of Eqs. (4.6). This calculation is detailed in Appendix B. The effective Rabi frequency is now given by a sum over intermediate levels:

$$\Omega_{eff} = \sum_i \frac{\Omega_{1i}^* \Omega_{i2}}{2\Delta_i} ,$$

$$(4.8)$$

where the index i ranges over all intermediate states.

4.1.2 *Raman transitions using phase-modulated lasers*

It was assumed above that only two frequency components were present in the

driving light field. In our experiment, an electro-optic phase-modulator generated the frequency offset for the Raman transitions. Thus, in practice, the light field contained several frequency components. This situation is readily incorporated into the above theoretical framework by explicitly including these fields in the coupling potential $\hat{V}$.

In the experiment described below one of the two counter-propagating beams passed through a phase-modulator and the other through an acousto-optic frequency shifter. In this case, the Raman frequency was determined by the difference frequency between one of the frequency sidebands of the phase-modulated beam and the frequency shifted counter-propagating beam. The other, non-Raman resonant, frequency components affected the atom only by contributing additional AC Stark shift terms to the resonance condition.

For the interferometer experiment described in section 5, the Raman transition is driven by phase-modulating both Raman beams. The second, counter-propagating beam, was generated by simply retro-reflecting the first beam on a stationary mirror. The Raman frequency was then determined by the modulation frequency alone. Analysis of this geometry is complicated by the interference between several pairs of Raman resonant sidebands, as well as potentially troublesome contributions from Doppler insensitive Raman processes and from standing wave diffraction. This analysis is presented in Appendix B. In the following paragraphs we summarize the essential results.

Since the frequencies ω_1 and ω_2 come from both directions, there are two Doppler sensitive resonances, one at $+v_{res}$ and the other at $-v_{res}$, where v_{res} is the velocity along the beam for which an atom is resonant with the Raman field. In order to maintain a unique correlation between internal state and momentum, the Doppler shift $2kv_{res}$ must be greater than the Rabi frequency, so that only one spatial combination of ω_1 and ω_2 drives the atom. In this limit, Doppler insensitive Raman processes and standing wave diffraction from same frequency beams become unimportant. Standing wave diffraction results from two-photon transitions which involve counter-propagating beams of the same frequency and polarization. Doppler insensitive Raman terms are out of resonance when the sideband frequency is tuned to one of the Doppler sensitive resonances. In the interferometer experiment, the Doppler shifts $2kv_{res}$ were always at least 10 times the

effective Rabi frequency.

In the weak phase-modulation limit the Raman field has three significant frequency components: a carrier and two sidebands. Thus the total electric field consists of three standing waves of frequency $\omega-\omega_{rf}$, ω, and $\omega+\omega_{rf}$ respectively. The Raman transition is now driven by two possible frequency combinations ω and $\omega-\omega_{rf}$, and ω and $\omega+\omega_{rf}$, and the two Raman amplitudes will interfere. Using this electric field in Eqs. (4.2) we again reduce Eqs. (4.4) to the form of Eqs. (4.6). In so doing we assumed the processes described in the previous paragraph to be Doppler shifted out of resonance. With the approximation that the atomic wavepacket is well localized on the scale length $k_{rf}=\omega_{rf}/c$, the effective Rabi frequency is given by

$$\Omega_{eff}(\ell) = \frac{\Omega_+^* \Omega_c}{2\Delta_+} e^{ik_{rf}\ell} + \frac{\Omega_c^* \Omega_-}{2\Delta_c} e^{-ik_{rf}\ell} , \tag{4.9}$$

where ℓ is the distance of the wavepacket from the retro-reflecting mirror; $\Omega_-, \Omega_c,$ and Ω_+ are the one-photon Rabi frequencies for the lower sideband, carrier and upper sideband respectively; and Δ_+ and Δ_c the detuning from the $|1\rangle \rightarrow |i\rangle$ optical transition for the upper-sideband and carrier. Note that Ω_{eff} has a slowly varying spatial dependence on the scale length of k_{rf} (λ_{rf} for sodium is ~ 18 cm).

4.1.3 Stimulated Raman transitions and the uncertainty principle

The Heisenberg uncertainty principle requires

$$\Delta x_{Heis} \geq \frac{\hbar}{m\Delta v} , \tag{4.10}$$

where Δv is the selected velocity width at the end of the velocity selecting light pulse of duration $\Delta t \sim \pi/(k\Delta v)$. On the other hand, atoms are initially localized to $\Delta x_0 \sim \lambda/20$ in the optical molasses,[82] and the ballistic spreading of a wavepacket of velocity spread Δv in time Δt is[83]

$$\Delta x_{bal} \approx \sqrt{(\Delta v \Delta t)^2 + (\Delta x_0)^2} \approx \frac{\lambda}{2} \quad , \tag{4.11}$$

which can be much *less* than Δx_{Heis} for narrow velocity slices. So how is the uncertainty principle satisfied? The answer: the photon recoil during the Raman transition leads to an additional wave-packet spreading. During the course of the Raman transition, population is fed continuously from one hyperfine level to another. Since the change in state is accompanied by a velocity recoil of $\sim 2\hbar k/m$, the population making the transition just after the Raman light is turned on drifts a distance

$$\Delta x_{Ram} \approx \left[\frac{2\hbar k}{m}\right] \Delta t \approx \frac{\hbar}{m \Delta v} \quad , \tag{4.12}$$

during the interaction time Δt with respect to the population making the transition just before the Raman light is turned off. A more quantitative analysis confirms this heuristic view.[84] Comparison of Eq (4.12) with Eq. (4.10) shows that velocity sensitive Raman transitions can be viewed as a means of preparing *uncertainty principle limited* wavepackets.

4.2 OVERVIEW OF EXPERIMENTAL DEMONSTRATION

The goal of the demonstration experiment was to prepare an ensemble of atoms with a narrow velocity spread using velocity sensitive stimulated Raman transitions and then to subsequently measure the velocity spread by ballistic methods.

The experiment was carried out in the atomic fountain apparatus described in section 3. Initially trapped and cooled atoms were launched through a pair of counter-propagating beams tuned to the hyperfine Raman resonance (see Fig. 4.2). The atoms were optically pumped into the F=1 level after being launched and the atoms in resonance with the Raman beams were promoted to the F=2 level. The transverse velocity spread was then measured by using the velocity selected atoms to illuminate a narrow (1.6 mm) slit whose edges were parallel to the velocity selection axis. The slit was located ~ 20 cm above the trap center. The image of the slit on the spatial atomic
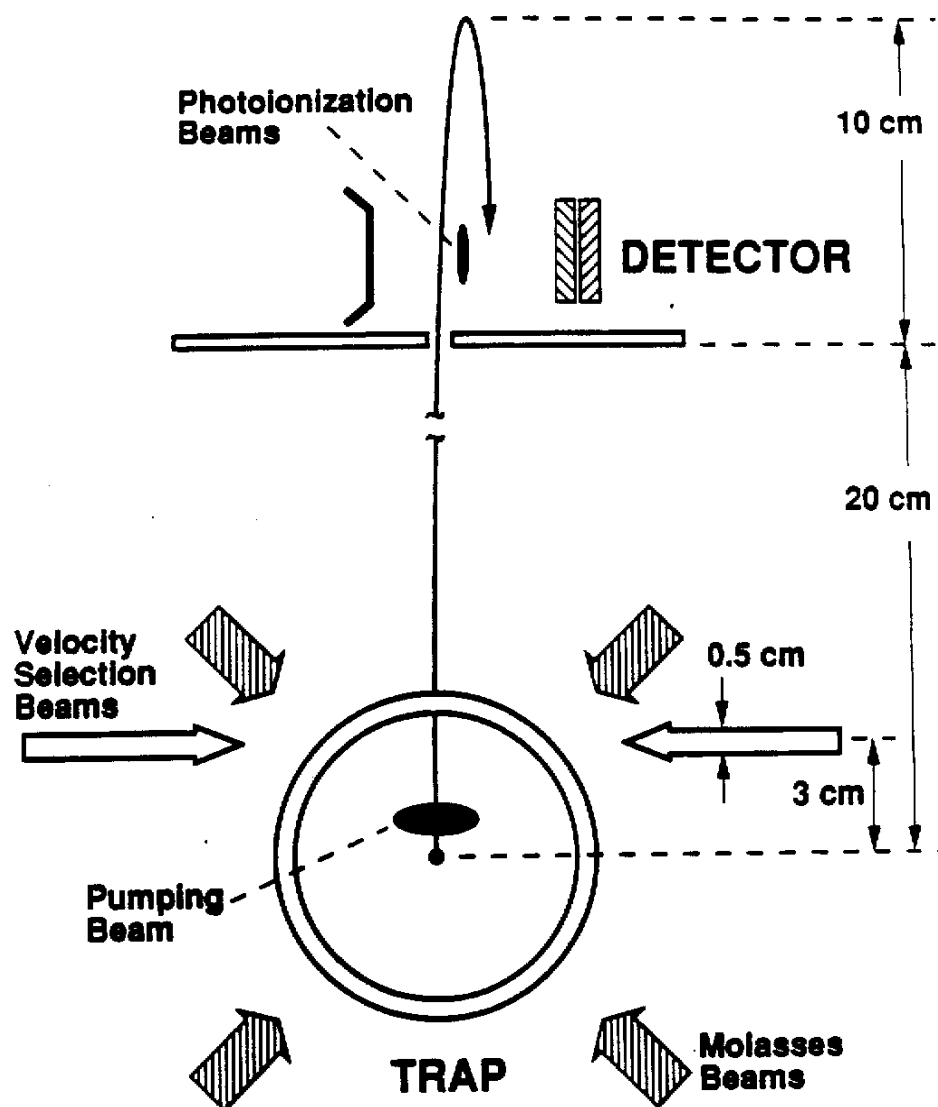
Fig. 4.2: Apparatus used to demonstrate velocity sensitive stimulated Raman transitions.

distribution of atoms in the $|2\rangle$ state was measured at two points in time: once immediately after the atoms passed through the slit (on their first transit through the detection region) and again ~230 msec later (after they had turned due to gravity and fallen back into the detection region). By comparing the width of image at two points in time we were able to place an upper limit on the velocity spread of the atoms. The width was measured by recording the number of ionized atoms as a function of the position of the 0.5 mm wide detection region. The frequency of the cw photo-ionization beam was chosen so that only atoms in the $|2\rangle$ state were ionized.

The experiment was complicated by two effects. (1) Vibration of the mirrors used to send the Raman beams into the vacuum can were large enough to Doppler shift the Raman frequency difference by an amount larger than the desired Raman linewidth. (2) For narrow velocity slices, the count rates were low. To see the resonances, background rates from incomplete optical pumping had to be minimized.

We combatted problem (1) by measuring the frequency difference of the two Raman beams just outside the vacuum can and then servoing the frequency difference to a phase stable rf source. This essentially limited the vibrationally induced frequency noise to the vibration of the elements used to overlap the beams. We addressed (2) by optimizing the optical pumping state preparation with an additional pumping beam.

4.3 APPARATUS

In this section we describe additions/modifications made to the basic fountain apparatus described in section 3.2.

A 1.6 mm x 10 mm aperture was inserted just below the detection region. The aperture could be translated along an axis perpendicular to the 10 mm edges. The 10 mm edge was also parallel to the propagation axis of the detection beams and the surface of the MCP detector.

A second Coherent 699-21 laser was used to generate the Raman beams. The pump beam for this dye laser was derived from the Ar^+ laser used for the molasses laser. With the ~1.2 watts available from the dye laser, the optical frequency of the Raman beams could be detuned ~10-20 GHz from the intermediate $3P_{3/2}$ level while keeping the

effective Rabi frequency of the transition high enough to drive a π pulse during the atom's transit time through the beams. Since the spontaneous emission background rate from the intermediate levels scales as I/Δ^2 (Δ is the detuning from the optical transition and is assumed to be large, and I is the intensity of the laser) while the two-photon Rabi frequency scales as I/Δ, the spontaneous emission background rate can be minimized by a factor of $1/\Delta$ by operating at high intensity and large detuning.

The laser was locked to Coherent's reference cavity. The frequency of the laser was set by locating the $3S_{1/2}$, $F=2 \rightarrow 3P_{3/2}$ resonances in a reference vapor cell and then detuning from this frequency with the front panel controls on the 699's electronic control box. Periodically during the course of a run the frequency of the laser was checked by verifying the location of the resonance. The locked drift rate was more than stable enough for this experiment, which could have tolerated a drift rate of more than 1 GHz/hr.

Approximately 1% of the light was split off from the main output beam and directed into the sodium vapor cell as illustrated in Fig. 4.3. The $3S_{1/2}$, $F=2 \rightarrow 3P_{3/2}$ resonance was observed by nearly retro-reflecting the light after it had passed through the cell and then visually looking for the saturated absorption dip associated with the transition (when both the incident and retro-reflected beam are in resonance with the same velocity class of atoms, there is a visible drop in cell fluorescence).

The remaining beam was divided into two beams of roughly the same intensity. One of these beams was double passed through an ~ 40 MHz IntraAction acousto-optic frequency modulator. The other beam was focussed through a 1.7 GHz home-built resonant frequency modulator. The carrier and first order sidebands had nearly equal power with ~ 30 dBm of rf drive power. In this modulation scheme, the beatnote between the high frequency sideband from the electro-optically modulated beam (beam 1) and the acousto-optically shifted beam (beam 2) drove the Raman resonance. The other frequency components contributed to the spontaneous emission background as well as AC Stark shifts of the transition frequency, but were otherwise unimportant.

After passing through their respective modulators, the beams were collimated and sent into the vacuum can. Due to the geometry of the detection region the Raman beam

Legend:

BS — 50/50 Beam splitter

— Mirror

☑ Polarizing beam splitting cube

◊ Lense

POL — Linear polarizer

EOM — Electro-optic modulator

AOM — Acousto-optic modulator
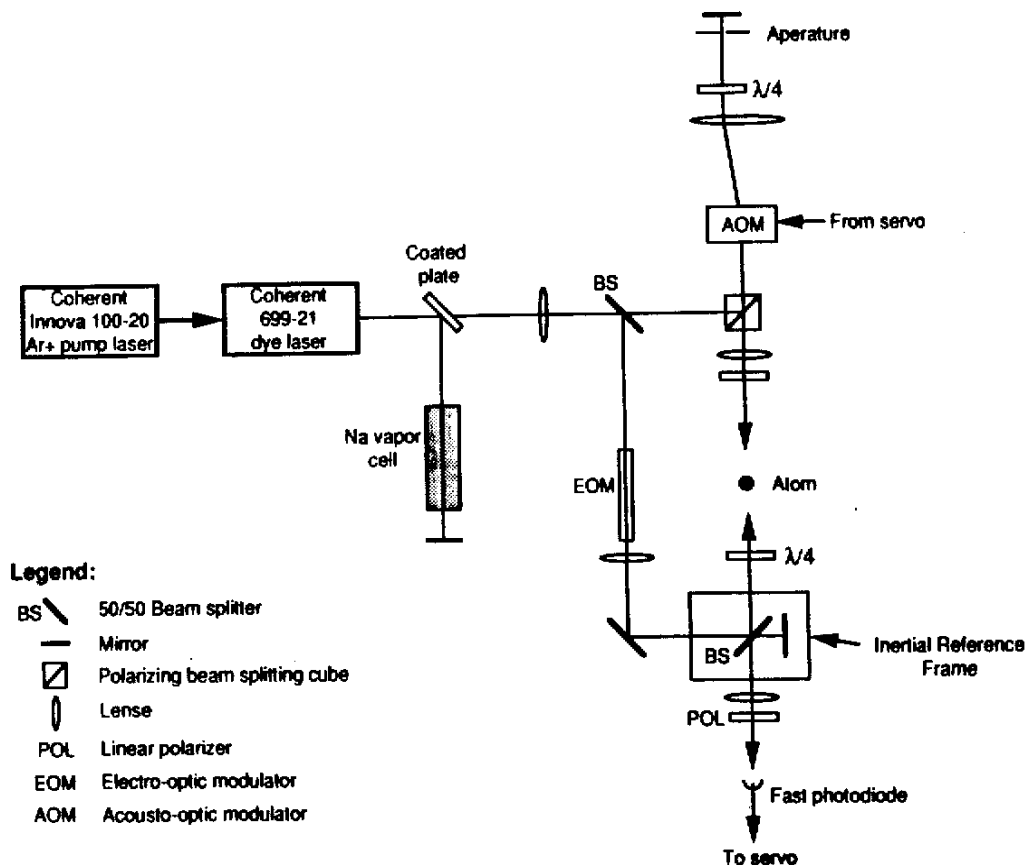
Fig. 4.3: Optics layout for demonstration of stimulated Raman transitions. The 699-21 is pumped by the same Ar^+ laser which pumps the molasses dye laser.

propagation axis was chosen parallel to the slowing beam. The two Raman beams were overlapped just outside the entrance viewport for beam 1 (at this point beam 2 was exiting the can through the same viewport). A fast photodiode (3 GHz 3 dB roll-off) measured the 1.7 GHz heterodyne beatnote between the beams. After amplification the beatnote was mixed with a stable rf reference down to near DC. The mixer output was used to phase-lock the beatnote to the rf reference by servoing the frequency of the

69

acousto-optic modulator. The open loop linewidth of the beatnote was ~5 kHz, far too large to coherently drive a sub-kHz resonance. After closing the loop, the relative phase noise between the heterodyne beatnote and stable rf source was $\pm 10°$. The reference synthesizer was slaved to a LORAN-C synchronized oscillator (SRS FS 700) which had a specified short term stability of 5 parts in 10^{11}.

The servo amplifier had variable proportional and integral gain. Since the servo actuator had integral response (the error signal was fed to the VCO which controlled the AOM's frequency), best results were obtained with high proportional gain and weak integral gain. The final phase-lock was robust enough to stay in lock when the reference synthesizer was scanned over a 1 MHz range over the course of a few minutes (the synthesizer frequency scans were *not* phase continuous, but had the characteristic switching drop-outs of a low-end signal source.)

The beams could also be aligned in a Doppler free configuration. This geometry was used to measure the transit-time limited linewidth of the transition. It was also used to align the Raman region with respect to the trap (see below) and to measure residual magnetic fields. In this case, the beams were overlapped on the same beam splitter used for the phase-lock, but this time in such a way that they co-propagated into the vacuum can. The propagation axis could be easily changed by simply adjusting the angle of the beam splitter.

A low intensity optical pumping beam intersected the flight path of the atoms before they passed through the Raman beams. The light for this beam was split off from the main molasses beam (before the molasses beam passed through the first electro-optic modulator) then double passed through a 110 MHz acousto-optic modulator. This permitted the frequency of the optical pumping light to be optimized. The intensity in this beam was ~1 mW/cm^2.

Large magnetic field coils (quasi-Helmholtz) were mounted outside the vacuum can to control the magnetic field in the interaction region. Due to space limitations, the coils which produced magnetic field components parallel to the floor of the lab were wrapped on 2'x5' rectangular forms and arranged to form a box around the apparatus. The coils for the vertical field component were 3.5' in diameter and separated by 5'.

The cw detection beam was focussed to a highly eccentric ellipse (0.5 mm minor axis, 8 mm major axis with the major axis oriented vertically). This profile provided good spatial resolution parallel to the imaging slit without sacrificing counts in the vertical dimension. Mounting the final beam steering mirrors for the detection beams on a motorized translation stage allowed the position of the detection region to be remotely scanned.

4.4 EXPERIMENTAL METHOD AND RESULTS

The Raman transitions were first studied in the Doppler free configuration to ensure that the basic atomic processes were understood. Fig. 4.4 shows all possible Raman excitation paths for sodium. A weak bias field removes the degeneracy of the
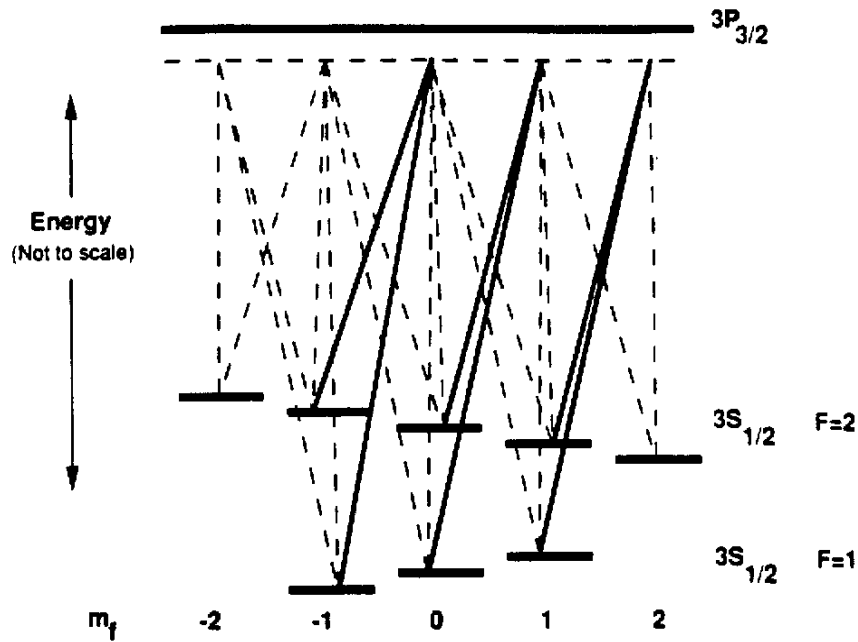
Fig. 4.4: Possible 2-photon paths for Raman transitions between sodium groundstate hyperfine levels.

71

Zeeman sub-levels. When the magnetic bias field lies parallel to the propagation axis for the Raman beams, and when the Raman beams are polarized $\sigma^+\sigma^+$ or $\sigma^-\sigma^-$ only three paths are allowed, one from each hyperfine sub-level. As shown in Fig. 4.5, this leads to a three peaked spectrum in the limit where the Raman transition linewidth is narrower than the Zeeman level splittings and assuming an initial statistical distribution of population in the F=1 Zeeman sub-levels. When the natural quantization axis for the Raman light is not parallel to the natural quantization axis for the Zeeman sub-levels (the direction of the bias magnetic field), the situation is more complicated. One way of thinking about the transitions is to project the light's polarization on the Zeeman quantization axis by use of the standard spin 1 rotation matrixes.[85] In this quantization axis the Raman beam polarization will in general consist of σ^+, linear and σ^- components, with the relative strength and phase given by the rotation matrix. As shown in Fig. 4.5, the spectrum now consists of seven peaks, again assuming an initial statistical population distribution.

AC Stark shifts destroy the even spacing of the Zeeman peaks. The size and sign of the shifts can be obtained by straightforward application of Eq. (4.7) for all allowed hyperfine transitions. The AC Stark shift is on the order of the two-photon Rabi frequency. There are no AC Stark shifts for the $m_f=0 \rightarrow m_f=0$ and $-1 \rightarrow +1$ transitions in the limit where the detuning from the optical level is large compared to the hyperfine splitting.[86]

We measured the two-photon Rabi frequency by recording the number of counts as a function of the measured intensity of the driving Raman beams. The measured value agreed to within 10% of the theoretical estimate. This measurement was complicated by the uneven sampling of the light field by atoms with trajectories which did not pass through the central region of the beams. With the laser detuned 15 GHz from the $3S_{1/2} \rightarrow 3P_{3/2}$ resonance, peak intensities of 5.5 mW/cm^2 and 15.0 mW/cm^2 were needed for σ^+ polarized beams to drive a π pulse on the $m_f=0 \rightarrow m_f=0$ transition. The Raman beam diameter was 0.5 cm 1/e^2 and the velocity of the atoms was ~2.6 m/sec. The corresponding transit-time limited linewidth was measured to be 900 Hz FWHM.

We used the Doppler free signals to zero the magnetic field and to align the
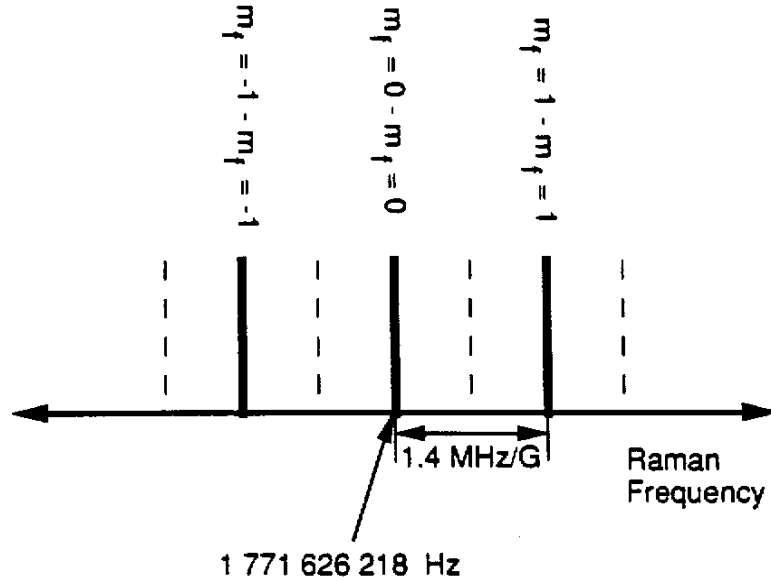
Fig. 4.5: Raman spectrum with $\sigma^+\sigma^+$ polarized beams and a bias magnetic field applied parallel to the propagation axis of the light (solid lines). Additional peaks are present when the bias field is not parallel to the propagation axis for the light (dashed lines).

Raman region with respect to the trap. We varied the Helmholtz coil currents until all Zeeman resonances nearly overlapped, then applied a bias field, if necessary, along the propagation axis of the light. We could verify that the bias field axis was parallel to the propagation axis of the light by monitoring the suppression of the odd order Zeeman peaks as illustrated in Fig. 4.5. We optimized the alignment of the Raman beams by lowering the Raman intensity so that the Raman pulse area was less than π and then by steering the beams to maximize the number of detected counts. The Doppler sensitive alignment started with the Doppler free alignment, then beam 2 was made to counter-propagate with beam 1 while the direction of beam 1 held at its Doppler free position.

Once the Doppler free spectra were understood, we switched to the Doppler sensitive configuration. Fig. 4.6 shows the measurement of the transverse spread of the atoms in the F=2 state at 140 msec and at 370 msec when the Raman beams were
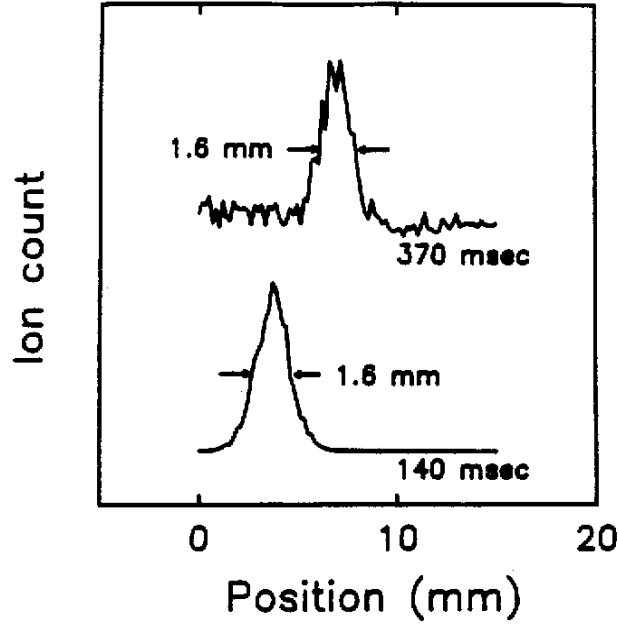
Fig. 4.6: Ballistic temperature measurement of an ultra-cold ensemble of atoms prepared with stimulated Raman transitions.

aligned to be Doppler sensitive. There was no significant spread in the width of the distribution, putting an upper limit on the velocity spread of $\Delta v < 0.1$ cm/sec (our experimental resolution). The transit-time limited linewidth for the Raman transition was measured to be 900 Hz in the Doppler free configuration. With this frequency width, the velocity spread of the selected atoms is inferred to be ~ 270 μm/sec, corresponding to an effective temperature of 24 pK and an uncertainty principle limited minimum wavepacket width of 51 μm. One of the beams was circularly polarized and the other linearly polarized, and the intensity was adjusted to irradiate the atoms with a π pulse. The probability of a spontaneous emission from the $3P_{3/2}$ state was $\sim 10^{-4}$ during the atom's flight through the beams at a 15 GHz detuning from the optical resonance.

Not shown in the figure are the background counts, measured by recording the ionization signal with the Raman beams off. The peak background level, due largely to

incomplete optical pumping, was ~ 1.4 times the peak signal. The peak counting rate at 370 msec was 30 counts/sec, 50 times less than the data rate at 140 msec. For the data taken 140 msec after the launch, the magnetic field was reduced to ~3 mG, measured by making the beams co-propagate and tuning the light to the field sensitive transitions. (The excitation of the magnetic field sensitive transitions when the beams are in the velocity sensitive mode translates into an additional width of ~150 μm contributing to the 1.6 mm width in Fig. 4.6). The data at 370 msec were taken with an 80 mG bias field to separate the magnetic field insensitive $m_f=0 \rightarrow m_f=0$ and $m_f=-1 \rightarrow m_f=+1$ transitions from the field sensitive $m_{f=}\pm1 \rightarrow m_{f=}\pm1$ and $m_f=0 \rightarrow m_f=+2$ transitions. The bias field was chosen to be large enough so that atoms in velocity classes selected by the field sensitive transitions ballistically separated from those excited by the field insensitive transitions by the time of detection.

Our ability to resolve narrow velocity slices was limited by the optical pumping background of 3 parts in 10^4 unpumped $F=2$ atoms to optically pumped $F=1$ atoms. In order to achieve this level we needed the extra optical pumping beam shown in Fig. 4.2. In the steady state, we expect the optical pumping background rate to be limited by the off-resonant excitation rate from the $F=1$ level and the on-resonant rate out of the $F=2$ state. Using Eq. (2.2) and the sodium oscillator strengths tabulated in Appendix A, we estimate the steady state background to be ~1×10^{-4} when the frequency of the pumping beams is tuned near the $3P_{3/2}$, $F=1,2$ transitions, in reasonable agreement with the observed value. Fig. 4.7 shows our measurement of the background rate as a function of frequency of the pumping beam. Consequently, for the data of Fig. 4.6, we tuned the pumping beams midway between the $3P_{3/2}$, $F=1$ and $3P_{3/2}$ $F=2$ transition. Background counts due to spontaneous emission during the Raman pulse and off-resonant excitation during the photo-ionization contributed negligibly to the background rate of Fig. 4.6.

The above experiment shows that Doppler sensitive Raman transitions can be used to prepare narrow velocity ensembles. The transitions, however, can also be used to measure velocity distributions. As a demonstration of this powerful capability, we measured the transverse temperature of the fountain source by probing the velocity

Background level (arb units)

140
120
100
80
60
40
20
0

-80   -60   -40   -20   0   20

Detuning from 2-2 transition
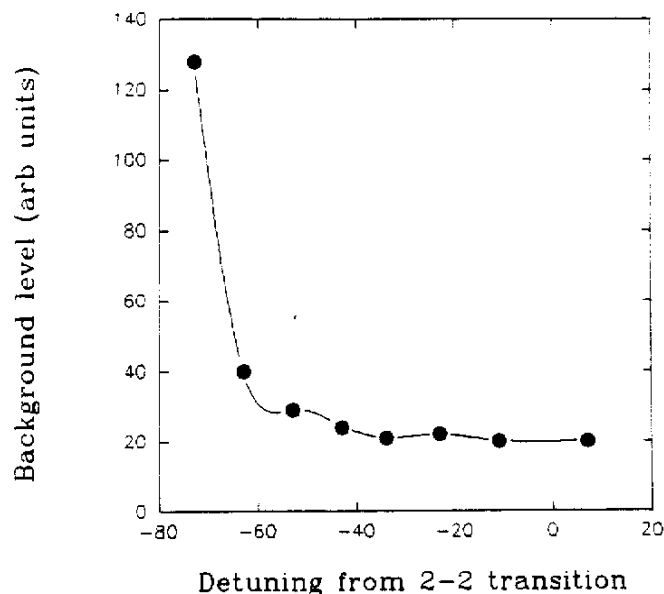
Fig. 4.7: Background counts in F=2 state vs. detuning of optical pumping beams.

distribution with stimulated Raman transitions. (Doppler sensitive 1-photon uv transitions have been previously used to probe the molasses temperature distribution. This work required an ultra-stable laser and the linewidth of the meta-stable uv transition was only a factor of 3 narrower than the Doppler width of the measured distribution.[87]) Fig. 4.8 shows the number of detected atoms as a function of the center frequency of the Raman beams. For this measurement the imaging slit was removed and the atoms were detected on their first pass through the detection region. The fitted temperature of 38 ± 2 μK agreed well with the ballistically determined value of 35 ± 7 μK for the vertical velocity spread, if the horizontal and vertical velocity spreads in the optical molasses were the same. The ballistic measurement was inferred from a time of flight scan similar to that shown in Fig. 3.9. The range of the frequency scan in Fig. 4.8 was limited by the spatial aperture of the MCP detector.
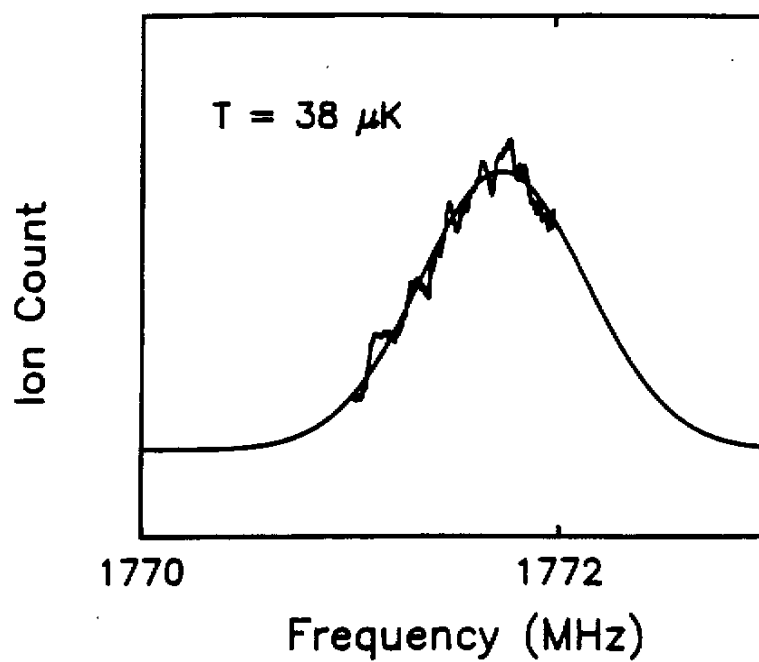
Fig. 4.8: Molasses temperature measurement with stimulated Raman transitions.

SECTION 5

ATOMIC INTERFEROMETER

Matter-wave interference with atoms has recently been demonstrated by several groups. Fringes have been observed by diffraction from two material slits in the Young's double slit geometry.[28] Interference has also been observed by diffraction from micro-fabricated gratings in a three-grating geometry.[29] The mechanical effects of light can also used to spatially separate and interfere atomic wavepackets.[27,88] In this vein, interference effects have been demonstrated for an atomic beam interacting with four laser beams.[20] We have also demonstrated interference using laser cooled atoms and a series of three light pulses.[16,17]

In 1975, Colella, Overhauser and Werner demonstrated that the acceleration of a neutron due to gravity could be measured with a matter-wave interferometer.[32] Clauser subsequently noted that the inertial sensitivity of an atom interferometer could exceed that of a neutron interferometer, largely due to the atom's mass advantage and to the potential availability of sources of slow atoms.[89] Experimental demonstration of the sensitivity of atom interferometers to inertial forces came in the first generation of light-pulse atom interferometers based on pulse sequences.[16,20]

Atom interferometers can be used as sensitive accelerometers in a variety of precision experiments which search for weak forces. Examples of such experiments include searches for net charge on atoms, "fifth" force experiments, and tests of general relativity. Accurate inertial sensors have practical applications in oil-well logging and navigation. Geophysical applications include earthquake prediction and studies of global warming.[90]

Although the emphasis of this research has been on the experimental demonstration of high sensitivity to accelerations, the sensitivity is coupled to large ($\sim$ 6 mm) wavepacket separations. Along these lines, atom interferometers can be used for novel tests of quantum mechanics. Examples include observation of the Aharonov-

Casher effect,[34] 'which-path' experiments,[91] and Berry's phase measurements.[92]

Light-pulse interferometers work on the principle that when an atom absorbs or emits a photon, momentum must be conserved between the atom and the light field. Consequently, an atom which emits (absorbs) a photon of momentum $\hbar k$ will receive a momentum impulse of $\Delta p = -\hbar k$ $(+\hbar k)$. When a resonant travelling wave is used to excite an atom, the internal state of the atom becomes correlated with its momentum: an atom in its ground state $|1\rangle$ with momentum p (labelled $|1,p\rangle$) is coupled to an excited state $|2\rangle$ of momentum $p+\hbar k$ ($|2,p+\hbar k\rangle$).[27]

We used a $\pi/2$-π-$\pi/2$ pulse[93] sequence to coherently divide, deflect and finally recombine an atomic wavepacket (see Fig. 5.1). The first $\pi/2$ pulse excites an atom initially in the $|1,p\rangle$ state into a coherent superposition of states $|1,p\rangle$ and $|2,p+\hbar k\rangle$. If state $|2\rangle$ is stable against spontaneous decay, the two wavepackets will drift apart by a distance $\hbar kT/m$ in time T. Each wavepacket is redirected by a π pulse which induces the transitions $|1,p\rangle \rightarrow |2,p+\hbar k\rangle$ and $|2,p+\hbar k\rangle \rightarrow |1,p\rangle$. After another interval T the wavepackets once again overlap. A final $\pi/2$ pulse cause the two wavepackets to interfere. The interference is detected, for example, by measuring the number of atoms in the $|2\rangle$ state.

We obtained large wavepacket separations by using laser cooled atoms in an atomic fountain geometry[11] and velocity sensitive stimulated Raman transitions to drive the transition.[6] The atomic fountain geometry allows the drift times T to be on the order of a second. Stimulated Raman transitions give large recoil kicks in transitions between ground-state hyperfine levels.

Interference was demonstrated for the two geometries illustrated in Fig. 5.1. In the Mach-Zehnder geometry, the mean velocity of the atoms is perpendicular to the light beams. In the gravimeter geometry, the mean velocity is parallel to the light beams. The area that the two interferometer arms enclose is typically quoted as a figure of merit for an interferometer's sensitivity to inertial effects. This is a misleading and sometimes incorrect measure of our interferometer's sensitivity to acceleration. As shown in section 5.1, sensitivity to acceleration is maximized when the perturbing force acts parallel to
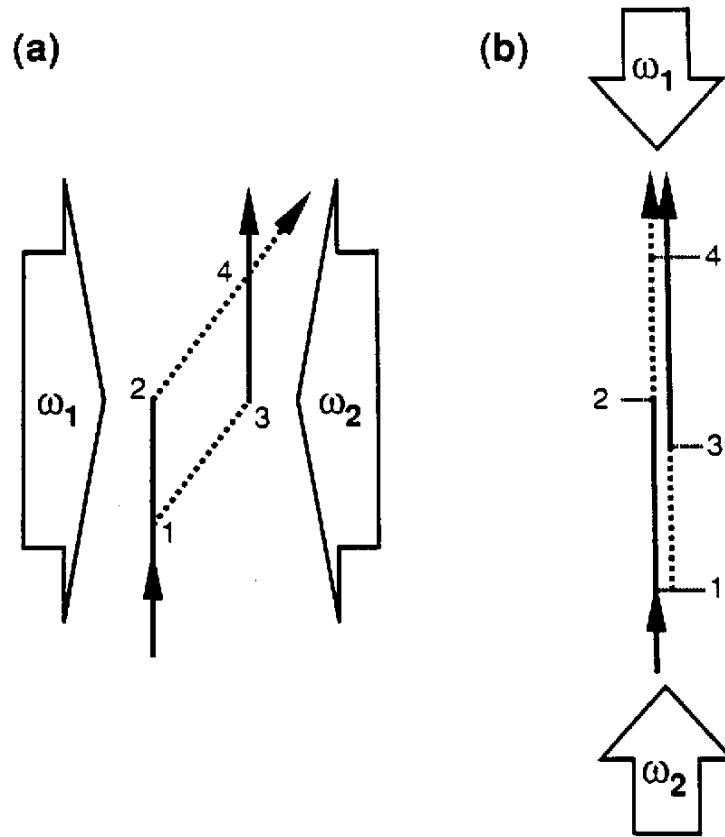
Fig. 5.1: (a) Mach-Zehnder configuration (b) Gravimeter configuration

the axis of the light beams, regardless of the area of the interferometer. In the special case where the acceleration results from the Coriolis force $f_c = 2\Omega x v$,[94] the fact that the force acts orthogonally to the atom's mean velocity has the consequence that sensitivity is maximized when area is maximized.

As described in section 1, the measurement of gravity in a light-pulse interferometer may also be viewed as a novel class of high-resolution spectroscopy. Here the object of study is not the absolute frequency of a resonance, but rather the Doppler shift of the resonance, or in the case of the measurement of gravity, the change

in the Doppler shift with respect to time. In this view, the extraordinary sensitivity to gravitational acceleration is a consequence of the long measurement times, hence narrow transit-time limited resonances, available in an atomic fountain and the large Doppler sensitivity of velocity sensitive stimulated Raman transitions. This perspective may provide perhaps the most straightforward route to understanding the how the $\pi/2$-τ-$\pi/2$ pulse sequence is sensitive to g in the gravimeter configuration. With this in mind, we have chosen to first present the theory of operation of the interferometer as a Doppler sensitive spectrometer (section 5.1.1).

Although rigorous, this treatment has its shortcomings in terms of providing an intuitive model with predictive power. Thus in section 5.1.2 we present the theory from the alternative viewpoint of matter-wave interference. This perspective stresses the physical separation of wavepackets as well as phase shifts resulting from the atom's interaction with the light field. It provides a more natural matrix for understanding systematic perturbing influences.

Section 5.1.3 presents numerical results directly pertinent to our experimental demonstration. These results are included to provide a quantitative basis for interpreting the sensitivity of the interference contrast to the small deviations from ideal which would be present in any realistic experiment (eg., what is the contrast for a $\pi/2$-τ-$\pi/2.1$ pulse sequence?).

Section 5.2 begins discussion of the fountain-based interferometer experiments by summarizing the basic experimental philosophy and describing in general terms the evolution of experimental technique over the course of the experiment. Section 5.3 details the actual implementation of our most successful (eg. best resolution) scheme. Since the particular implementation methods changed dramatically from the first observation of interference, some space is devoted to justifying the latest practices against the backdrop of earlier work. Finally, results are presented in section 5.4.

5.1 INTERFEROMETER THEORY

In the absence of any external forces acting on the atom, the solutions to Eqs. (4.6) and those for the free evolution of the wavepacket can be used to obtain the final

state of the atom after the $\pi/2$-π-$\pi/2$ interferometer pulse sequence. We show below that the final state of the atom depends on the phase of the Raman light field driving the transition. This result is readily extended to an atom falling in a gravitational field. In the reference frame falling with the atom, the Raman light field's frequencies appear to be Doppler shifted linearly with time. This frequency chirp shows up as a quadratic shift in the *phase* of the field as a function of time.

In section 4.1 we analyzed the atom's center of mass motion in terms of momentum eigenstates. In section 5.1.1 we analyze interferometer phase shifts in terms of momentum eigenstates. This has the advantage that the calculations are straightforward but the disadvantage that the range of applicability of the solutions is limited. For example, it is awkward to handle external electric or magnetic field gradients in this basis set. The phase shifts can also be viewed in terms of the wavepacket's mean position. This view is presented in section 5.1.2. In section 5.1.3 we discuss the issue of fringe visibility in the context our interferometer experiment.

5.1.1 *Phase shifts for momentum eigenstates*

In the limit of short, intense pulses ($\Omega_{eff} \gg \delta_{12}$) Eqs. (4.6) can be solved for the amplitudes $a_{1,p}$ and $a_{2,p+2\hbar k}$ (taking $k_1 \approx -k_2$) immediately following a $\pi/2$ or π pulse. For a $\pi/2$ pulse of duration $\tau/2$, or a π pulse of duration τ, the amplitudes are[95]

$$a_{1,p}(t+\tau/2) \quad = \sqrt{\tfrac{1}{2}}\left[a_{1,p}(t) - ie^{+i\phi(t)}a_{2,p+2\hbar k}(t)\right] , \quad (\pi/2 \; pulse)$$

$$a_{2,p+2\hbar k}(t+\tau/2) = \sqrt{\tfrac{1}{2}}\left[-ie^{-i\phi(t)}a_{1,p}(t) + a_{2,p+2\hbar k}(t)\right] , \quad (5.1)$$

$$a_{1,p}(t+\tau) \quad = ie^{+i\phi(t)}a_{2,p+2\hbar k}(t) , \quad (\pi \; pulse)$$

$$a_{2,p+2\hbar k}(t+\tau) \quad = -ie^{-i\phi(t)}a_{1,p} ,$$

where

$$\phi(t) = \int_{t_0}^{t} \delta_{12}(t')dt' \quad .$$ (5.2)

During the period between pulses, the free evolution is

$$a_{1,p}(t+T) = a_{1,p}(t) \;,$$

$$a_{2,p+2\hbar k}(t+T) = a_{2,p+2\hbar k}(t) \;.$$ (5.3)

(Note that the explicit time dependence of the amplitudes has been factored out in the definition of $a_{\alpha,p}(t)$ in Eq. 4.3). Evaluating Eqs. (5.1) and Eqs. (5.2) for the three pulse interferometer sequence leads to the following expression for the transition probability to state $|2\rangle$ for an atom initially prepared in state $|1\rangle$:

$$a_{2,p+2\hbar k}(2T+2\tau) = \tfrac{1}{2}(e^{-i\Delta\phi} + 1) \;,$$ (5.4)

where

$$\Delta\phi = \phi(t_1) - 2\phi(t_2) + \phi(t_3)$$ (5.5)

and t_1 is the time of the first $\pi/2$ pulse of width $\tau/2$, $t_2 = \tau/2 + T + t_1$ is the time of the π pulse and $t_3 = 3\tau/2 + 2T + t_1$ the time of the final $\pi/2$.

$\Delta\phi$ does not vary with the initial momentum of the atom. This has the important consequence that a large spread in initial velocities can coherently contribute to the interference signal. Eq. (5.5) was derived for one momentum component of a wavepacket. Since it is independent of momentum, the phase shift for a spatially localized wavepacket, which is a coherent sum over momentum states, is also given by this equation. Specifically, for ω_1,ω_2 independent of time, $\Delta\phi = 0$.

AC Stark shifts do not contribute to the net shift $\Delta\phi$ if the intensity of the Raman field remains constant for all three pulses. Consequently, phase shifts associated with the AC Stark terms have been suppressed in Eqs. (5.1).

Next consider an atom which is falling in a gravitational field. In the frame falling with the atom the Raman frequency changes linearly with time at the rate of $(k_1-k_2) \cdot gt$. Evaluating Eq. (5.5) with $\omega_1-\omega_2 \rightarrow \omega_1 -\omega_2 - (k_1-k_2) \cdot gt$ gives

$$\Delta\phi = -(k_1-k_2) \cdot g\, T^2 \ . \tag{5.6}$$

For sodium, with k_1, k_2 parallel to g, $(k_1-k_2)g \sim 2\pi \times 3.3 \times 10^7$ sec^{-2}.

In the experiment the effective Rabi frequency was ~ 50 kHz, whereas the change in the Doppler shifts, $\sim 2k_1 gT$, was greater than 3 MHz. Thus a momentum component in resonance with the first $\pi/2$ pulse will be far out of resonance with the remaining pulses. By actively changing the frequency difference $\Delta\omega(t) = \omega_1(t)-\omega_2(t)$, we compensated for the atom's deceleration. We changed $\omega_1(t)-\omega_2(t)$ so that, for each Raman pulse, the detuning from resonance was less than the Rabi frequency. The atom is resonantly driven for all three pulses when $\Delta\omega = \omega_0$ for the first $\pi/2$ pulse, $\Delta\omega = \omega_0+\omega_m$ for the π pulse, and $\Delta\omega = \omega_0+2\omega_m$ for the final $\pi/2$ pulse, with $\omega_m \sim (k_1-k_2) \cdot gT$. In the falling frame, the phase of the Raman field before each Raman pulse is $\omega_0 t_1 + \phi_1^0$, $(\omega_0+\omega_m)t_2 - (k_1-k_2) \cdot gt_2^2 + \phi_2^0$, and $(\omega_0+2\omega_m)t_3 - (k_1-k_2) \cdot gt_3^2 + \phi_3^0$ respectively. In this case, $\Delta\phi = 2\omega_m T - (k_1-k_2) \cdot gT^2 + \Delta\phi^0$. The term $\Delta\phi^0 = \phi_1^0 - 2\phi_2^0 + \phi_3^0$ represents the initial phase relationship between the three pulse frequencies. If each of the three frequencies is derived from an independent synthesizer, the ϕ_i^0's are interpreted as the phase of the ith synthesizer at time $t=0$. (eg. $\phi_i(t) = \Delta\omega_i t + \phi_i^0$ is the phase of the ith synthesizer).

Rather than using three independent frequencies, the resonance could equally well have been maintained by a phase continuous sweep of the frequency difference $\Delta\omega$, so that $\Delta\omega(t) = \omega_0+\beta(t-t_0)$. Evaluation of Eq. (5.5) in the falling frame, for this condition, gives $\Delta\phi = [\beta-(k_1-k_2) \cdot g]T^2$. When $\beta=(k_1-k_2) \cdot g$ there is no relative phase shift: the Doppler shift is exactly canceled by the frequency sweep of the Raman driving field. Note that this expression is insensitive to the time origin of the sweep (t_0). The accuracy of the phase continuous sweep is critical if the full resolution for the interferometer is to be realized. The introduction of direct frequency synthesis techniques allows phase

84

continuous sweeps while remaining locked to a stable frequency reference oscillator.

5.1.2 *Phase shifts for wavepackets*

The method of section 5.1.1 shows the origin of gravitationally induced phase shifts to be Doppler shifts of the Raman field. However, it does not provide a useful framework for understanding phase shifts due to non-inertial forces. An alternative approach, which can account for non-inertial forces, views phase shifts in terms of the position of the wavepacket.[16,20] In this approach, contributions to $\Delta\phi$ fall into two classes: those arising from the atom's interaction with the light ($\Delta\phi_l$) and those arising during the atom's free evolution between light pulses ($\Delta\phi_f$). The first take the form

$$\Delta\phi_l = \phi_R(x_1^1,t_1) - \phi_R(x_2^1,t_2) - \phi_R(x_2^2,t_2) + \phi_R(x_3^1,t_3) , \qquad (5.7)$$

where $\phi_R(x,t) = (k_1-k_2)\cdot x - \Delta\omega t$ is the phase of the Raman field at position x and time t. The position vectors x_i^α represent the mean position of the wavepacket correlated with internal state α at the time t_i of the ith pulse. When the action $S = \int_\Gamma L dt$ (L the Lagrangian for the atom) is much greater than $\hbar$, the free evolution contribution is[96]

$$\Delta\phi_f = \int_\Gamma k_a \cdot dx - \omega_a dt , \qquad (5.8)$$

where Γ is the circuit describing the path of the wavepackets, k_a = (wavepacket's mean momentum p)$/\hbar$, and ω_a = (total mean energy of wavepacket)$/\hbar$.

Evaluation of Eq. (5.7) for the gravitationally perturbed wavepacket trajectories which occur in a $\pi/2$-π-$\pi/2$ pulse sequence yields the result obtained in section 5.1. The free evolution contribution from Eq. (5.8) turns out to be zero if there is no violation of the equivalence principle: the contribution from the asymmetry in deBroglie wavelengths is canceled by the changes in the atom's total energy. This is in contrast to neutron interferometers where the free evolution contribution *is* the dominant phase shift.[97] The distinguishing feature between the two cases is that the energy of the atom is not conserved during the light pulses of our interferometer while it is conserved during the Bragg reflection processes of neutron interferometers.

85

5.1.3 *Fringe visibility*

Fringe visibility $V=(P_{max}-P_{min})/(P_{max}+P_{min})$ quantifies the extent to which wavepacket interference is experimentally observable. For our interferometer P_{max} and P_{min} are the maximum and minimum probabilities of finding the atom in state $|2\rangle$ after the $\pi/2$-π-$\pi/2$ pulse sequence. If the conditions for the validity of Eqs. (5.1) are satisfied, the visibility is 100%. However, the assumption that the Rabi frequency be much larger than the detuning from the transition is not true for all atoms contributing to the signal. The Doppler width of the laser cooled source of atoms is 600 kHz while the maximum Rabi frequency used was 50 kHz. Consequently, not all atoms see a $\pi/2$-π-$\pi/2$ pulse sequence because some are Doppler shifted out of resonance with the Raman beams. Contributions from off-resonant atoms are calculated by using the exact solutions
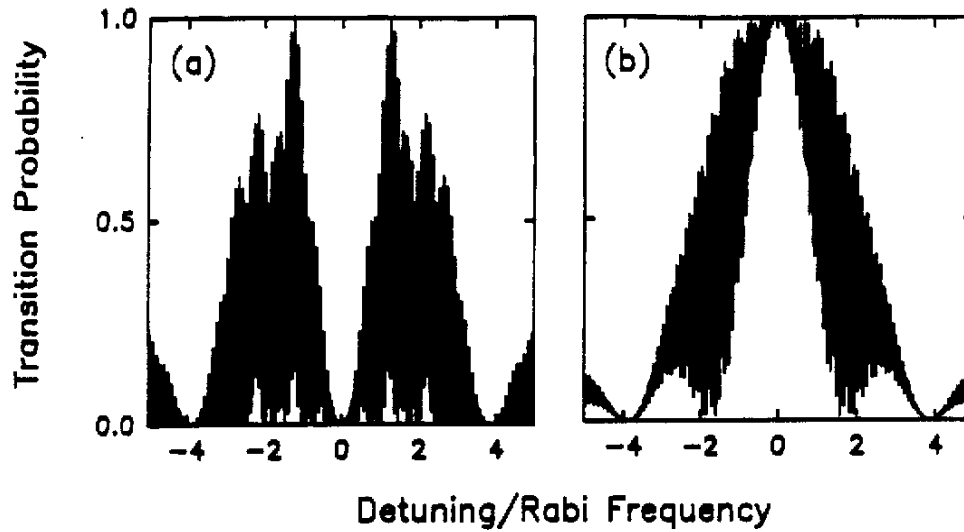
Fig. 5.2: (a) Transition probability vs. detuning (all pulses in phase) (b) Transition probability vs. detuning (180° phase shift for final $\pi/2$ pulse).

to Eqs. (4.6) rather than the approximate ones given by Eqs. (5.1). Fig. 5.2 shows the probability of excitation to level 2 following a $\pi/2$-π-$\pi/2$ sequence as a function of the atom's detuning from the resonance. In Fig. 5.2b the phase of the final $\pi/2$ pulse is shifted by π radians with respect to the first two pulses. In Fig. 5.2a all pulses are in phase. In the limit where the Doppler width of the source of atoms is much larger than the Rabi frequency, P_{max} and P_{min} are obtained by integrating the excitation probabilities over detuning (velocity). The resulting visibility is 28% in the limit where T $\gg$ τ. The approximations for the validity of Eqs. (5.1) amount to considering only those detunings near the center of curves of Figs. 5.2a,b.

We have numerically explored the quality of the fringe contrast in the event of imperfect pulse sequences to provide a quantitative gauge of how well our experimental parameters needed to be controlled. Fig. 5.3a,b,c plots contrast as a function of the width of the first pulse, second pulse and third pulse respectively. Fig. 5.4 shows contrast as a function the time delay between the second and third pulses. This figure demonstrates the important result that the time intervals $|t_3\text{-}t_2|$ and $|t_2\text{-}t_1|$ need only be balanced to order $1/\Omega_r$. All of these plots apply to the limit where the Rabi frequency is much less than the Doppler width of the source (as in the previous paragraph), and were generated by first evolving Eqs. (4.6) and (5.3) for the specified pulse parameters and a given detuning and then integrating over detuning. The mean time between pulses was taken to be $\Omega_r t = 20\pi$ except for Fig. 5.4, where the second delay was varied between 16π and 24π.

It is useful from an experimental perspective to have a method for determining when the pulse areas of the interferometer pulses have been set correctly. In the limit where the source Doppler width is much less than the Rabi frequency (ie. Doppler free excitation) this can be done by scanning the pulse width to observe Rabi oscillations. In the Doppler sensitive limit, however, the Rabi oscillations tend to wash out. Fig. 5.5 shows the calculated velocity-averaged transition probability for the $\Omega_r \ll$ (Doppler width) limit. A π pulse width is approximately that corresponding to the first maximum in transition probability.

In the limit where $\Omega_r \ll$ (Doppler width) the interferometer contrast does not

$$\frac{\Omega_r}{2\pi} (\tau - \tau_0) \quad (\Omega_r \tau_0 = \frac{\pi}{2}, \pi)$$
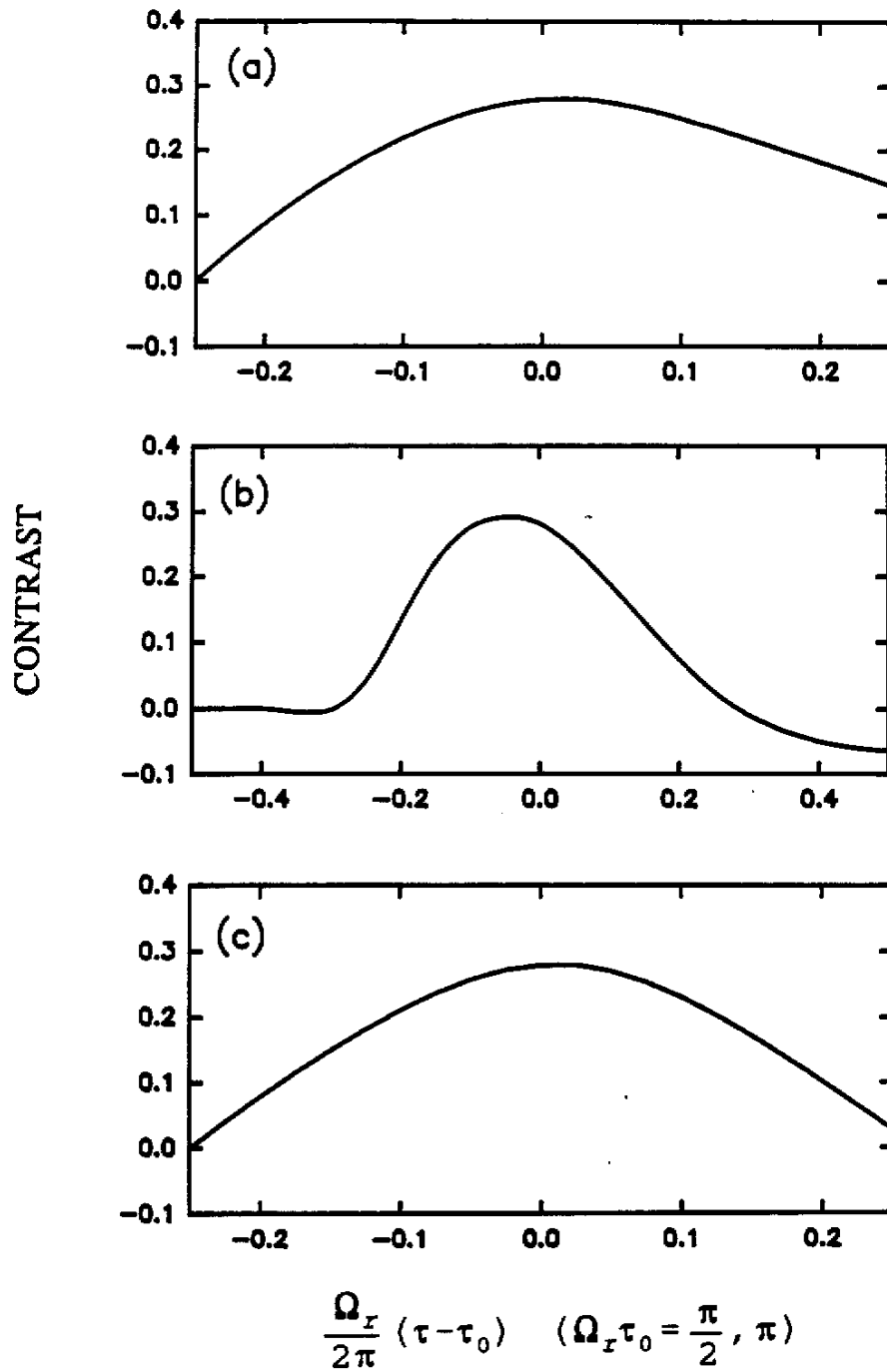
Fig. 5.3: (a) Interferometer contrast vs. width of first $\pi/2$ pulse (b) Contrast vs. width of π pulse (c) Contrast vs. width of final $\pi/2$ pulse
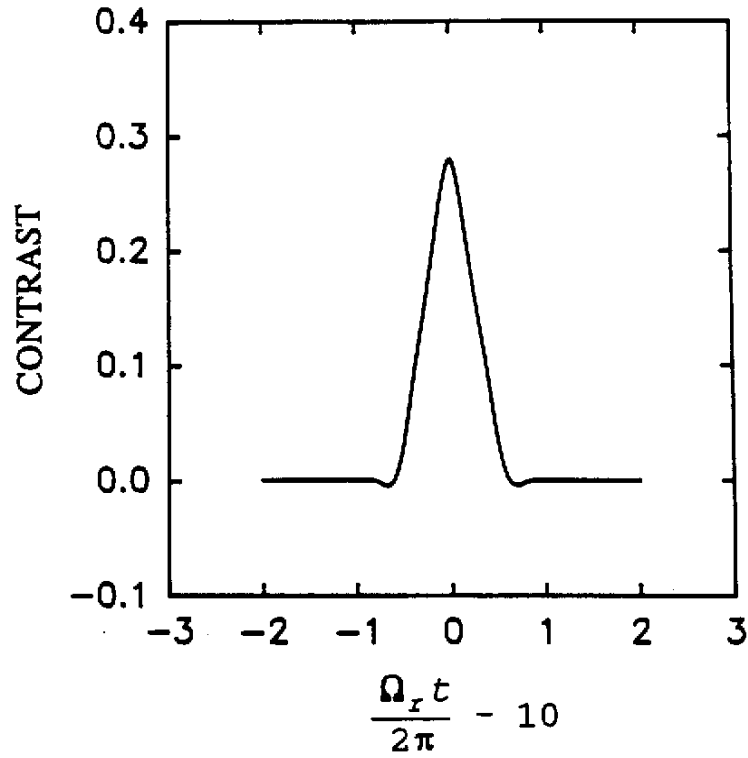
Fig. 5.4: Contrast vs. second delay time

change when the Rabi frequency (and corresponding pulse widths) are uniformly changed. From the perspective of a count-rate limited experiment, however, there is incentive to going to higher Rabi frequencies. The number of atoms that contribute to the interferometer resonance is directly proportional the width of the velocity class in resonance with the Raman light. For a fixed pulse area, this is proportional to the Rabi frequency. One way of driving up the Rabi frequency is detuning closer to the optical resonance. This, however, leads to a higher spontaneous emission background rate. The ratio of the signal size to spontaneous emission background rate is

$$R \propto \frac{\Omega_r}{\left[\dfrac{I}{\Delta^2}\right]t} \propto I \quad , \tag{5.9}$$

since $\Omega_r t$ = const. Remarkably, this is independent of detuning. This scaling breaks down as Ω_r approaches the source Doppler width or when the probability of spontaneous emission per atom per pulse is no longer much smaller than unity (in which case the full density matrix equations need to be solved). If the experiment were purely shot-noise limited, the signal-to-noise ratio would improve as the Raman laser was detuned closer to the line.
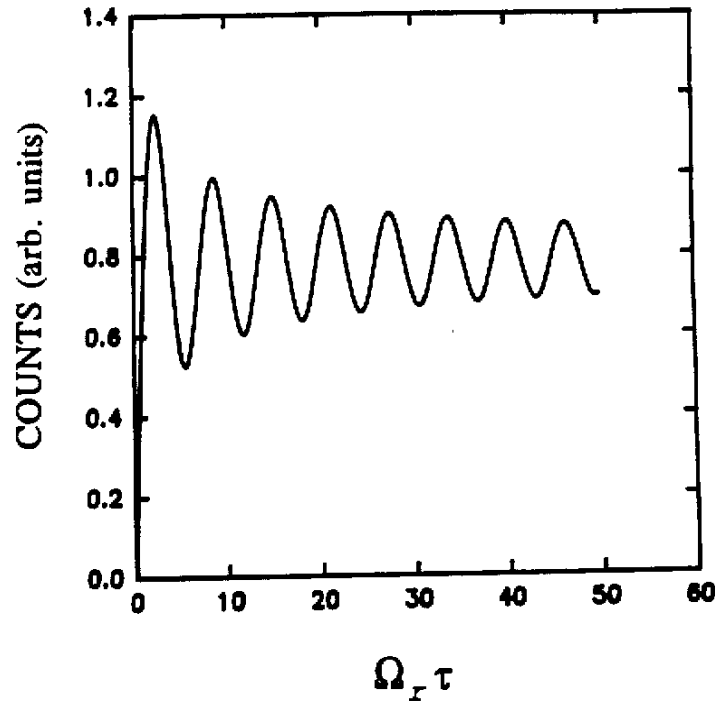
Fig. 5.5: Rabi oscillations in the limit (Doppler width of source) ≫ Rabi frequency.

90

5.2 INTERFEROMETER EXPERIMENT

Three successive pulses of divided, redirected and finally recombined an atomic wavepacket. Atoms were initially launched in the $F=1$ state as described in section 3. During their flight to the detection region they were subjected to the three pulse interferometer sequence. Interference was observed by measuring variations in the number of atoms detected in the $F=2$ state. The number of detected atoms was varied, for example, by scanning the rf phase of the final interferometer pulse. A schematic illustration of the experiment is shown in Fig. 5.6.

For our first experimental efforts we used a phase-locking scheme similar to that described in section 4.3 to stabilize the Raman frequency. However, since it was necessary to stabilize against vibrations of the phase of the Raman light field (ie. the distance of the atom to the beam-splitter) for the duration of the interferometer pulse sequence, we could no longer simply mount the beam splitter on our unfloated optical table.

We demonstrated interference in the Mach-Zehnder configuration by using large beams (~ 2 cm $1/e^2$ diameter) oriented horizontally, in a geometry similar to that described in section 4.3. Atoms were launched vertically through the beams, and the three light pulses occurred during the atom's transit time through the one beam. This limited the maximum interaction time to ~ 3 msec. To combat vibrations, interferometer components were mounted on a vibration isolation stack which rested on the optical table. The stack consisted of two isolation stages, each stage consisting of a layer of packing foam sandwiched beneath a heavy (20 kg) brass plate.

In the gravimeter configuration, the Raman beams were oriented vertically and centered on the magneto-optic trap. The maximum interaction time could in principle be limited by the parabolic flight of the atom to the detection region -- as long as 600 msec. In fact, it was limited by vibration of the beamsplitter and pointing instability in the Raman beams to a maximum of 80 msec. Vibration isolation was achieved by mounting the beamsplitter assembly on a brass plate suspended from the ceiling by surgical tubing.

In subsequent experiments we made several changes in order to improve the
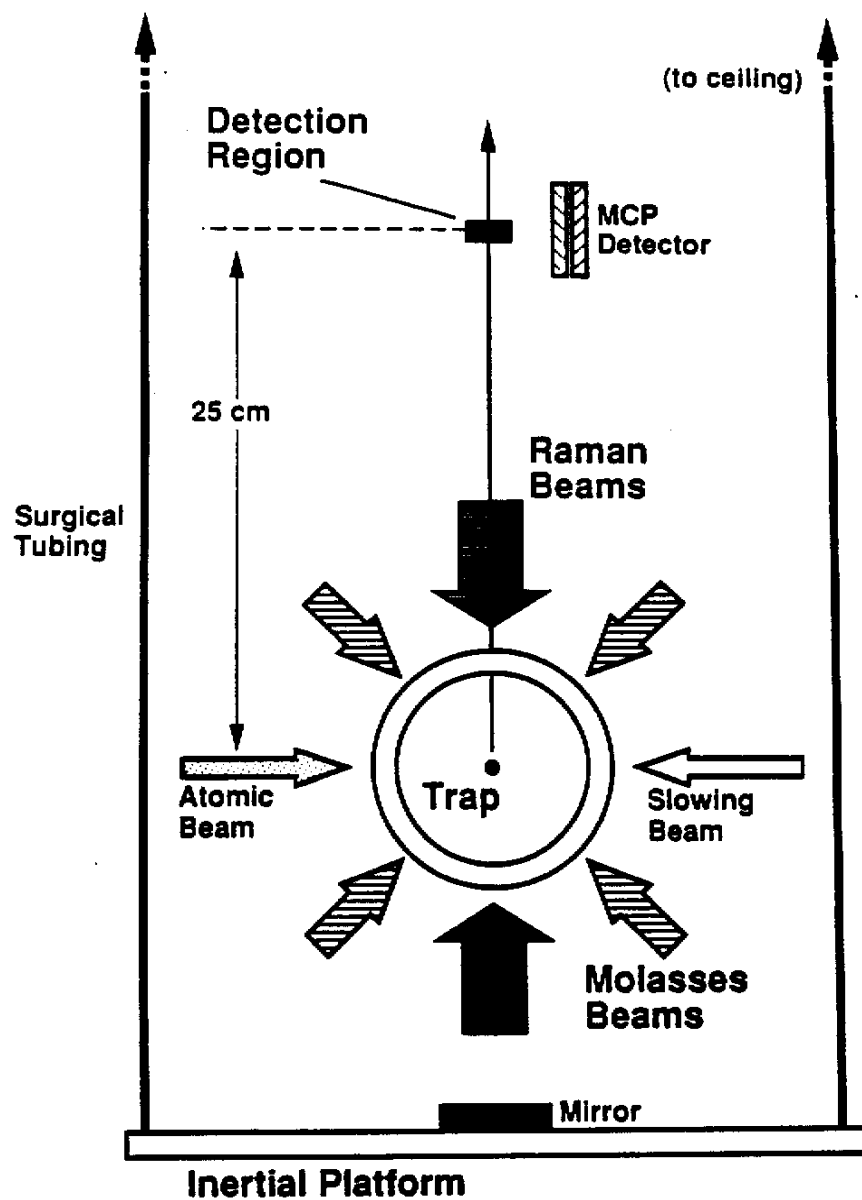
Fig. 5.6: Schematic of the apparatus used to demonstrate the light-pulse atom interferometer.

gravimeter's performance. The most significant change was in the method we used to drive the Raman transitions. In the new scheme, the output of the Raman laser was sent through an electro-optic modulator tuned to the Raman resonant frequency. The output of the EOM was fed into a polarization preserving fiber after which it was collimated and steered into the vacuum can. The beam was retro-reflected from a vibrationally isolated mirror. Experimentally, this method had several benefits. (1) It eliminated the phase-locking of the ω_1 and ω_2 beams (as shown in Fig. 4.3). This made the experiment easier to run, as the alignment for the phase-lock was delicate, and would drift in time as the surgical tubing supporting the inertial platform stretched or contracted. It also eliminated systematic offsets associated with the finite acquisition time of the phase-lock. In order to accommodate rapid pulsing of the light field, a two step process was originally used to turn on the beams. First, the light was pulsed on, but the electro-modulator was left off. The ~ 60 MHz beatnote between the AO shifted beam and the unmodulated EO beam was phase-locked to a 60 MHz reference oscillator. (This is in contrast to the experiment described in section 4.2 where the lock frequency was 1.7 GHz). Approximately 40 μsec were needed to allow the phase-lock to capture and stabilize. After the phase-lock stabilized, the EOM was pulsed on at ~ 1.71 GHz to drive the Raman transition. So for 40 μsec before each Raman pulse the atom was exposed to AC Stark shifting light and also light which would lead to a signal background via spontaneous emission. When the transition was driven directly, the phase-lock acquisition cycle was no longer needed. (2) It delivered more power to the Raman beams (even with an optical fiber). This, in turn, allowed the use of a larger beam waist (4 cm $1/e^2$ diameter), which lead to a more homogeneous intensity distribution for atoms confined to the center 1 cm diameter of the beam. We were also able to run with higher Rabi frequencies and thus achieve higher count rates. (3) The polarization preserving optical fiber stabilized against the initial pointing instability of the Raman laser beams (due ultimately to instability in the Ar^+ pump laser output). It also spatially filtered the beams, and thus improved wavefront quality.

Although experimentally beneficial, the new driving scheme complicated matters theoretically (see section 4.1.2) by adding extra spectral components to the light field

driving the transition, and also meant that we had to be more careful in choosing our actual running parameters (in particular the detuning from the optical resonance).

Less significant changes over the earlier work included efforts to improve the vibration isolation as well as a change increasing the repetition rate of the experiment from 1 Hz to 5 Hz. A new platform supported the mirror just below the lower window. The mirror was attached to a massive base suspended from the ceiling by surgical tubing. An accelerometer was mounted on the platform to monitor its motion. The 5 Hz repetition rate improved our signal to noise by permitting more rapid averaging over shot-to-shot noise sources.

In section 5.2.1 we describe in detail the experimental method for obtaining the Raman beams. Section 5.2.2 focusses on the major noise source of the measurement, mechanical vibrations, and our efforts to overcome it. Section 5.2.3 relates the importance of magnetic fields in the experiment, and serves as a reminder that sodium is not the 3-level atom shown in Fig. 4.1.

5.2.1 Raman Beams

Light from a second dye laser was switched through an electro-optic modulator by an acousto-optic modulator located at the output of the laser (see Fig. 5.7). The frequency modulated light was then coupled into an ~ 2 m long polarization preserving
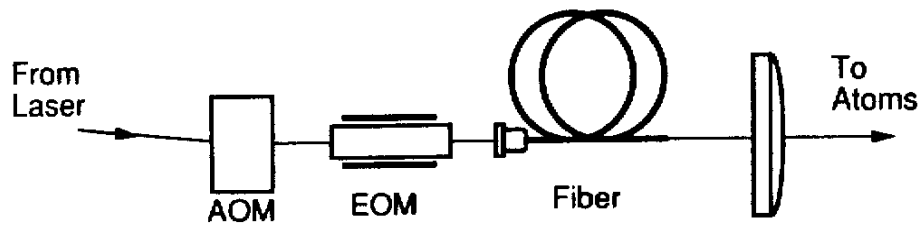

Fig. 5.7: Optics used to generate the Raman beams

optical fiber. The output beam from the fiber was expanded and collimated before being sent into the vacuum can through a window mounted on its top flange. The light exited the vacuum chamber through another window located on the bottom of the can. The beam was then retro-reflected back into the vacuum by a mirror mounted on a stable 'inertial' reference frame just outside the lower window.

The fiber optic isolated the interferometer beams from pointing instabilities in the dye laser and also spatially filtered the beams. Pointing instabilities and wavefront distortion in the Raman beams tend to destroy fringe contrast as well as randomize the interferometer phase shifts. After the fiber, the beam was expanded to an ~ 4 cm $1/e^2$ diameter collimated beam. With this beam waist the power varied by 12% over the central 1 cm diameter of the beam. The collimation was better than 250 μrad.

The Raman beat frequency was determined directly by the rf frequency used to drive the electro-optic modulator. For each Raman pulse the acousto-optic modulator was switched on, sending light through the electro-optic modulator and then fiber. Simultaneously the appropriate rf frequency was switched into the electro-optic modulator. The acousto-optic modulator's switching time was ~ 100 nsec and its on/off extinction ratio was better than 10^{-4}. The rf power for the electro-optic modulator was switched on in $\sim 1\mu$sec.

The effective Rabi frequency of the Raman transition is determined by the power output of the interferometer laser, the detuning of this laser from the optical transition, and the modulation index of the electro-optic modulator. Typically ~ 20 μsec were required to drive a π pulse when the laser carrier frequency was detuned 2.5 GHz from the $F=2$, $3S_{1/2} \rightarrow 3P_{3/2}$ resonance. Circularly polarized light was used to drive the $m_f=0$ $\rightarrow m_f=0$ magnetic field insensitive transition.

The detuning operating point was chosen to enhance the Rabi frequency as much as possible without sacrificing performance with an excessive background due to spontaneous emission. The simple scaling argument presented at the end of section 5.1.3 did not account for spurious spectral components in the light field. The choice of a suitable operating point was complicated by the higher order sidebands from the electro-optic modulator: one had to step carefully to avoid an accidental resonance with a high

order sideband. For example, a detuning of -1.7 GHz put the +1 sideband directly on resonance! At -2.5 GHz, the +1 and +2 order sidebands bracketed the resonance by ± 800 MHz. Experimentally, detuning the carrier at $|\Delta| < 1$ GHz produced unacceptably high background levels.

After fixing Δ, the Rabi pulse temporal widths corresponding to π or $\pi/2$ pulses were set by scanning the pulse width of a single Raman pulse. In the absence of spontaneous emission, the profile shown in Fig. 5.5 is expected. Spontaneous emission, however, produces a background which grows linearly with pulse width, which can be measured by detuning the Raman beams from the Raman resonance condition. The π pulse time corresponded to the first maximum in the scan. A pulse width scan also served as a simple diagnostic for alignment/timing errors which resulted in $m_f \neq 0$ atoms being detected as well as $m_f = 0$ atoms (see section 5.2.3 below).

As discussed in section 5.1, the change in the Raman resonance frequency due to the atom's acceleration was much larger than the effective Rabi frequency of the transition. In order to maintain the resonance condition the frequency of the rf sideband was switched from one pulse to the next by an amount which nearly compensated for the atom's acceleration. The rf sideband frequency was generated by mixing the output of one of three low frequency synthesizers with a stable high frequency synthesizer (Hewlett-Packard 8665A) to get the required ~ 1.7 GHz Raman frequency as shown in Fig. 5.8. A notch filter passed the sum frequency to a power amplifier which drove the electro-optic modulator. The sideband frequency was switched by multiplexing between the three low frequency synthesizers. The reference frequency for all synthesizers was derived from a SRS FS 700 LORAN-C receiver, which had a short term frequency stability of $\sim 5 \times 10^{11}$. The relative phase noise of the synthesizers was monitored by forming the sum $\phi_1 - 2\phi_2 + \phi_3$ ($\phi_i = \Delta\omega_i t + \phi_i^0$ the phase of the ith synthesizer) with an appropriate combination of rf mixers and combiners (see Fig. 5.8). The peak-to-peak excursions in phase were measured to be less than 20°. We were able to scan the phase of the final $\pi/2$ pulse by incrementing the phase of the Hewlett-Packard 3325B synthesizer used to generate this pulse.

The delay time between each Raman pulse was set by a quartz oscillator driven
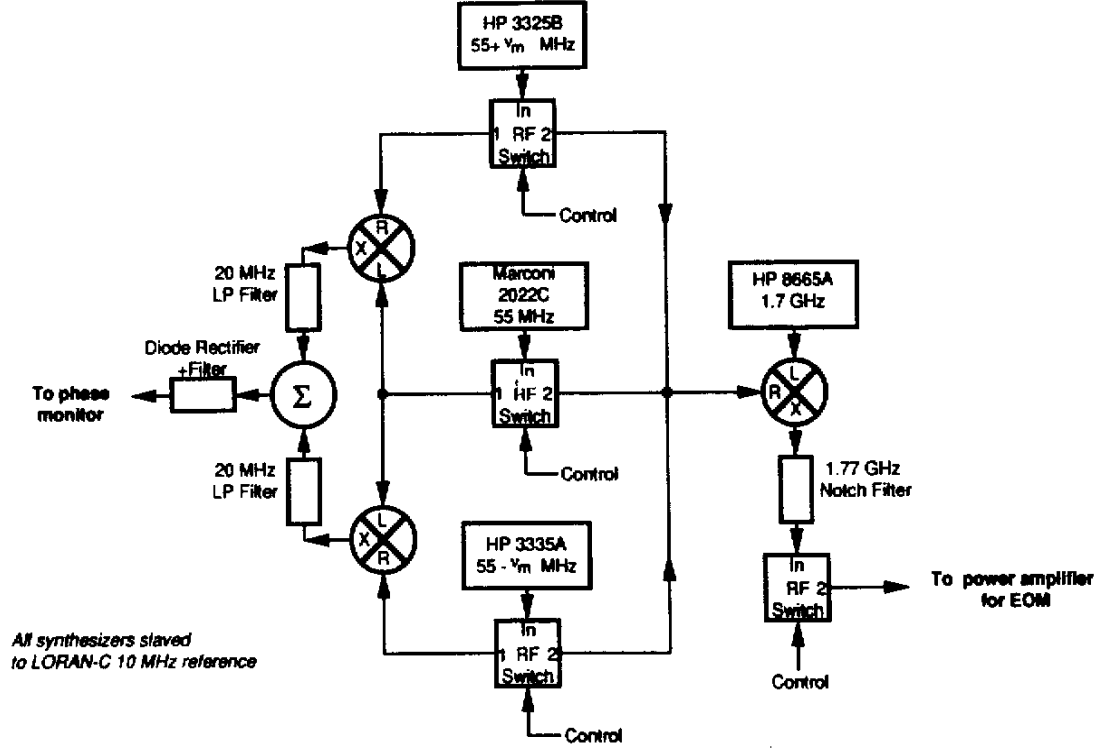
Fig. 5.8: Schematic of rf electronics used to drive the EOM for the Raman beams

pulse generator. The requirements on timing jitter for this delay are obtained by considering Eqs. (4.6) and Eqs. (5.3) in light of unequal intervals between pulses. The result is that contrast is lost when $\Omega_{eff}\delta t \sim 2\pi$, where $\delta t = |(t_2-t_1) - (t_2-t_3)|$ (see section 5.1). In this experiment, $\Omega_{eff}\delta t \ll 2\pi$.

The frequencies of the Raman pulses depended on the times t_i when the Raman beams were pulsed on, the location of the detection region, and of course gravity. The spatial extent of the detection region was constrained vertically to minimize background counts from the $m_f \neq 0$ atoms (see section 5.2.3 below). This imposed a ballistic

97

constraint on the trajectories of the $m_f=0$ atoms. Our method was to first fix a detection time, then ensure that the $m_f=0$ atoms had the appropriate initial velocity to place them in the detection region at the detection time. There were two steps in preparing the velocity of the atoms. First, the moving molasses launch velocity was optimized to maximize the number of atoms in the detection region at the detection time (due to the large initial velocity spread of the atoms this was a fairly course adjustment). Next, the Raman beams were pulsed on for a single pulse at the time of the π pulse (t_2) for a time roughly corresponding to the time required to drive a π pulse (precise determination of the π pulse time, as described above, was done *after* choosing the Raman frequencies). The Raman frequency was then scanned to find the Raman frequency which addressed the velocity class of atoms which were in the detection region at the detection time. The time T between interferometer pulses was then used to determine the frequencies of the first $\pi/2$ and final $\pi/2$ pulse by the relation $\omega_m = (k_1-k_2)gT$. To see interference, $|\omega_m - 2kgT| < \Omega_r$. After interference was established, ω_m could be changed to optimize the signal.

5.2.2 *Mechanical vibration*

Since all frequency components of the Raman beams follow the same optical path into the vacuum can, the Raman frequency is insensitive to mechanical vibrations of the optical elements used to steer the beams into the can. In the gravimeter configuration, vibrating elements Doppler shifted the optical frequency by approximately one kHz. However, when all the frequencies co-propagate, these Doppler shifts are nearly equal for each component. Thus the net shift to the Raman beat frequency was negligible when the beams were being directed into the vacuum can (on the order of 1 kHz x $k_{rf}/k_1 \sim$ 10^{-3} Hz). The shift in the Raman frequency due to the ~2 MHz linewidth of the lasers was negligibly small. On the other hand, vibrations of the retro-reflecting mirror beneath the vacuum can will directly Doppler shift the Raman frequency. Here the two frequency components no longer co-propagate: the Raman field driving the atom is comprised of one frequency component which has not reflected from this mirror and another which has. The Doppler shift of one beam is no longer canceled by another shift

of nearly equal magnitude in the other beam. The Doppler shift due to the random motion of this mirror, in turn, randomizes the phase of the Raman beams from launch to launch.

From another point of view, the retro-reflecting mirror is providing an inertial reference for the measurement of the acceleration of the atom. It is, therefore, essential that this mirror not vibrate (ie. accelerate). We passively vibrationally isolated the mirror by mounting it on a platform which was suspended from the ceiling of our lab with surgical tubing. A Kinemetrics SS-1 seismometer[98] was used to characterize the platform's motion. The platform's natural oscillation frequency was ~0.5 Hz. At frequencies above 3 Hz the peak-to-peak displacement of the position of the platform parallel to the Raman beams was less than 20 nm. Since the amplitude of these high frequency vibrations was much less than the effective wavelength of the Raman light (295 nm) they were not large enough to wash out interference fringes. The dominant platform vibrations were large amplitude (~2.5 μm) oscillations near the platform's resonance frequency, 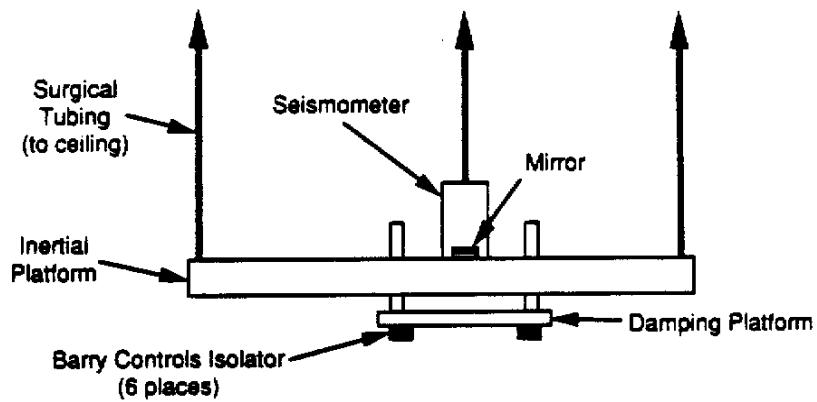which corresponded to platform accelerations of ~2.5×10^{-6} g. Independent measurements of the floor vibration spectrum at various locations throughout the building demonstrated strong peaks in the 0.5-1.0 Hz band. At longer drift times, these vibrations destroyed fringe visibility. Fig. 5.9 illustrates the design of the vibration isolation stage. The geometry was limited by the existing apparatus and availability of anchor points on the ceiling for the surgical tubing supports. Pulleys allowed the tension in the surgical tubing support strands to be easily adjusted, which in turn, provided a means for a course levelling of the platform. Fine tuning of the platform levelling was accomplished by stacking appropriately placed shim weights on the platform. Damping was supplied by dabs of Dow Corning high vacuum grease which weakly linked the platform to semi-rigid posts in the three locations indicated in Fig. 5.9. The posts were themselves mounted on stages vibrationally isolated from the floor with properly loaded Barry-Controls SLM-1A vibration isolation supports. This isolated the damping posts from high frequency noise sources produced by nearby mechanical pumps and compressors. The seismometer was rigidly attached to the platform to monitor the platform's motion during data acquisition. The entire system, including the surgical

Top View

Hi-Vac
Grease
(3 places)

Seismometer

Damping Post
(3 places)

Intertial Platform

Damping
Platforms

Mirror

Surgical
Tubing
(3 places)

7'

6'

Side View

Surgical
Tubing
(to ceiling)

Seismometer

Mirror

Inertial
Platform

Damping Platform

Barry Controls Isolator
(6 places)
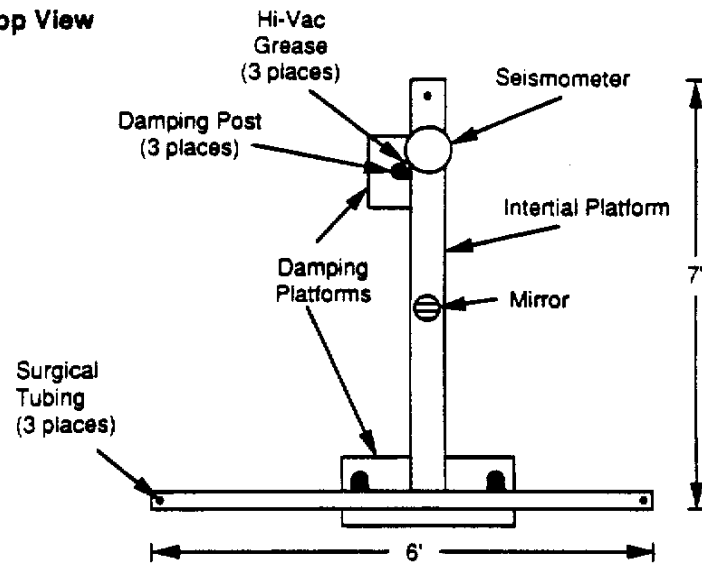
Not shown:
Air current shield

Fig. 5.9: Vibration isolation system for the retro-reflecting mirror

100

tubing supports, was enclosed in a cardboard shell which served to isolate it from room air currents. The coupling strength for the damping was experimentally tweaked by varying the amount of Hi-Vac grease and proximity of the damping posts to the platform.

The Kinemetrics SS-1 seismometer had a 370 V/(m/sec) factory quoted response. The response was independently measured by comparing the SS-1 response to that of a previous calibrated Mark Products L-25A-1 geophone (8Hz natural resonance, 110Ω coil resistance) under the same excitation conditions. The measured and quoted responses agreed to within 30%. The geophone was calibrated by mounting the sensor on a PZT driven stage. The response of the sensor was measured as a function of the driving frequency/amplitude of the PZT stage.

5.2.3 *Magnetic fields*

Whereas vibrations and wavefront quality can destroy fringe visibility by randomizing the phase of the Raman field, inhomogeneous magnetic fields can potentially destroy fringe contrast during the atom's free flight between Raman pulses. To minimize the effects of magnetic field variations, we used the magnetic field insensitive $m_f=0 \rightarrow m_f=0$ transitions. Helmholtz coils were used to apply a bias field parallel to the propagation axis of the Raman beams. The bias field was needed to Zeeman shift the field sensitive transitions out of resonance with the Raman beams. Off-resonant excitation of magnetic field sensitive transitions produces unwanted background counts. To avoid off-resonant excitation the Zeeman shifts between field sensitive and field insensitive transitions must be greater than the frequency linewidth of an individual Raman pulse. The $m_f=\pm 1 \rightarrow m_f=\pm 1$ field sensitive transitions Zeeman shift by 1.4 MHz/Gauss. For a $10\mu sec$ $\pi/2$ pulse, the transition linewidth is ~ 100 kHz, so a bias field of at least (100 kHz)/(1.4 MHz/Gauss) ~ 80 mGauss is needed. Interference contrast was observed to be insensitive to bias field values over a range from 100 mGauss to 300 mGauss.

The above constraint on the size of the bias field ensures that the probability for excitation of $m_f \neq 0$ atoms having the same velocity as the $m_f=0$ atoms is small. However, if the magnetic field shifts are less than the Doppler width of the source, the

$m_f \neq 0$ transitions are still excited in velocity classes which differ from the velocity class driven by the $m_f = 0$ transitions. If these atoms were detected along with the $m_f = 0$ atoms, they would lead to a large, unwanted background. We discriminated $m_f \neq 0$ atoms
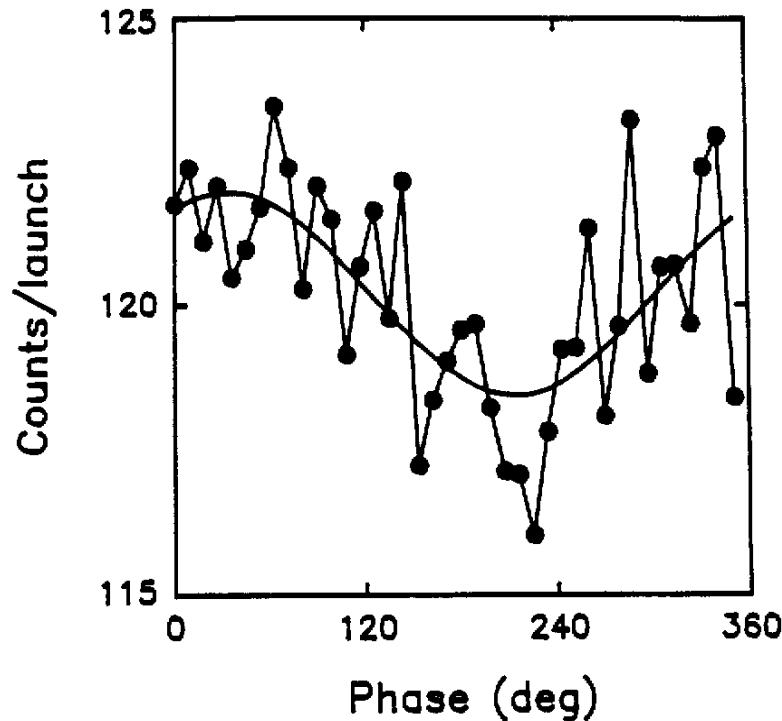
Fig. 5.11: Counts vs. phase of final $\pi/2$ pulse for T = 100 msec.

with the square of the drift time). Figure 5.11 shows data for T=100 msec. At T=100 msec between pulses the estimated phase noise from platform vibrations was ± 0.4 cycles. Due to these large phase variations, visibility was degraded to a few percent, which is consistent with simulations of the signal. Each data point is an average of 22 launches, with a launch rate of 1 launch/sec. Even with the poor visibility, the sensitivity to changes in g was $\Delta g/g = 7 \times 10^8$. In order to accommodate the longer drift times, the atoms were detected on their second pass through the detection region at t = 400 msec. The Raman pulse times were 120 msec, 220 msec and 330 msec, with $\omega_0 = 1770.44$ MHz and $\omega_m = 3.366$ MHz.

Other sources of noise included fluctuations in the number of trapped atoms

sources on the interference signal was characterized, in part, by driving the hyperfine "clock" transition with two Doppler insensitive $\pi/2$ pulses. Counts due to population of the $F=2$ level from spontaneous emission from the $3P_{3/2}$ state produced a background count rate which was 20% of the peak rate. This rate was measured by detecting the number of atoms in the $F=2$ state when the Raman frequency was tuned far (1 MHz) off resonance, and was subtracted out before estimating fringe visibility.

Scanning the phase of the final $\pi/2$ pulse was a convenient way to characterize the sensitivity of the interferometer. It does not provide enough information alone, however, to give an absolute value for g. In our earlier work, we implemented a data collection method which can, in the absence of systematic perturbations (see below), be used to derive an absolute measure of g. In this method, we scanned the frequency ω_m rather than the final phase. The theoretical response is given by $\Delta\phi = -(k_1-k_2)gT^2+2\omega_mT$, and with T fixed, produces a sinusoidal dependence of counts on ω_m. An absolute value for g can be inferred from the relation

$$\frac{\left(\omega_m^{min}\right)^2}{2kg} = 2\pi n \qquad (n\ an\ integer) \quad , \tag{5.10}$$

which is obtained by substituting $\omega_m \sim (k_1-k_2)gT$ into the expression for $\Delta\phi$ (ω_m^{min} is the frequency corresponding to a fringe minimum). Fig. 5.12 shows a scan of ω_m vs. counts. For this data the delay time between pulses was $T=10$ msec and a least squares fit to the data give an uncertainty in g of 3×10^{-6}. The initial phase of the synthesizers $\Delta\phi^0 = \phi_1^0-2\phi_2^0+\phi_3^0$ had to be reset to 0 after each frequency step for ω_m. Perhaps a more intuitive way of measuring g is to use a phase continuous frequency chirp to control the frequency (phase) of the Raman beams (see section 5.1.2). The experimental method would entail changing the chirp rate of the sweep generator until the phase evolution of the generator exactly balanced that of the atom's Doppler shift of the Raman field, so that as the drift time T was changed, no change in the number of atoms excited to the $F=2$ state would be observed. We implemented this scheme in our earlier measurements and found that the phase stability of the sweep for the HP8665A sweep generator was
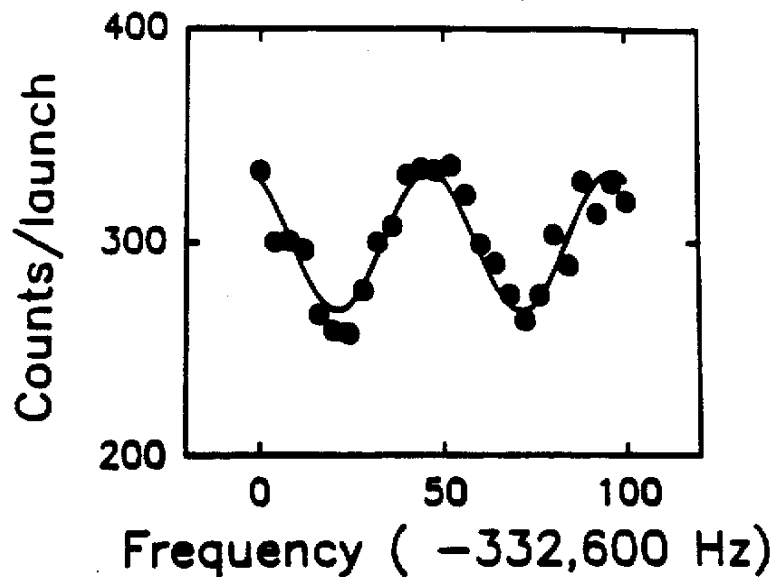
Fig. 5.12: Counts vs. frequency increment ω_m

unreliable for drift times greater than 10 msec. Fig. 5.13 shows an example of this technique. For this data, the phase of the chirp generator nearly canceled that of gravity, so that as the delay time T was scanned, a slowly evolving quadratic phase shift was observed. With the recent commercial availability of affordable and useable direct digital synthesis waveform generators, this method deserves re-evaluation.
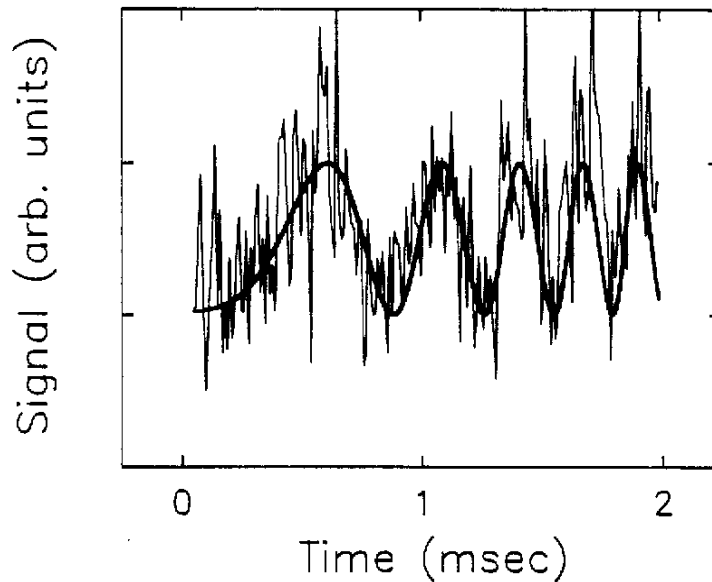
Fig. 5.13: Counts vs. drift time T for a fixed chirp rate

5.4 DISCUSSION

The ultimate resolution and accuracy of the accelerometer hinges on (1) sources of short term fluctuations and (2) long term stability of systematic offsets.

5.4.1 *Short term stability*

Our present short term sensitivity to changes in g is limited by vibrations, fluctuations in the number of trapped atoms and fluctuations in detection efficiency. Neither of these is an insurmountable obstacle towards achieving better resolution.

Noise arising from vibrations can be significantly reduced with an active isolation system: state-of-the-art "super-springs" routinely achieve rms residual accelerations of 10^{-9} g.[25,26] This improvement should enable the use of drift times ~0.3 sec. For T=300

107

msec, a change in g by 3 parts in 10^7 leads to a phase shift $\Delta\phi$ of one cycle.

Noise sources associated with fluctuations in numbers of trapped atoms or from fluctuations in detection efficiency can be reduced by techniques now being used for atomic-fountain-based atomic clocks.[13,99] Fluctuations in detection efficiency and numbers of trapped atoms are minimized by 'normalized' detection techniques, where the number of atoms in the $|1\rangle$ state and $|2\rangle$ state are detected simultaneously. Recent experiments using this scheme have reported performances within two orders of magnitude of the shot-noise limit, and it is anticipated that, with further improvements, performance will approach the shot-noise limit.

The number of atoms contributing to the interference can be significantly improved by using cesium, rather than sodium atoms. The rms velocity spread of a sample of laser cooled cesium atoms is ~ 2 cm/sec. Thus, fewer atoms will be lost due to ballistic spreading of the sample during the ~ 600 msec flight time of the atoms. A 1 mm diameter trap (larger traps may lead to systematic shifts, see below) contains nearly 10^8 atoms. Assuming 10% of the initially trapped atoms ultimately contribute to the detected interference signal, the anticipated count rate is $\sim 10^7$ atoms/sec. If the measurement were shot-noise limited, these statistics would enable a fringe to be split by better than 1 part in 10^3 after 1 second.

Based on the above estimates, it seems reasonable to conclude that the short term resolution of the instrument will probably be limited by residual vibrations of the platform, and not atom count statistics. Taking residual platform vibrations as a random noise source, we project a short term stability of $\sim 10^{-9}\,g/\tau^{1/2}$ (τ the measurement time in seconds). If the measurement were shot-noise limited, the estimated resolution is $\sim 10^{-10}\,g/\tau^{1/2}$.

5.4.2 Systematic Uncertainties

Other uncertainties which will limit the resolution of a measurement of g include those arising from the initial spread in position and velocity of the atoms, from spurious electro-magnetic forces on the atoms, and from imperfections in the light beams. Coriolis forces and gravitation gradients produce inertial forces which are velocity and

position dependent. Magnetic field gradients are the dominant electro-magnetic perturbation. Finally, AC Stark shifts, Raman beam alignment, laser frequency stability and multiple sideband interference are sources of laser dependent phase shifts. Shot-to-shot variations due to the above effects can likely be made less than those due to vibration of the inertial reference. However, slow drifts in the average value of a systematic offset will limit the accelerometer's long term resolution.

Coriolis forces may lead to systematic phase shifts for atoms with velocity components orthogonal to the propagation axis of the light. For these atoms, the Coriolis term $2\Omega_{earth}xv$ may have a component parallel to the light's propagation axis. For the T=50 msec data, the transverse velocity spread was limited to $\Delta v_{transverse} < 10$ cm/sec by the spatial extent of the detection region. Taking $2\Omega_{earth}xv$ to lie parallel to k, the *worst case* acceleration is $\sim 10^{-6}$ g. Working with laser cooled cesium atoms reduces this limit by an order of magnitude. Furthermore, trajectories can be transversely collimated (at the expense of lowering the count rate) to further minimize this effect.

Alternatively, by changing the experimental geometry, the interferometer can be used to measure rotations with high sensitivity. In this case, the orientation of the Raman beams is taken perpendicular to the atoms' mean velocity in order to maximize sensitivity to rotations (since Ωxv is perpendicular to v). Replacing the acceleration due to gravity with the Coriolis acceleration $2\Omega xv$ in Eq. (5.6) gives $\Delta\phi_{Coriolis} = 2(k_1-k_2) \cdot (\Omega xv)T^2$ which is equivalent to the standard expression for the Sagnac phase for matter waves.[89] Taking $v \sim 1$ m/sec and T=50 msec yields a sensitivity to rotations of $\Delta\Omega/\Omega_{earth} \sim 2x10^{-3}$ if a fringe can be split by 3 parts in 10^3 (as demonstrated for the data of Fig. 5.10).

The gravitational gradient due to the $1/R^2$ dependence of g on the distance R from the center of the earth is $3x10^{-9}$ g/cm. Thus, the mean trajectory of the atoms (defined by their mean initial position and velocity) should be stable to better than 1 mm for accuracies of 10^{-10} g. This sensitivity will allow one to measure changes in height of land and sea levels with a 1 mm resolution.

Magnetic field gradients exert forces on an atom, which, in general, depend on the internal state of the atom. The resulting phase shifts are estimated from Eqs. (5.7)

109

and (5.8) by calculating the classical trajectories for the atom under the influence of the perturbing field. In the limit where the recoil velocity is much smaller than the mean velocity of the atom (ie. the deBroglie wavelength of the wavepacket is much smaller than the wavelength of the Raman light), the dominant contribution comes from the shift which accrues during the atom's free evolution. The extra free evolution phase is $\Delta\phi_f = \int_\Gamma \Delta k_a \cdot dx - \Delta\omega_a dt$, where $\hbar\Delta k_a$ and $\hbar\Delta\omega_a$ are the change in the momentum and total energy of the atom due to the presence of the field gradient (see Eq. 5.8). For a static magnetic field with weak gradients, the total energy of the atom is conserved, so $\Delta\omega_a = 0$. Then $\Delta\phi_f \approx \int_\Gamma k \cdot v dt \approx -\int_\Gamma \Delta\omega_{int}(t) dt$, where $\Delta\omega_{int}$ is the Zeeman shift of the internal state of the atom. For an $m_f = 0 \rightarrow m_f = 0$ groundstate hyperfine transition, the shift is approximately

$$\Delta\phi_f \approx 2\alpha v B \frac{dB}{dx} T^2 , \qquad (5.11)$$

where the second order Zeeman shift of the transition is αB^2, B is the magnitude the magnetic field at the first $\pi/2$ pulse, and dB/dx the size of the field gradient. In the above expression we have neglected the effects of gravity on the atom's trajectory and taken the atom's initial velocity v parallel to the field gradient. For sodium ($\alpha = 2.21$ mHz/mGauss^2), a 1 mG/cm gradient in a 100 mG bias field leads to a shift of ~ 0.2 cycles when T = 100 msec and v = 1 m/sec. These shifts can be significantly reduced by lowing the external bias field. Since cesium atoms can be initially hyperfine pumped to an $m_f = 0$ state, off-resonant excitation of other levels is not a problem. Therefore, only a small bias field is needed to define a quantization axis.

AC Stark shifts change the phase of the atomic coherence when the Raman beams are pulsed on. When the pulse areas for the interferometer sequence are uniformly $\pi/2$, π and $\pi/2$ the net contribution to $\Delta\phi$ is zero. The AC Stark effect can lead to uncontrolled phase shifts when the intensity of the laser beam varies over the spatial extent of the source, or when the intensity varies in time. For this experiment the AC Stark shift was measured to be ~ 12 kHz, which corresponds to about 0.25 cycles of phase shift for a π pulse. The dye laser intensity fluctuations of $\sim 5\%$ then lead to

random phase shifts of < 0.025 cycles. These were also present when the transition was driven in the Doppler free $\pi/2$-$\pi/2$ configuration, and so could be characterized independently from the vibrationally induced phase shifts. Shifts arising from spatial variations can be minimized by using large Raman beams and a relatively small source of atoms, so that the atoms sample only the central region of a large Gaussian beam. Finally, it may be possible to cancel the AC Stark shifts arising from the Raman beams with those from extra, non-resonant, spectator beams of appropriate detuning.

The gravitational phase shift is proportional to $(k_1$-$k_2) \cdot g$, thus any offset or variation in either the direction or magnitude of k_1 or k_2 will produce unwanted phase shifts. In the current experiment, the Raman beams were aligned parallel to g to within 2 mrad. Since the systematic error scales with the square of the alignment errors, in future experiments tolerances of $\sim 10^{-5}$ rad will be required for accuracies of $\sim 10^{-10}$ g. The optical frequency of the laser beams must be stable to approximately the same level as the desired uncertainty in the measurement, and must be known to that degree if an absolute calibration is desired.

The phase-modulation scheme we used to drive the Raman transitions has the undesirable sideband interference effects alluded to in section 5.1.3. These lead to phase shifts which are difficult to characterize. A better scheme is available for cesium atoms: phase-lock the output of two diode lasers to the Raman frequency.[100] The phase-locked beams can be overlapped, then coupled into the optical fiber, as in Fig. 5.7.

5.5 FUTURE PROSPECTS

We have demonstrated a sensitivity to accelerations of $\Delta g/g = 3 \times 10^{-8}$ for T=50 msec drift times and seen weak interference for T=100 msec drift times. Working with cesium atoms, rather than sodium, and implementing an active vibration isolation system, we hope to achieve an absolute sensitivity of $\Delta g/g < 10^{-10}$. At this accuracy, a measurement of the acceleration due to gravity will represent an improvement of 5 orders of magnitude over existing measurements on atomic mass scale particles.[101] This also will exceed the current resolution of state-of-the-art 'falling corner cube' gravimeters by more than an order of magnitude.[102] Furthermore, with recent advances in diode laser

111

technology[103] and trapping of atoms in vapor cells,[104] it should be possible to engineer a portable system for geophysical applications.

We note that with wavepacket separations in excess of a mm, the two arms of the interferometer should be spatially resolved. The arms are resolvable when the ballistic spreading of the wavepacket is less than the recoil velocity of the Raman transition and when the initial size of the source of atoms is less than the single atom wavepacket separation. The ballistic spread of atoms contributing to the interference is set by the Rabi frequency. For the Rabi frequency of this experiment, the velocity spread is 1.5 cm/sec. The recoil velocity, on the other hand, is 6 cm/sec, and the source size for the T=50 msec data was ~1.5 mm, significantly less than the wavepacket separation.

Finally, the Doppler sensitivity, and hence recoil kick, of the stimulated Raman transitions can be enhanced by replacing single Raman pulses with trains of pulses of alternating spatial orientation. For example, the Doppler sensitivity of a π pulse can be leveraged up by a factor of two by applying a π pulse with ν_1 propagating in the +x direction and ν_2 in -x direction, and then immediately thereafter applying a π pulse with ν_1 propagating in the -x direction and ν_2 in the +x direction. A factor of n enhancement is obtained with a sequence of n pulses, with the propagation axes of the Raman components of each successive pulse reversed with respect to those of the previous pulse. An enhanced $\pi/2$ pulse would be formed in a manner identical to that of a π pulse, with the first pulse in the sequence being a $\pi/2$ pulse rather than a π pulse. Successful application of this technique will require fine control of the pulse area associated with each individual pulse in order to maintain good fringe contrast. This necessitates that the Raman laser intensity be temporally stable and that the beam profile be uniform over the spatial extent of the atomic source. Given current operating parameters, pulse trains at least as long as 10, and perhaps as long as 100, pulses seem feasible. Viewing n Raman pulse sequences as effective phase gratings of periodicity $\lambda_{eff} \sim \lambda/2n$ implies that grating periodicities of $\lambda_{eff} < 10$ nm may be obtainable.

SECTION 6

CONCLUSION

Velocity sensitive stimulated Raman transitions have been used to demonstrate a light-pulse atom interferometer with laser cooled atoms. Configuring the interferometer as an accelerometer, we have measured the acceleration due to gravity of an atom with a resolution of 3 parts in 10^8. We have also demonstrated interference for wavepacket separations as large as 6 mm. Our current resolution is limited by vibration of our inertial reference point: at least two orders of magnitude improvement in performance is expected when it is replaced with a state-of-the-art active vibration isolation system. An absolute measurement of g at this level will represent a 5 order of magnitude improvement over previous measurements of g on atomic scale particles. Wavepacket separations of more than 2 cm seem feasible.

In the course of this work we have developed several new atom manipulation techniques which have important applications in their own right: atomic fountains, "moving molasses" and velocity sensitive stimulated Raman transitions. By launching atoms in a moving molasses on ballistic trajectories, we have demonstrated a high density atomic fountain where laser cooled atoms are confined by gravity for time scales on the order of a second. Velocity sensitive Raman transitions have been used to prepare ensembles of atoms with one-dimensional effective temperatures of 24 pK. We have also used the transitions to measure the temperature of polarization gradient molasses.

Moving molasses atomic fountains may prove to be the best source for the next generation of atomic clocks. They also provide ideal sources for experiments such as ultra-cold atom collision studies. We have already made a preliminary measurement of the atom-surface Casimir interaction. Future collision studies will also benefit from the velocity selection techniques demonstrated here for the first time. For example, with the enhanced resolution afforded by velocity sensitive stimulated Raman transitions, it appears possible to map out the strength of the Casimir surface potential as a function

of the atom's distance from the surface. Velocity sensitive Raman transitions are currently being used in conjunction with optical pumping techniques to cool atoms well below the photon recoil limit, and may provide access to phase space densities high enough to see quantum many-body effects.

APPENDIX A

SODIUM MATRIX ELEMENTS

Table A.I lists the relative oscillator strengths $\langle d^2 \rangle$ and matrix elements $\langle d \rangle$ for the sodium $3S_{1/2} \to 3P_{1/2}, 3P_{3/2}$ hyperfine transitions. The table was generated using the standard Racah algebra formulae summarized below.[105] 3-j and 6-j symbols were evaluated numerically with Fortran code written by Tamura.[106]

We wish to evaluate the matrix elements $\langle F,m_f | C^{(1)}_q | F',m_{f'} \rangle$, where $C^{(1)}_q$ is the Racah tensor for a spin 1 particle (eg. photon). In particular

$$C^{(1)}_0 = \cos(\theta)$$

$$C^{(1)}_{\pm 1} = \mp \frac{\sin(\theta)}{\sqrt{2}} e^{\pm i\phi}$$

(A.1)

where θ and ϕ are the angular coordinates for the radial vector. The total angular momentum $F = J + I$, where I is the nuclear angular momentum and $J = L + S$ the sum of the orbital angular momentum L and spin angular momentum S. For the sodium $3S \to 3P$ transitions, $I = 3/2$, $S = 1/2$ and $L = 0,1$.

First, the Zeeman sub-levels are decoupled with the Wigner-Eckart theorem:

$$\langle F,m_f | C^{(1)}_q | F',m_{f'} \rangle = (-1)^{F-m_f} \begin{pmatrix} F' & 1 & F \\ -m_f & q & m_f \end{pmatrix} \langle F \| C^{(1)} \| F' \rangle$$

(A.2)

where ( ) is the 3-j symbol and $\langle F \| C^{(1)} \| F' \rangle$ is the reduced matrix element. Next, the nuclear angular momentum I is decoupled from the total angular momentum F:

$$\langle F \| C^{(1)} \| F' \rangle =$$

$$\delta_{II'} \sqrt{2F+1} \sqrt{2F'+1} (-1)^{J+I+F'+1} \begin{Bmatrix} I & J & F \\ 1 & F' & J' \end{Bmatrix} \langle J \| C^{(1)} \| J' \rangle$$

(A.3)

where {} is the 6-j symbol. The spin angular momentum S is subsequently decoupled

115

from **J**:

$$\langle J \| C^{(1)} \| J' \rangle =$$

$$\delta_{SS'} \sqrt{2J+1} \sqrt{2J'+1} \, (-1)^{L+S+J'+1} \begin{Bmatrix} S & L & J \\ 1 & J' & L' \end{Bmatrix} \langle L \| C^{(1)} \| L' \rangle \qquad \text{(A.4)}$$

Finally, the reduced matrix elements are given by

$$\langle L \| C^{(1)} \| L' \rangle = (-1)^{L_> - L} \sqrt{L_>} \qquad \text{(A.5)}$$

where $L_>$ is the larger of L and L', and L = L'$\pm$1.

Nuclear spin = 1.5
Orbital spin = .00   1.0
J spin = .50   1.5

mf	mf'	<d>	<d**2>	<d**-2>
F = 1.0	F' = .00			
-1.0	.00	-.3333333	.1111111	9.000000
.00	.00	-.3333333	.1111111	9.000000
1.0	.00	-.3333333	.1111111	9.000000
F = 1.0	F' = 1.0			
-1.0	-1.0	.3726780	.1388889	7.200000
-1.0	.00	-.3726780	.1388889	7.200000
.00	-1.0	.3726780	.1388889	7.200000
.00	1.0	-.3726780	.1388889	7.200000
1.0	.00	.3726780	.1388889	7.200000
1.0	1.0	-.3726780	.1388889	7.200000
F = 1.0	F' = 2.0			
-1.0	-2.0	-.4082483	.1666667	6.000000
-1.0	-1.0	.2886751	.8333334E-01	12.00000
-1.0	.00	-.1666667	.2777778E-01	36.00000
.00	-1.0	-.2886751	.8333334E-01	12.00000
.00	.00	.3333333	.1111111	9.000000
.00	1.0	-.2886751	.8333334E-01	12.00000
1.0	.00	.1666667	.2777778E-01	36.00000
1.0	1.0	.2886751	.8333334E-01	12.00000
1.0	2.0	-.4082483	.1666667	6.000000
F = 2.0	F' = 1.0			
-2.0	-1.0	-.1825742	.3333334E-01	30.00000
-1.0	-1.0	-.1290994	.1666667E-01	60.00000
-1.0	.00	-.1290994	.1666667E-01	60.00000
.00	-1.0	-.7453560E-01	.5555556E-02	180.0000
.00	.00	-.1490712	.2222222E-01	45.00000
.00	1.0	-.7453560E-01	.5555556E-02	180.0000
1.0	.00	-.1290994	.1666667E-01	60.00000
1.0	1.0	-.1290994	.1666667E-01	60.00000
2.0	1.0	-.1825742	.3333334E-01	30.00000
F = 2.0	F' = 2.0			
-2.0	-2.0	.3333333	.1111111	9.000000
-2.0	-1.0	-.2357023	.5555556E-01	18.00000
-1.0	-2.0	.2357023	.5555556E-01	18.00000
-1.0	-1.0	.1666667	.2777778E-01	36.00000
-1.0	.00	-.2886751	.8333334E-01	12.00000
.00	-1.0	.2886751	.8333334E-01	12.00000
.00	1.0	-.2886751	.8333334E-01	12.00000
1.0	.00	.2886751	.8333334E-01	12.00000
1.0	1.0	-.1666667	.2777778E-01	36.00000
1.0	2.0	-.2357023	.5555556E-01	18.00000
2.0	1.0	.2357023	.5555556E-01	18.00000
2.0	2.0	-.3333333	.1111111	9.000000
F = 2.0	F' = 3.0			
-2.0	-3.0	-.5773503	.3333333	3.000000
-2.0	-2.0	.3333333	.1111111	9.000000
-2.0	-1.0	-.1490712	.2222222E-01	45.00000
-1.0	-2.0	-.4714045	.2222222	4.500000
-1.0	-1.0	.4216370	.1777778	5.625000
-1.0	.00	-.2581989	.6666667E-01	15.00000
.00	-1.0	-.3651484	.1333333	7.500000
.00	.00	.4472136	.2000000	5.000000
.00	1.0	-.3651484	.1333333	7.500000
1.0	.00	-.2581989	.6666667E-01	15.00000
1.0	1.0	.4216370	.1777778	5.625000
1.0	2.0	-.4714045	.2222222	4.500000
2.0	1.0	-.1490712	.2222222E-01	45.00000
2.0	2.0	.3333333	.1111111	9.000000
2.0	3.0	-.5773503	.3333333	3.000000

Nuclear spin = 1.5
Orbital spin = .00   1.0
J spin = .50   .50

mf	mf'	<d>	<d**2>	<d**-2>
F = 1.0	F' = 1.0			
-1.0	-1.0	-.1666667	.2777778E-01	36.00000
-1.0	.00	.1666667	.2777778E-01	36.00000
.00	-1.0	-.1666667	.2777778E-01	36.00000
.00	1.0	.1666667	.2777778E-01	36.00000
1.0	.00	-.1666667	.2777778E-01	36.00000
1.0	1.0	.1666667	.2777778E-01	36.00000
F = 1.0	F' = 2.0			
-2.0	-2.0	.4082483	.1666667	6.000000
-1.0	-1.0	-.2886751	.8333334E-01	12.00000
-1.0	.00	.1666667	.2777778E-01	36.00000
.00	-1.0	.2886751	.8333334E-01	12.00000
.00	.00	-.3333333	.1111111	9.000000
.00	1.0	.2886751	.8333334E-01	12.00000
1.0	.00	.1666667	.2777778E-01	36.00000
1.0	1.0	-.2886751	.8333334E-01	12.00000
1.0	2.0	.4082483	.1666667	6.000000
F = 2.0	F' = 1.0			
-2.0	-1.0	-.4082483	.1666667	6.000000
-1.0	-1.0	-.2886751	.8333334E-01	12.00000
-1.0	.00	-.2886751	.8333334E-01	12.00000
.00	-1.0	-.1666667	.2777778E-01	36.00000
.00	.00	-.3333333	.1111111	9.000000
.00	1.0	-.1666667	.2777778E-01	36.00000
1.0	.00	-.2886751	.8333334E-01	12.00000
1.0	1.0	-.2886751	.8333334E-01	12.00000
2.0	1.0	-.4082483	.1666667	6.000000
F = 2.0	F' = 2.0			
-2.0	-2.0	-.3333333	.1111111	9.000000
-2.0	-1.0	-.2357023	.5555556E-01	18.00000
-1.0	-2.0	-.2357023	.5555556E-01	18.00000
-1.0	-1.0	-.1666667	.2777778E-01	36.00000
-1.0	.00	-.2886751	.8333334E-01	12.00000
.00	-1.0	-.2886751	.8333334E-01	12.00000
.00	1.0	-.2886751	.8333334E-01	12.00000
1.0	.00	-.2886751	.8333334E-01	12.00000
1.0	1.0	-.1666667	.2777778E-01	36.00000
1.0	2.0	-.2357023	.5555556E-01	18.00000
2.0	1.0	.2357023	.5555556E-01	18.00000
2.0	2.0	-.3333333	.1111111	9.000000

Table A.1: Sodium $3S_{1/2} \to 3P_{1/2}$, $3P_{3/2}$ matrix elements

117

APPENDIX B

RAMAN DIFFRACTION

We generalize the treatment presented in section 4 to a multi-level atomic system in the presence of a Raman resonant driving field. No restrictions are placed on the spatial orientation of the propagation vectors for the Raman field components. The goal is to reduce the interaction picture Schrödinger equations by adiabatic elimination of intermediate levels and subsequent application of the rotating wave approximation. The final equations take a form similar to those describing diffraction of a two-level atom in a standing light wave, and our method of reduction closely follows that developed for this problem.[107,108,109]

The starting point is the Schrödinger equation

$$\hat{H} \, | \psi \rangle = i\hbar \frac{\partial | \psi \rangle}{\partial t} \, , \tag{B.1}$$

with

$$\hat{H} = \hbar\omega_0 |e\rangle\langle e| + \sum_i \hbar\omega_i |i\rangle\langle i| + \frac{\hat{p}^2}{2m} + \hat{V} \, , \tag{B.2}$$

where $\hat{V}$ describes the coupling to the light field and $\hat{p}$ is the momentum operator. Fig. B.1 shows an energy level diagram for the multi-level atom. Note that we are explicitly neglecting spontaneous emission processes from the outset. The detuning of the light fields from the intermediate levels is assumed to be large enough so that the population in the intermediate levels is negligible.

We take as a basis the wavefunctions

$$| \psi \rangle = \sum_{\alpha, p} a(p,\alpha) |p,\alpha\rangle \, , \tag{B.3}$$

where α ranges of the internal states of the atom and p is the atom's momentum. Substitution of Eqs. (B.3) and (B.2) into Eq. (B.1) yields the coupled equations
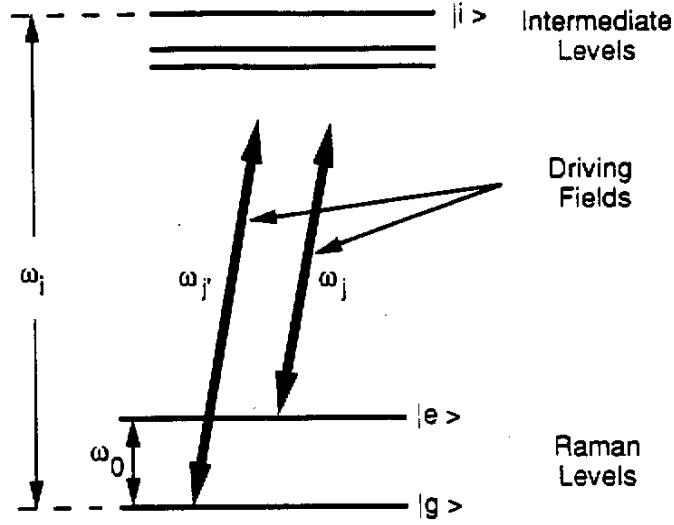
Fig. B.1: Energy level diagram for the multi-level system under consideration.

$$\hbar\omega_0 a(p',\beta)\,\delta_{\beta,e} + \sum_i \hbar\omega_i a(p',\beta)\delta_{\beta,i} + \frac{p^2}{2m}a(p',\beta) +$$

$$\sum_{p,\alpha} a(p,\alpha)\langle p',\beta\,|\,\hat{V}\,|\,p,\alpha\rangle = i\hbar\dot{a}(p',\beta)$$

(B.4)

where $\delta_{i,j}$ is the Kronecker-δ symbol.

The following definitions

$$p' \equiv p_0 + n\hbar k \quad,$$

(B.5)

$$a(p,\beta) \rightarrow a(n,\beta) = e^{-i\omega_{p'}t}\tilde{a}(n,\beta) \quad,$$

(B.6)

119

$$\omega_\beta \equiv \omega_R \delta_{\beta,e} + \frac{p_0^2}{2m\hbar} \quad ,$$

(B.7)

are substituted into Eqs. (B.4) to obtain the interaction picture coupled equations

$$\bar{a}(n',\beta) \left[\hbar\omega_0 \delta_{\beta,e} + \sum_i \hbar\omega_i \delta_{\beta,i} + \frac{(p_0 + n'\hbar k)^2}{2m} - \hbar\omega_\beta \right]$$
$$+ \sum_{n,\alpha} e^{i(\omega_\beta - \omega_\alpha)t} \bar{a}(n,\alpha)\langle n',\beta | \hat{V} | n,\alpha \rangle = i\hbar\dot{\bar{a}}(n',\beta) \quad ,$$

(B.8)

where ω_R is the Raman laser difference frequency and p_0 the initial momentum of the atom. In the following, we neglect the small difference in the momentum $\hbar k$ amongst the various Raman frequency components. The equations are further reduced with the following associations

$$\hbar\gamma \equiv \hbar k \frac{p_0}{m} \qquad (Doppler\ shift) \quad ,$$

(B.9)

$$\hbar\varepsilon \equiv \frac{\hbar^2 k^2}{2m} \qquad (Recoil\ shift) \quad ,$$

(B.10)

$$\Delta \equiv \omega_R - \omega_0 \qquad (Raman\ detuning) \quad .$$

(B.11)

Substituting Eqs. (B.9)-(B.11) into Eq. (B.8), and explicitly expanding Eq. (B.8) in terms of internal atomic states gives

$$i\hbar\dot{\bar{a}}(n,g) = \bar{a}(n,g)\left[n\hbar\gamma + n^2\hbar\varepsilon\right] + \sum_{i,n'} \bar{a}(n',i)\langle n,g | \hat{V} | n',i \rangle \quad ,$$

(B.12)

$$i\hbar\dot{\bar{a}}(n,e) = \bar{a}(n,e)\left[n\hbar\gamma + n^2\hbar\varepsilon - \hbar\Delta\right] + \sum_{i,n'} e^{i\omega_R t} \bar{a}(n',i)\langle n,e | \hat{V} | n',i \rangle \quad ,$$

(B.13)

$$i\hbar\dot{\tilde{a}}(n',i) = \tilde{a}(n',g)\left[n'\cdot\hbar\gamma + n'^2\hbar\varepsilon + \hbar\omega_i\right] +$$

$$\sum_n \tilde{a}(n,g)\langle n',i\,|\,\hat{V}\,|\,n,g\rangle + \sum_n \tilde{a}(n,e)\langle n',i\,|\,\hat{V}\,|\,n,e\rangle e^{-i\omega_e t} \quad .$$

(B.14)

The intermediate levels are eliminated by integrating Eq. (B.14) with the assumption that the amplitudes a(n,g) and a(n,e) are slowly varying with respect to the coupling matrix element. This is a good assumption when the driving fields are far detuned from the optical resonance. Performing the integration yields

$$i\hbar\tilde{a}(n',i) = \sum_{n''} \tilde{a}(n'',g)e^{-i\omega_i't}\int\langle n',i\,|\,\hat{V}\,|\,n'',g\rangle e^{i\omega_i't}dt$$

$$+ \sum_{n''} \tilde{a}(n'',e)e^{-i\omega_i't}\int\langle n',i\,|\,\hat{V}\,|\,n'',e\rangle e^{i(\omega_i'-\omega_e)t}dt \quad ,$$

(B.15)

with

$$\hbar\omega_i' = n'\cdot\hbar\gamma + n'^2\hbar\varepsilon + \hbar\omega_i \quad .$$

(B.16)

We explicitly evaluate the integrals of Eq (B.15) for the following potential $\hat{V}$:

$$\hat{V} = \sum_j \hat{V}_j \quad ,$$

(B.17)

$$\hat{V}_j = \sum_j er\cdot E_j(t)\cos(km_j\cdot r - \omega_j t + \phi_j) \quad ,$$

(B.18)

where the standard semi-classical electric-dipole approximation has been invoked (eg. electro-magnetic fields are treated classically). The time dependence of the amplitude $E_j(t)$ is assumed to be slowly varying with respect to the frequency ω_j. In evaluating the

integrals for (B.15) we make the rotating-wave approximation. One of the integrals is

$$\int \langle n',i | \hat{V}_j | n'',g \rangle e^{i\omega_i't} dt \quad \approx \quad \langle n' | e^{i(k m_j \tau + \phi_j)} | n'' \rangle \langle i | \frac{e r \cdot E_j}{2} | g \rangle \int e^{i(\omega_i' - \omega_j)t} dt$$

(B.19)

$$= -i \delta_{n',m_j + n''} e^{i\phi_j} \frac{\hbar \Omega_{ig}^{j}}{2(\omega_i' - \omega_j)} e^{i(\omega_i' - \omega_j)t} \quad ,$$

where we have defined the Rabi frequency as

$$\hbar \Omega_{i\alpha}^{j} \equiv \langle i | e r \cdot E_j(t) | \alpha \rangle \quad .$$

(B.20)

The above momentum matrix element is simplified using the identity $\langle p' | e^{ikx} | p \rangle = \delta_{p',p+\hbar k}$ ($| p \rangle \sim e^{ipx}$).

After evaluating the remaining integrals in a similar manner, substituting the resulting expression for the amplitudes a_i into Eqs. (B.12) and (B.13), and collecting terms, we find the following reduced coupled equations:

$$i\dot{a}(n,g) = \tilde{a}(n,g)[n \cdot \gamma + n^2 \varepsilon]$$

$$+ \sum_i \sum_{jj'} \tilde{a}(n + m_{j'} - m_j, g) \, \delta_{\omega_j, \omega_{j'}} e^{i(\phi_j - \phi_{j'})} \left(\frac{\Omega_{gi}^{j'} \Omega_{ig}^{j}}{4 \Delta_{ig}^{j}} \right)$$

(B.21)

$$+ \sum_i \sum_{jj'} \tilde{a}(n + m_j - m_{j'}, e) \, \delta_{\omega_j, \omega_k + \omega_{j'}} e^{i(\phi_{j'} - \phi_j)} \left(\frac{\Omega_{gi}^{j} \Omega_{ie}^{j'}}{4 \Delta_{ig}^{j}} \right) \quad ,$$

$$i\dot{\bar{a}}(n,e) = \bar{a}(n,e)[n\cdot\gamma + n^2\varepsilon - \Delta]$$

$$+\sum_i \sum_{jj'} \bar{a}(n+m_{j'}-m_j,e)\,\delta_{\omega_j,\omega_{j'}}e^{i(\phi_j-\phi_{j'})}e^{i\Delta t}\left(\frac{\Omega_{ei}^{j'}\Omega_{ie}^{j}}{4\Delta_{ie}^{j}}\right) \qquad (B.22)$$

$$+\sum_i \sum_{jj'} \bar{a}(n+m_j-m_{j'},g)\,\delta_{\omega_j,\omega_R+\omega_{j'}}e^{i(\phi_j-\phi_{j'})}\left(\frac{\Omega_{ei}^{j'}\Omega_{ig}^{j}}{4\Delta_{ig}^{j}}\right) \quad,$$

with

$$\Delta_{i\alpha}^{j} \equiv \omega_i' - \omega_j - \omega_R\delta_{e,\alpha} \quad . \qquad (B.23)$$

Eqs. (B.21) and (B.22) are the principal results of this section. Solutions to coupled equations of this form are well known in the literature of atomic diffraction. The first terms to the right of the summation symbols describe AC Stark shifts (j = j') and standing wave diffraction (j ≠ j'). Standing wave diffraction results from stimulated absorption and emission of photons of the same frequency but different direction. The second set of terms couple the ground and excited states via. two-photon Raman processes. Finally the first terms on the right determine the effective detuning of the process in question. In the case of the interferometer Raman beam configuration where the Raman transition was driven by retro-reflecting a phase modulated beam, these terms which are responsible for suppression of off-resonant standing wave and Doppler free transitions so that the ground and excited states are effective coupled by only one Raman resonant path.

REFERENCES

1. T. Hänsch and A. Schawlow, Opt. Commun. **13**, 68 (1975).

2. S. Chu, L. Hollberg, J. Bjorkholm, A. Cable and A. Ashkin, Phys. Rev. Lett. **55**, 48 (1985).

3. J. Dalibard, private communication to D. Pritchard.

4. E. Raab, M. Prentiss, A. Cable, S. Chu, and D. Pritchard, Phys. Rev. Lett. **59**, 2631 (1987).

5. D. Weiss, E. Riis, M. Kasevich, K. Moler and S. Chu, in *Light Induced Kinetic Effects*, L. Moi, S. Gozzini, C. Gabbanini, E. Arimondo, F. Strumia, Eds. (ETS Editrice, Pisa, 1991), pp. 35-44.

6. M. Kasevich, D. Weiss, E. Riis, K. Moler, S. Kasapi, and S. Chu, Phys. Rev. Lett. **66**, 2297 (1991).

7. M. Kasevich and S. Chu, submitted to Phys. Rev. Lett.

8. J. Zacharias, Phys. Rev. **94**, 751 (1954).

9. A. deMarchi, Metrologia **18**, 103 (1982).

10. R. G. Beausoleil and T. Hänsch, Phys. Rev. A **33**, 1661 (1986).

11. M. Kasevich, E. Riis, S. Chu, and R. DeVoe, Phys. Rev. Lett. **63**, 612 (1989).

12. N. F. Ramsey, *Molecular Beams* (Oxford Univ. Press, London, 1956).

13. For example, A. Clairon, C. Salomon, S. Guellati and W. Phillips, Europhys. Lett. **16**, 165 (1991).

14. For a recent review of future slow-atom frequency standards see K. Gibble and S. Chu, Metrologia (to be published, 1992).

15. For a review, see J. Hall, M. Zhu, and P. Buch, J. Opt. Soc. Am. B **6**, 2194 (1989).

16. M. Kasevich and S. Chu, Phys. Rev. Lett. **67**, 181 (1991).

17. M. Kasevich and S. Chu, to be published in App. Phys. B.

18. D. Weiss, Stanford PhD thesis.

19. Recoil measurements were first spectroscopically resolved by J. Hall, C. Bordé, and K. Uehara, Phys. Rev. Lett. **37**, 1339 (1976).

20. A non-fountain measurement of this type was recently performed by F. Riehle, T. Kisters, A. White, J. Helmcke, and C. Bordé, Phys. Rev. Lett. **67**, 181 (1991).

21. D. Wineland, J. Bergquist, J. Bollinger, W. Itano, D. Heinzen, S. Gilbert, C. Manney, and C. Weimer, in *Proceedings of the 43rd Annual Symposium on Frequency Control 1989*, (IEEE, New York, 1989).

REFERENCES (continued)

22. Alternatively, the beatnote between two lasers may be phase-locked to a stable rf source.

23. C. Bordé, C. Salomon, S. Avrillier, A. Lerberghe, C. Bréant, D. Bassi, and G. Scoles, Phys. Rev. A **30**, 1836 (1984).

24. V. Baklanov, B. Dubetsky, and V. Chebotayev, Appl. Phys. **9**, 171 (1976).

25. P. Nelson, Rev. Sci. Instrum. **62**, 2069 (1991).

26. P. Saulson, Rev. Sci. Instrum. **55**, 1315 (1984).

27. C. Bordé, Phys. Lett. A **140**, 10 (1989).

28. O. Carnal and J. Mlynek, Phys. Rev. Lett. **66**, 2689 (1991).

29. D. Keith, C. Ekstrom, Q. Turchette, and D. Pritchard, Phys. Rev. Lett. **66**, 2693 (1991).

30. L. Marton, J. Simson, and J. Suddeth, Phys. Rev. **90**, 490 (1954).

31. H. Rauch, W. Treimer, and U. Bronse, Phys. Lett. **47A**, 369 (1974).

32. R. Colella, A. Overhauser, and S. Werner, Phys. Rev. Lett. **34**, 1472 (1975).

33. S. Werner, J. Staudenmann, and R. Colella, Phys. Rev. Lett. **42**, 1102 (1979).

34. Y. Aharonov and A. Casher, Phys. Rev. Lett. **53**, 319 (1984).

35. A. Cimmino, G. Opat, A. Klein, H. Kaiser, S. Werner, M. Arif, and R. Clothier, Phys. Rev. Lett. **63**, 380 (1989).

36. J. Jackson, *Classical Electrodynamics* (Wiley, New York, 1975).

37. M. Kasevich, D. Weiss, and S. Chu, Opt. Lett. **15**, 607 (1990).

38. For a review of cold atom-atom collisions, see P. Julienne and F. Mies, J. Opt. Soc. Am. B **6**, 2257 (1989).

39. R. Chiao, P. Kwiat, and A. Steinberg, Physica B **175**, 257 (1991).

40. H. Casimir and D. Polder, Phys. Rev. **73**, 360 (1948).

41. G. Doyen, Phys. Rev. B **22**, 497 (1980); W. Brenig, Z. Physik B **36**, 227 (1980).

42. J. Berkhout, O. Luiten, I. Setija, T. Hijmans, T. Mizusaki, and J. Walraven, Phys. Rev. Lett. **63**, 1689 (1989).

43. M. Kasevich, K. Moler, E. Riis, E. Sunderman, D. Weiss, and S. Chu, *Atomic Physics 12*, R. Lewis and J. Zorn, Eds. (AIP, New York, 1991).

44. E. Lifshitz, Sov. Phys. **2**, 73 (1956).

45. For an excellent historical review of the development of the understanding of radiation forces, see Minogin and Letokhov, *Laser Light Pressure on Atoms* (Gordon and Breach, New York, 1987) pp. 1-12.

46. For a rigorous discussion, see J. Gordon and A. Ashkin, Phys. Rev. A **21**, 1606 (1980).

47. For a good introductory discussion, see J. Sakuri, *Advanced Quantum Mechanics* (Benjamin/Cummings, Menlo Park, 1984), p. 36.

48. See for example, Meystre and Sargent, *Element of Quantum Optics* (Springer-Verlag, New York, 1991), pp. 111.

49. L. Allen and J. Eberly, *Optical Resonance and Two-Level Atoms* (Wiley, New York, 1975).

50. J. Dalibard and C. Cohen-Tannoudji, J. Opt. Soc. Am. **B, 2**, 1707 (1985).

51. For a rigorous discussion, see G. Nienhuis, P. van der Straten and S-Q. Shang, Phys. Rev. A **44**, 462 (1991).

52. Y. Castin, and J. Dalibard, Europhys. Lett. **14**, 761 (1991).

53. D. Walls, Enrico Fermi 1991 Summer School Lecture Notes (to be published).

54. D. Wineland and W. Itano, Phys. Rev. A **20**, 1521 (1979).

55. J. Dalibard and C. Cohen-Tannoudji, J. Phys B **18**, 1661 (1985); J. Dalibard, Physica Scripta T12, 28 (1986).

56. For a good review, see P.D. Lett, et. al., J. Opt. Soc. Am. B **6**, 1989 (2084).

57. A. Aspect, E. Arimondo, R. Kaiser, N. Vansteenkiste, and C. Cohen-Tannoudji, Phys. Rev. Lett. **61**, 826 (1988).

58. P. Lett, R. Watts, C. Westbrook, W. Phillips, P. Gould, and H. Metcalf, Phys. Rev. Lett. **61**, 169 (1988).

59. J. Dalibard and C. Cohen-Tannoudji, J. Opt. Soc. Am. B **6**, 2023 (1989).

60. P. Ungar, D. Weiss, E. Riis, and S. Chu, J. Opt. Soc. Am. B **6**, 2058 (1989).

61. For clarity, we assume that the atom does not decay into the F=1 hyperfine level during the optical pumping process. See section 2.5.

62. See S. Chu, Enrico Fermi 1991 Summer School Lecture Notes (to be published) for an intuitive explanation of these rules.

63. Y. Castin and J. Dalibard, Europhys. Lett. **14**, 761 (1991).

64. D. Weiss, E. Riis, Y. Shevy, P. Ungar and S. Chu, J. Opt. Soc. Am. B **6**, 2072 (1989)

REFERENCES (continued)

65. K. Mølmer and Y. Castin, J. Phys. B **23**, 4101 (1990).

66. J. Dalibard, Y. Castin, K. Mølmer, Phys. Rev. Lett. **68**, 580 (1992).

67. K. Mølmer, Phys. Rev. A **44**, 5820 (1991).

68. D. Sesko, T. Walker, and C. Wieman, J. Opt. Soc. Am. B **8**, 946 (1991).

69. A. Steane and C. Foot, Europhys. Lett. **14**, 231 (1991).

70. K. Gibble, S. Kasapi, and S. Chu, Opt. Lett. **17**, 526 (1992).

71. B. Sheehy, S-Q. Shang, P. van Straten, S. Hatamian, and H. Metcalf, Phys. Rev. Lett. **64**, 858 (1990).

72. J. Javanainen, Phys. Rev. Lett. **64**, 519 (1990).

73. V. Minogin, M. Olshany and S. Shulga, J. Opt. Soc. Am. B **6**, 2108 (1989).

74. C. Monroe, W. Swann, H. Robinson, and C.E. Wieman, Phys. Rev. Lett. **65**, 1571 (1990).

75. J. Tegopoulus and E. Kriezis, *Eddy Currents in Linear Conducting Media* (Elsevier, New York, 1985).

76. W. Ertmer, R. Blatt, J. Hall, and M. Zhu, Phys. Rev. Lett. **54**, 996 (1985).

77. J. Hall, L. Hollberg, T. Baer, and H. Robinson, Appl. Phys. Lett. **39**, 680 (1981).

78. L. Windholz and M. Musso, Phys. Rev. A **39**, 2472 (1989).

79. This laser was also used in the first optical spectroscopy of Ps and the first optical molasses and trapping experiments.

80. Wavepacket diffraction from a narrow slit was first reported by J. Leavitt and F. Bills, Am. J. Phys. **37**, 905 (1969).

81. For a more detailed presentation, see K. Moler, D.S. Weiss, M. Kasevich, and S. Chu, Phys Rev. A **45**, 342 (1992).

82. C. Cohen-Tannoudji, Cours de Physique Atomique et Moleculaire, Collège de France, 1989.

83. C. Cohen-Tannoudji, B. Diu, F. Laloë, *Quantum Mechanics* (Wiley, New York, 1963).

84. The approach is to break down a wavepacket into momentum eigenstates, as in Eq. (4.3), evolve each eigenstate according to Eq. (4.6), and then reconstruct the spatial wavepacket.

85. M. Rose, *Elementary Theory of Angular Momentum* (Wiley, New York, 1963).

86. Direct evaluation of the matrix elements shows this to be true. For a more elegant explanation see C. Cohen-Tannoudji and J. Dupont-Roc, Phys. Rev. A 3, 968 (1972).

87. M. Zhu and J. Hall, IQEC '90 Technical Digest 8, 230 (1990).

88. V.P. Chebotayev, B. Dubetsky, A.P. Kasantsev, V.P. Yakovlev, J. Opt. Soc. Am. B 2, 1791 (1985).

89. J.F. Clauser, Physica (Amsterdam) 151B, 262 (1988).

90. M. Zumberge, private communication.

91. M. Hillery and M. Scully, in Quantum Optics, Experimental Gravitation and Measurement Theory, P. Meystre and M. Scully, Eds. (Plenum Press, New York, 1983), pp. 65-85.

92. M.V. Berry, Proc. Roy. Soc. London, Ser. A 392, 45 (1984); Y. Aharonov and J. Anandan, Phys. Rev. Lett. 58, 1593 (1987).

93. See, for example, Ref. 49.

94. See, for example, J. Marion, Classical Dynamics of Particles and Fields (New York: Academic Press, 1970), p. 343.

95. N. Ramsey, Molecular Beams, (Oxford Univ. Press, Oxford, 1956); S. Chu and M. Kasevich, Laser Spectroscopy X, M. Ducloy, E. Giacobino, and G. Camy Eds. (World Scientific, New York, 1992).

96. R.P. Feynman and A.R. Hibbs, Quantum Mechanics and Path Integrals (McGraw-Hill, New York, 1965).

97. A.W. Overhauser and R. Colella, Phys. Rev. Lett. 33, 1237 (1974).

98. The natural resonance frequency of the seismometer is 1 Hz.

99. C. Monroe, H. Robinson, and C. Wieman, Opt. Lett. 16, 50 (1991).

100. S. Kasapi and K. Gibble, private communication.

101. J. Schmiedmayer, Nuc. Inst. and Meth. in Phys. Res. A284, 59 (1989).

102. J.E. Faller and I. Marson, Metrologia 25, 49 (1988).

103. K.E. Gibble, Ph.D. Thesis, University of Colorado, 1990 (unpublished); C.E. Wieman and L. Hollberg, Rev. Sci. Instrum. 62, 1 (1991).

104. C. Monroe, W. Swann, H. Robinson, and C. Wieman, Phys. Rev. Lett. 65, 1571 (1990).

105. B. Shore and H. Menzel, Principles of Atomic Spectra (Wiley, New York, 1968).

106. T. Tamura, Comp. Phys. 1, 337.

REFERENCES (continued)

107. E. Arimondo, A. Bambini, and S. Stenholm, Phys. Rev. A **24**, 898 (1981).
108. A.F. Bernhardt and B.W. Shore, Phys. Rev. A **23**, 1290 (1981).
109. J. Cook and A.F. Bernhardt, Phys. Rev. A **18**, 2533 (1978).